Contrail Formation

Exploring options for improving prediction methods on the Formation of Contrails from Modern Turbofan Engines

G. Nieuwerth

Contrail Formation

Exploring options for improving prediction methods on the Formation of Contrails from Modern Turbofan Engines

by

G. Nieuwerth

to obtain the degree of Master of Science
at the Delft University of Technology,
to be defended publicly on Monday May 15th, 2023 at 13:30

Student number:	4171047	
Project duration:	September 1, 2020 – May 15, 2023	
Thesis committee:	Prof. Dr. A. G. Rao,	TU Delft, chair
	Dr. ir. F. Yin,	TU Delft, supervisor
	Dr. S. J. Hulshoff,	TU Delft, examiner
	Dr. ir. F. F. J. Schrijer	TU Delft, examiner

An electronic version of this thesis is available at http://repository.tudelft.nl/.

TU Delft

Preface

Before you lies the Master Thesis "Contrail Formation: Exploring options for improving prediction methods on the Formation of Contrails from Modern Turbofan Engines". As a student within the Flight Performance track of the Aerospace Engineering Master of the Delft University of Technology, this research topic would not necessarily be the most obvious choice. It lies within a research field that, while containing many areas of overlap to my own track, takes place largely in the Aircraft Noise and Climate Effects section of the faculty. However, the opportunity was granted to me to perform this research nonetheless, under the supervision of Dr. Feijia Yin, in tandem with Prof. Dr. Arvind Gangoli Rao from my own master track. As someone with a great interest in climate research, I am very grateful for their support in this matter. They gave me a great deal of freedom to pursue the research in whatever manner I thought was best. In the end, my path towards the final result ended up being long and winding. However, I learned so much more in this time than I could ever convey in the span of a single thesis, not only with regard to a wide range of scientific topics and engineering skills, but also about myself. For that opportunity, as well as the many hours of meetings they dedicated to keeping me on track, I would like to offer both Feijia and Arvind my sincere thanks.

There are four people who deserve special thanks, without whom this thesis would surely not be lying before you in the completed state it is now. My parents, who as far as I am concerned deserve an honorary part of my Master's degree for their tireless efforts to support me and believe in me. During my lowest lows, they have been there for me, and it is my great pleasure to share my highest highs with them as well. My brother Martin, whom I have always looked up to, and continues to be an inspiration to me every day. And finally, to Silvia, who is the sunshine of my life, and whose unwavering support has made all the difference in the world. Thank you.

Without further ado, I am happy to present my Thesis for the degree of Master of Science in Aerospace Engineering.

G. Nieuwerth
Delft, February 2023

Abstract

One of the most pressing challenges faced by modern society is maintaining a habitable planet by curbing the effects of anthropogenic warming of the earth, to which the aviation sector is a significant contributor. This thesis contributes to the body of science in the field of aviation climate impact by improving upon current prediction methods for the formation of contrails from modern High Bypass Ratio aircraft turbofan engines. These methods are based on the Schmidt - Appleman Criterion (SAC), which was developed for simple turbojets and therefore rests on questionable assumptions with respect to modern engines. Specifically the impact of bypass ratio on the accuracy of current methods is investigated in this research. This is done through the development of a modelling framework with the objective of estimating the impact of engine configurations on contrail formation by analyzing the physics of the mixing process between core and bypass flow.

The first step in the framework is the estimation of conditions at the core and bypass nozzle exit planes of the engine. This is done by use of an Engine Performance Model, designed in the GSP software tool. Subsequently, a Flow Field Solver module has been set up to resolve the pressure, temperature, and velocity in the exhaust of the engine. An extensive investigation into the various options for this module has yielded the conclusion that, while in particular the 2D Finite Element Method shows promise with respect to computational efficiency, and a fully 3D CFD simulation would most accurately reflect reality, a 2D axisymmetric CFD approach provides the best trade-off between reliable results and efficient use of resources. The next step is the prediction of contrail formation locations within the flow field through a Contrail Formation Prediction Model. A Species Transport Model native to the CFD solver is employed to predict the dispersion of water vapour from the core exhaust throughout the flow field, after which contrail locations are determined by a set of criteria for homogeneous ice crystal formation. Finally, mixing lines from the engine are drawn by tracking the evolution of flow properties along particle pathways through the field. These are then compared to the mixing line generated by the original prediction method based on the SAC, and a comparison is made, allowing conclusions to be drawn with respect to the validity of the SAC for the given engine.

Once completed, this framework has been applied to a case study of a modern HBPR engine: the CFM Leap-1A model. The resulting contrail prediction shows close agreement with state-of-the-art contrail formation simulations for the same engine, giving confidence in the validity of the model framework. In addition, the results of the case study allow the following conclusions to be drawn with respect to the accuracy of current SAC-based contrail prediction methods. First, the assumptions of instantaneous and isobaric mixing underlying the SAC prediction methods are not valid for modern High Bypass Ratio turbofan engines. In addition, the influence of an increase in Bypass Ratio is to commensurately increase the discrepancy between the initial temperature and water vapour content of the real mixing line from the engine and the values assumed by the SAC. When comparing the mixing lines from the current model to the SAC mixing line, the latter represents an upper limit to the former. The results from this case study therefore suggest that in reality, mixing lines from modern engines have a lower gradient than predicted by the SAC, and therefore the SAC may predict contrails to be formed in certain cases where the current model would not.

For future research, it is recommended that additional attention is given to the microphysical processes involved in contrail formation, so more confidence can be gained in the validity of the current framework for a wide range of cases. This framework can then also be included in the design process of future engines, as well as in the decision process for flight paths, so contrail formation can be minimized in the future.

List of Figures

List of Tables

Nomenclature

β	Diameter ratio
Δ	Difference
ϵ	turbulence dissipation rate
η	Aircraft propulsion efficiency
ω	specific turbulence dissipation rate
ρ	Density
AFR	Air to Fuel Ratio
BPR	Engine Bypass Ratio
c_p	Air constant pressure heat coefficient
CFD	Computational Fluid Dynamics
D	Molecular diffusivity
D_i	Diameter of the inner jet
D_o	Diameter of the outer jet
E	Solution Error
e_s	Saturation pressure
EI	Engine Emission Index
$EI(H_2O)$	Engine Emission Index of Water
f	Solution
G	slope of mixing line between exhaust and ambient conditions
GCI	Grid Convergence Index
h	Enthalpy
h	Measure of grid spacing
$HBPR$	High Bypass Ratio
$ISSR$	Ice Supersaturated Region
k	Turbulence Kinetic Energy
$m(fuel)$	mass of fuel
$m(species)$	mass of emitted species
M_1	Molar masses of gas 1 in a mixture
M_{air}	Air molar mass
m_b	bypass mass flow

m_c	core mass flow
M_{H_20}	Water molar mass
MR	Mixing Ratio
N	Dilution Ratio
OPR	Engine Overall Pressure Ratio
p	order of convergence
p^{H_20}	Water vapour partial pressure
p_a	Ambient pressure
$p_a^{H_20}$	Ambient Water vapour partial pressure
$p_e^{H_20}$	Exhaust Water vapour partial pressure
Q	Quantity
Q	Fuel Heat Content
$q(air)$	mass fraction of air
$q(H_2O)$	mass fraction of Water
$q(species)$	mass fraction of emitted species
q_{H_20}	Water vapour concentration
r	grid Refinement ratio
R_{gas}	Specific Gas Constant
r_{i}	jet half width
rh	Relative Humidity
SAC	Schmidt - Appleman Criterion
Sc	Schmidt Number
SLS	Sea Level Static
T_a	Ambient temperature
T_e	Exhaust temperature
$U(cl)$	Center Line Velocity
U_0	Characteristic velocity at the center line
v	Kinematic Viscosity
x_1	Molar fraction of gas 1 in a mixture
Z	Mixing Ratio

Contents

1

Introduction

The climate and environmental impact of human activity has become a more and more pressing research topic over the last decades. Aviation is one industry that not only contributes to global warming, but has also steadily grown larger, and is expected to continue its growth in the future. While an argument can be made that curbing this growth is essential to limiting aviation's contribution to global warming, another approach is possible, and generally more attractive to businesses: Reduce the climate impact of every flight, so the growing demand for aviation can be met while reducing its overall climate impact. In the long term, radical changes in propulsion technology need to be considered, such as fuel cell powered electric aircraft, although the effect of water vapour emissions from such technologies would also need to be considered. However, in the short term, the existing fleet, powered by turbofan engines, should also reduce its contribution to global warming.

Aviation currently contributes an estimated 3-5% to the total global anthropogenic warming of the earth [10]. Much of the uncertainty within that estimate is related to the climate impact of contrails: the condensation of water from the turbofan exhaust which forms trails and sometimes (cirrus) clouds of ice crystals, which have a net warming effect on the planet. These contrails only form under certain circumstances, so accurately predicting when they occur is helpful for avoiding their formation and thereby reducing the total radiative forcing effect of turbofan exhausts.

The current methods for predicting contrail formation are largely based on a method called the "Schmidt - Appleman Criterion" (SAC) [1]. This method relates the exhaust temperature and pressure to ambient conditions, assumes a straight mixing line between the two on a pressure - temperature plot. Comparing this mixing line to the saturation pressure curves of ice and water, which depend also on temperature, then allows us to predict when persistent contrails are formed. Under the aforementioned assumptions, this method is physically well motivated and accurate. However, for modern turbofan engines, these assumptions can be drawn into question. The chief reason is the increasing bypass ratio of newer engines, which makes them more efficient, but also implies an extra step of mixing: that between the core and bypass flow. To apply the SAC, therefore, these flows are assumed to be instantaneously and isobarically mixed at the engine exit. These assumptions are increasingly questionable for higher bypass ratio turbofan engines.

It is therefore worth investigating, firstly how (in)accurate these assumptions are, and secondly how they influence the overall accuracy of current contrail formation prediction methods for modern high bypass turbofan engines. These are the aims of the current research, resulting in the following research objective:

To estimate the impact of engine configurations on contrail formation by analyzing the physics of the mixing process between core and bypass flow through engine performance modelling and exhaust flow simulation.

This objective is pursued by developing a modelling framework for predicting the formation of contrails from a modern engine. The framework is then applied to a case study for a modern engine and its results compared to current prediction methods.

This report describes the research work done for the development and implementation of the model framework for the prediction of the formation of contrails from modern turbofan engines. First, in chapter 2, the scientific background and literature is described, followed by the formulation of research questions and objectives. Subsequently, chapter 3 sets out the overall research setup and approach, including the design of the modelling framework. The first step in this framework then, the Engine Performance Model, is described in chapter 4, along with the results for the case study. The development of the Flow Field Solver module, which resolves the relevant parameters in the exhaust flow field of the engine, is set out in chapter 5. In addition, this chapter includes the verification and validation efforts done for the module, as well as a sensitivity analysis with respect to input parameters, and results and conclusions from the case study. The final step in the framework, namely the prediction of water vapour dispersion and the resulting contrails, is done in chapter 6. A comparison between the model results and original SAC predictions for the given case study is also shown here. Finally, chapter 7 draws conclusions with respect to the original research questions and objectives, followed by recommendations for future research.

2

Background and Research Objectives

This chapter aims to survey the existing literature in the field of contrail formation prediction, and lay the groundwork for modelling the exhaust plumes of modern high bypass ratio engines in order to examine the validity of the assumptions underlying the Schmidt - Appleman Criterion. To this end, section 2.1 discusses the current understanding of climate change and greenhouse gases. Consequently, section 2.2 treats the role of aviation in this phenomenon. The mechanism by which contrails are formed is explained in section 2.3, after which the state of the art in contrail formation prediction is treated in section 2.4. This is followed by an overview of literature in mixing physics and methods for simulating the coaxial jets of core and bypass flow in the jet exhaust in section 2.5. In section 2.6, a research gap is defined, followed by the formulation of research questions and objectives.

2.1. Science of Anthropogenic Climate Change

Humans have contributed to the warming of the planet since roughly the start of the industrial era in 1750, mostly through our emissions of greenhouse gases such as carbon dioxide, methane, and nitrous oxide. In 1995, the Intergovernmental Panel on Climate Change (IPCC) brought out its Second Assessment Report, concerning the effects of all anthropogenic emissions on climate change [16]. The findings from this report are summarized here to establish a basic framework for understanding the science of anthropogenic global warming.

The mechanism by which species in the atmosphere affect the global temperature balance is defined as "radiative forcing". Certain species can either affect the amount of radiation that is let through the atmosphere from the sun, or the amount emitted back out to space by the earth, or a combination of the two. The difference between the inbound and outbound radiation blocked or absorbed is defined as the net radiative forcing. A net positive radiative forcing is defined as a warming effect, and a negative radiative forcing has a cooling effect. As sunlight consists mostly of visible and UV light, whereas the outward radiation from the Earth is on the infrared spectrum, the net radiative forcing of a species depends on its optical properties: which wavelengths of light it lets through or not.

Greenhouse gases are so named because of their net positive radiative forcing effect: they block infrared radiation, preventing heat from escaping the atmosphere, while still letting through visible and UV light. An additional problematic property of these greenhouse gases is their longevity, in the case of CO_2 remaining in the atmosphere for decades to centuries. A rule of thumb for CO_2 lifetime is: 50% remains after 50 years, but 40% is still there after 100 years, and after 1000 to 10000 years, 20 % remains [8]. A certain amount of further global warming is therefore already guaranteed, even if net zero emissions were reached today. As the radiative forcing effect of CO_2 is one of the best understood, the emissions of a wide range of species are often expressed in the amount of CO_2 that would have the same net radiative forcing effect. This then allows us to capture policy and technological goals in a single number: the so-called CO_2 budget (or colloquially, carbon budget).

One of the most recent reports by the IPCC treats one such policy goal and the measures that need to be taken

to reach it: the limitation of global temperature rise to 1.5 $°C$ [17]. As stated in this Special Report on Global Warming of 1.5 $°C$, approximately 1.0 $°C$ of warming above pre-industrial levels has already been caused by human activity. A total 1.5 $°C$ rise in global temperature would result in larger climate-related risks, such as rising sea levels, mass species extinction events and loss of ecosystems, and more extreme weather events, than currently exist. However, these risks would still be significantly lower than at a temperature rise of 2.0 $°C$. Any warming above 2.0 $°C$, and the risk of reaching tipping points, such as the disappearance of polar ice sheets and release of methane gas from tundra areas, increases significantly. This would lead to meters of sea level rise over the next centuries, inundating many of the most densely populated areas of the world. A cascade of tipping points would also lead to runaway temperature changes, with comparisons being drawn to the levels of CO_2 concentrations last seen in the Eocene, 50 million years ago, when the average global temperature was up to 14 $°C$ higher than pre-industrial levels [24]. An overview of the global tipping points and their interactions can be seen in Figure 2.1.

The writers of the IPCC report estimated at time of writing that the total remaining carbon budget for a probability of 50% of staying within 1.5 $°C$ temperature rise was 580 gigatonnes $CO_2 (GtCO_2)$. With yearly global emissions still steady at around 42 $GtCO_2$ per year, the Mercator Research Institute on Global Commons and Climate Change (MCC) estimates there are less than seven years left if this plateau is maintained, before that budget is spent [25].

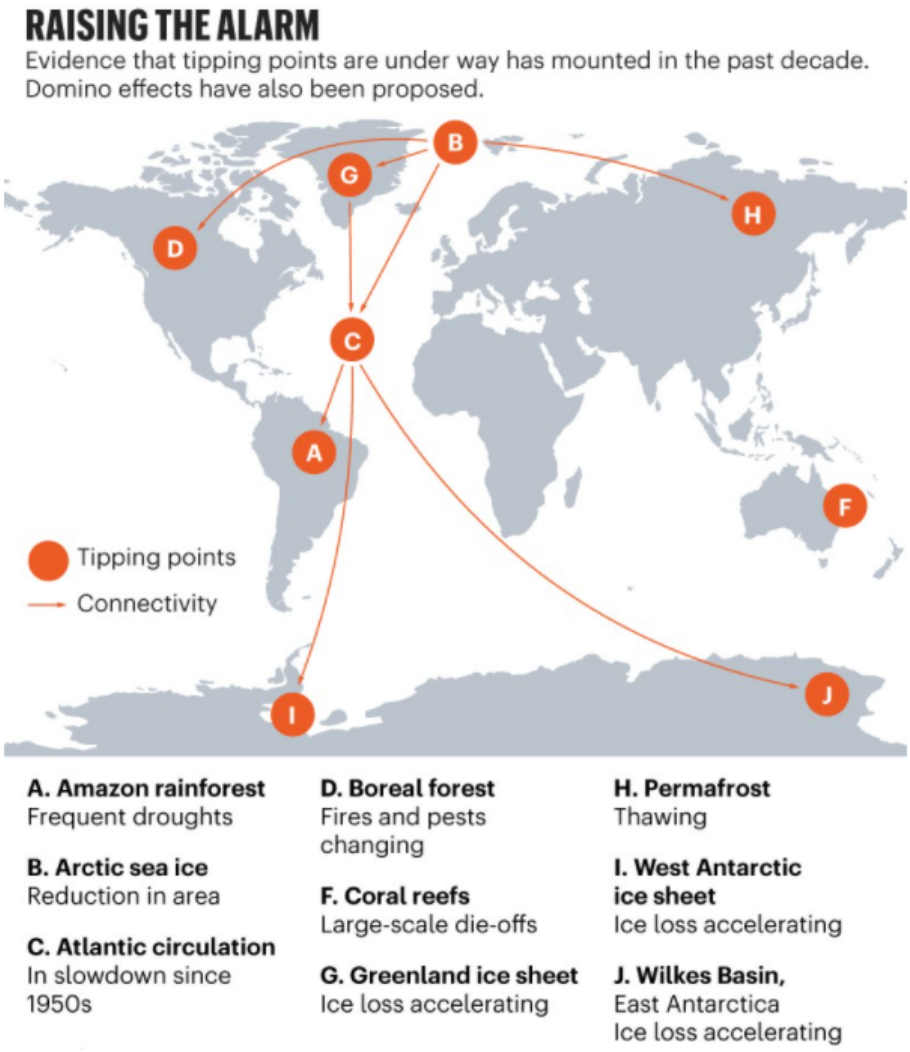

Figure 2.1: Overview of climate tipping points and the connections between them [23].

It is evident, then, that radical reduction in greenhouse gas emissions is needed on a global scale, if a habitable planet is to be maintained.

2.2. The Role of Aviation

In the previous section, the concept of anthropogenic global warming was treated, along with the importance of limiting global temperature rise to 1.5 $^{\circ}C$. Aviation as an industry contributes significantly to the annual radiative forcing effect, with an estimated 2.5% of global carbon emissions, and 3 to 5 % of total radiative forcing from all factors combined. Additionally, since travel restrictions due to the recent pandemic have been lifted, previous trends in the growth of annual passengers transported by aviation are expected to continue at approximately 4% per year. It is clear, then, that to curb the short term climate impact of aviation, either these passenger numbers, or the climate impact per passenger, or both, need to be reduced. This thesis will focus on the second aspect: reducing the climate impact per passenger. While large-scale changes such as transitioning to electric flying are likely necessary to achieve true sustainable air travel [26], the time constraints laid out in section 2.1 make it clear that the existing, kerosene turbofan-powered fleet should also reduce its climate impact in the short term, while such a paradigm shift is pursued.

Before thinking about how to reduce the radiative forcing contribution of aircraft, its current impact and the physical mechanisms underlying it need to be understood. To this end, the exhaust products of a typical turbofan engine are examined. An overview of these products and their respective radiative forcing effects is given in Figure 2.2.

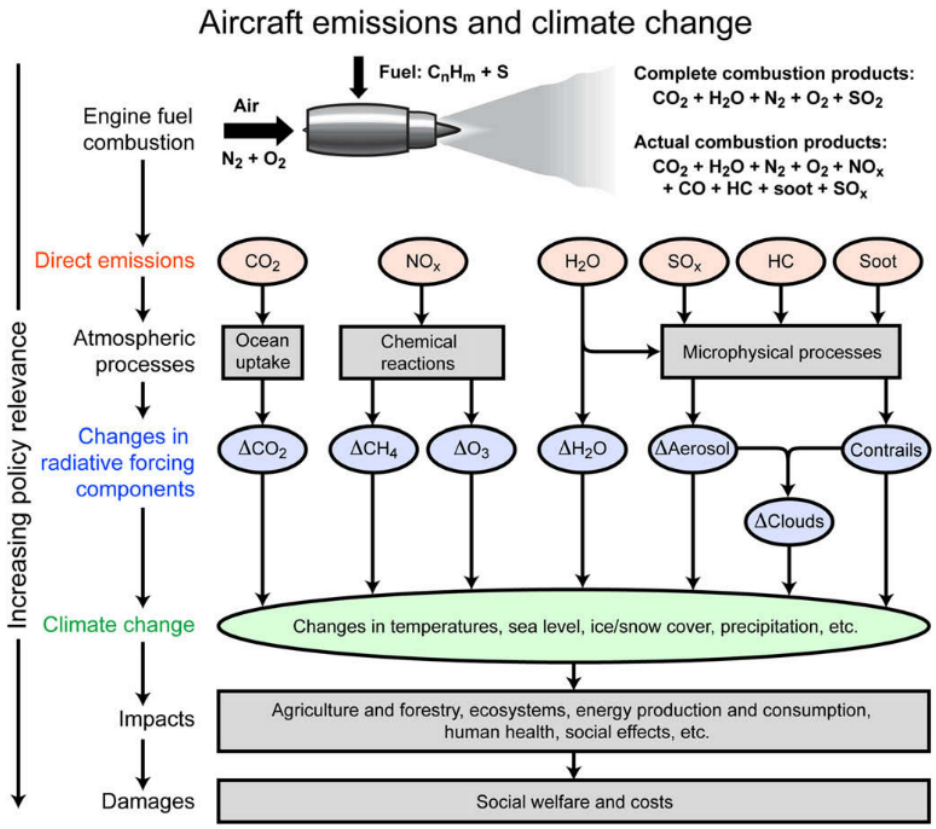

Figure 2.2: The main emissions from aircraft engines and their pathways towards impacting the climate. [20]

At the top of the figure are the combustion processes that take place in the jet engine. The direct emissions are then summarized below, where a distinction can be made between water - and non - water related emissions. CO_2 and NO_x emissions have pathways towards increasing direct radiative forcing components CO_2, CH_4, and O_3. Of these three, CO_2 is long-lasting, while CH_4 and O_3 are depleted through atmospheric processes. The emissions on the right, H_2O, SO_x, UHC (unburnt hydrocarbons), and soot, are all related to changes in

the water content of the atmosphere through microphysical processes. In addition, SO_x and UHC have a direct radiative forcing effect aside from their role in contrail and cirrus formation.

For a breakdown of the radiative forcing effects of these various aircraft emissions, Figure 2.3 can be examined. From this figure, it is clear that contrails and the cirrus clouds they induce are the source of the largest uncertainty in the estimation of total aviation induced radiative forcing.

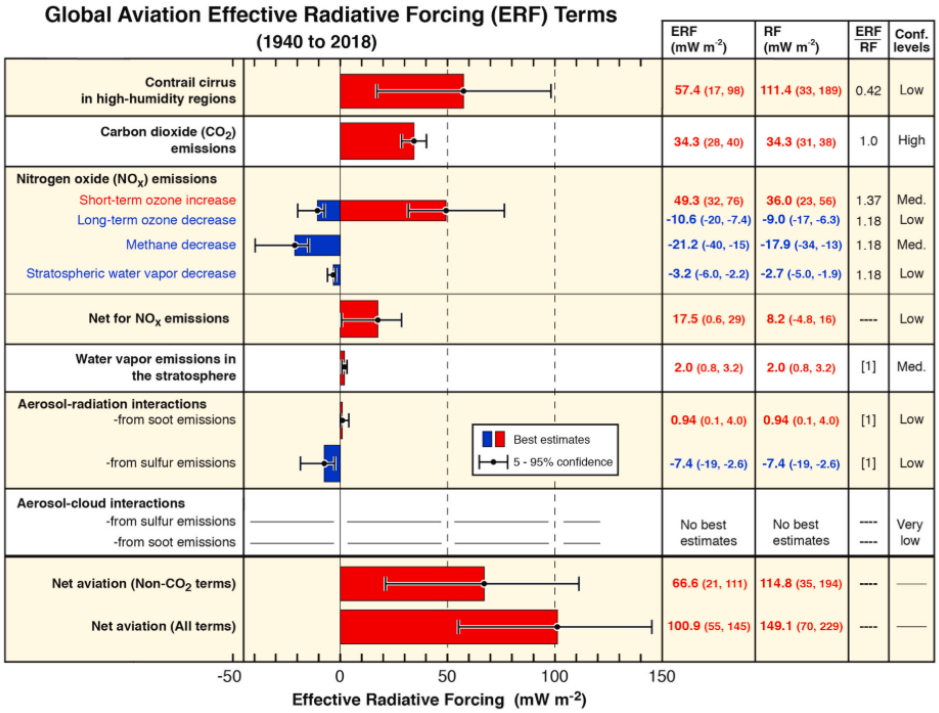

Figure 2.3: Breakdown of the radiative forcing effects from aircraft emissions and the uncertainties in their estimation [22]

As mentioned in section 2.1, the radiative forcing effects of CO_2, CH_4, and O_3 are well understood, and are not the focus of this research. However, the exact impact of water emission depends on a number of variables (e.g. flow conditions at the core and bypass exit, as well as ambient temperature and water vapour content), and is still an active topic of research. The main radiative forcing effects of water emissions are due to the formation of contrails and a subsequent increase in cirrus cloud coverage. This mechanism can be summarized as follows:

- Water, soot, sulfur, and unburnt hydrocarbons are emitted by the engine exhaust at high pressure and temperature.
- Ambient conditions exhibit much lower pressure and temperature than those of the exhaust, as typical aircraft cruise altitudes are around 10 km.
- Mixing occurs between exhaust and environment, reducing pressure and temperature until ambient conditions are reached.
- Droplets of water form around nuclei of soot, sulfur, and unburnt hydrocarbon.
- The droplets become supercooled and form ice crystals under the right conditions
- Condensation trails, or contrails for short, are formed in the wake of the aircraft.

It is estimated that the contribution of persistent contrails formed in this way from aircraft exhaust could be as much as 60% of the total radiative forcing effect of aviation [22].

Limitations in Current Understanding

The main limitations in quantifying the overall impact of contrails from aviation are related to determining their exact optical properties, knowing when and where they are formed, and distinguishing them from existing cirrus clouds. One of the best ways to address these limitations is by accurately describing and predicting the formation of persistent contrails based on the aircraft specifications and its surroundings.

2.3. The Microphysics of Contrail Formation

Contrails, or condensation trails, are formed when water vapor emitted by the engine condensates to form ice crystals around soot or other particles after mixing with the ambient air. To predict their formation, then, an understanding must first be established of this condensation process. In this section, the formation of ice crystals in the exhaust plume is examined on a microphysics level.

To understand the ice crystal formation process, use can be made of Figure 2.4. The main steps involved can be summarized as follows:

1. Exhaust products exit the engine. They can be categorized as: non-volatile particles (mainly soot), volatile particles (sulfur, unburnt hydrocarbon, ion clusters), and water vapor.

2. The exhaust plume mixes with ambient air, which contains aerosols and soluble organics. When water vapor saturation occurs, liquid droplets are formed around the non-volatile exhaust particles and ambient aerosols.

3. Further mixing lowers the temperature until ice nucleation occurs. The size and number of ice particles depends on the initial number of soot particles and concentration of ambient aerosols. This relation can be seen in Figure 2.5.

4. The plume cools further until ambient conditions are reached. The exact ambient conditions determine if persistent contrails are formed (see section 2.4 for a detailed explanation).

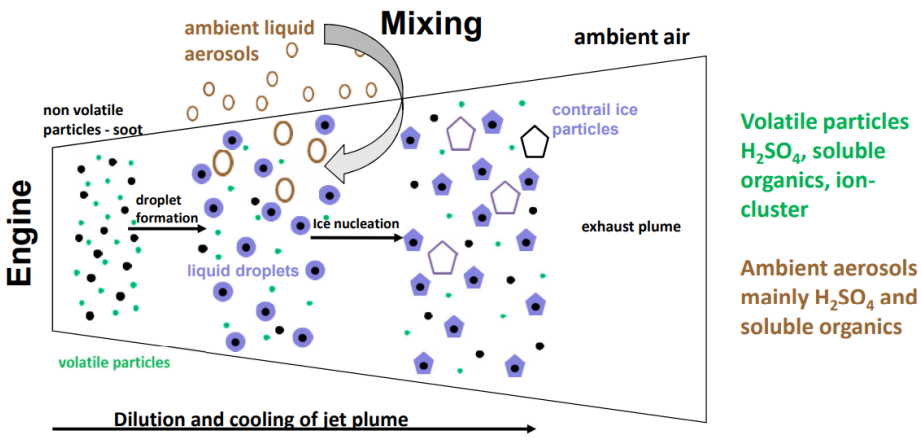

Figure 2.4: A schematic overview of the formation of contrails on the micro level [9].

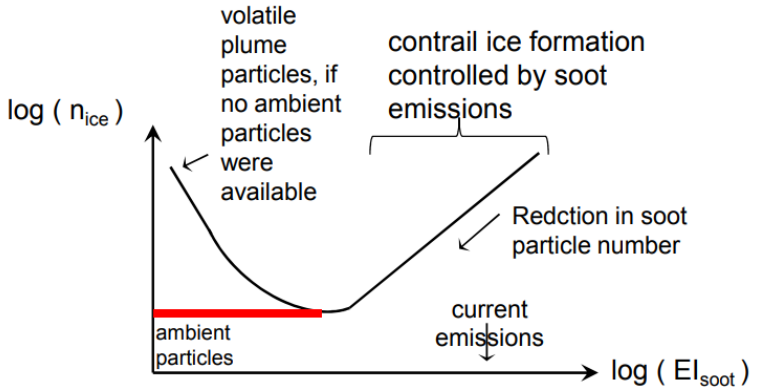

Figure 2.5: Plot depicting the relation between soot number emission index and number of ice crystals that are formed [9]. It can be observed that a baseline of ambient particles is always present for ice crystal formation. In addition, in a clean exhaust and the hypothetical absence of ambient particles, crystals would form around the volatile plume particles instead.

2.4. Schmidt - Appleman Criterion

In this section, a treatment is given of the concepts of saturation and relative humidity. Consequently, use is made of these concepts to explain one of the earliest contrail prediction methods, which is still relevant today: the **Schmidt - Appleman Criterion (SAC)**.

Saturation

Within a mixture of air, water vapor, and liquid or ice phase water, there is an exchange of water molecules between these phases. A flux of water molecules exists from the liquid (or solid) state to the gaseous state, and an opposite flux exists from gaseous to liquid or solid state. The air containing the water vapor is said to be saturated if these two fluxes are in equilibrium. If the flux from gaseous to liquid / solid state is larger than the reverse, the air is supersaturated, and the opposite case is called sub-saturation. The flux from gaseous to liquid/solid state, especially, is influenced by the temperature of the air. The transition from liquid or solid to gaseous state is an endothermic one: the enthalpy of the water increases, which means heat needs to be added for the transition to take place. Conversely, a water vapour molecule transitioning to liquid or solid state undergoes an exothermic reaction: the enthalpy decreases, so heat is extracted. Increasing the temperature, therefore, provides more heat to both reactions. This results in a shift in the equilibrium: more available heat favors the endothermic reaction taking place, and therefore more water vapor is formed, and equilibrium occurs at a higher vapor pressure. In other words, the maximum water vapor content in air increases with temperature [9].

Relative humidity

The concept of relative humidity follows from an understanding of the saturation curve: it is the water vapor partial pressure relative to the saturation vapor pressure for a given temperature. This can be expressed in the following equation:

$$rh = \frac{p^{H_2O}}{e_s} \tag{2.1}$$

where rh is the relative humidity, p^{H_2O} the water vapor partial pressure, and e_s the saturation pressure, generally given by the Sonntag formula [36]:

$$e_s = exp\left[\sum_{i=1}^{4} a_i T^{i-2} + a_7 ln(T)\right] \tag{2.2}$$

where coefficients a_i were experimentally determined for ice and water saturation, and are given in Table 2.1.

Coefficient	Above water	Above ice
a1	-6.0969385E+03	-6.0245282E+03
a2	2.1240964E+01	2.9327070E+01
a3	-2.7111930E-02	1.0613868E-02
a4	1.6739520E-05	-1.3198825E-05
a7	2.4335020E+00	-4.9382577E-01

Table 2.1: Experimentally determined coefficients used in the Sonntag formula [9].

The Sonntag formula allows us to express the water saturation pressure (vapor pressure at 100% relative humidity) as a function of temperature for ice and liquid phases respectively. This yields the saturation curves shown in Figure 2.6.

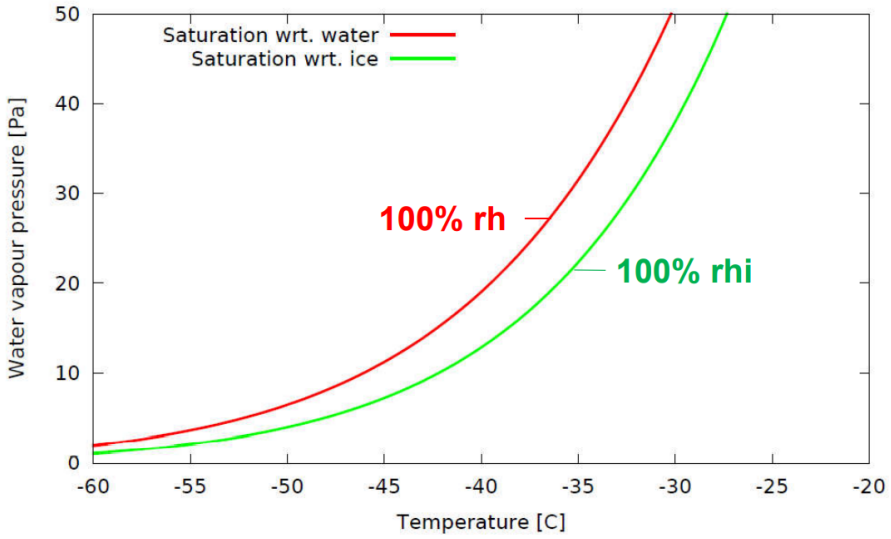

Figure 2.6: Saturation curves of water vapor above water (red) and ice (green) as a function of temperature [9]

Prediction method and underlying assumptions

In his 1953 paper "The Formation of Exhaust Condensation Trails by Aircraft", Appleman made use of these saturation curves to develop his criterion for the prediction of contrail formation, later called the Schmidt - Appleman Criterion, as his work built on and formalized that of Schmidt's 1941 paper "Die Entstehung von Eisnebel aus den Auspuffgasen von Flugmotoren".
His prediction method rests on three basic assumptions:

1. Contrails are composed of ice crystals
2. Water vapor must pass through the liquid phase before forming ice crystals
3. For a distinct trail, a minimum visible water content of 0.01 gm^{-3} is required.

The first two assumptions relate to the formation of a contrail, and the third only to its persistence and visibility once formed. Together with the gained understanding of **relative humidity** and **saturation curves** for water and ice in air, this leads to the postulation of a criterion for the prediction of contrail formation: **The Schmidt - Appleman Criterion (SAC)**.

The mixing process of the engine exhaust with ambient air can be represented by a **mixing line** between exhaust and ambient conditions. This line is drawn on the same water vapor pressure - temperature graph as in Figure 2.6. The relation between this mixing line and the water and ice saturation curves then allows the prediction of contrail formation based on the assumptions mentioned above.

- The first assumption requires ambient conditions to be between the ice and water saturation curves: Ambient conditions below ice saturation will result in sub-saturation and no condensation. Ambient conditions above water saturation will result in water droplets being formed instead of ice crystals.

- The second assumption requires the mixing line to intersect with the water saturation curve. If this does not occur, then the water vapor never passes through the liquid phase, and the ice crystals will not be formed.

- If a linear mixing line is also assumed, a derivation can be made for the slope G of this mixing line, taking into account aircraft and engine properties, exhaust conditions, and ambient pressure. This derivation starts from the basic expression of slope G is given in Equation 2.3 [9]. Drawing a line from ambient conditions in the P-T graph with slope G will then reveal whether the aforementioned conditions for contrail formation are met.

$$G = \frac{p_e^{H_2O} - p_a^{H_2O}}{T_e - T_a} \tag{2.3}$$

with	$p_e^{H_2O}$	Exhaust water vapor partial pressure
	$p_a^{H_2O}$	Ambient water vapor partial pressure
	T_e	Exhaust temperature
	T_a	Ambient temperature

The conditions in the engine exhaust used in Equation 2.3 are not generally known, and it is more convenient to express the mixing line slope in other characteristics that *are* known, such as efficiency and water vapour emissions index. To this end, a derivation can be made, resulting in a new expression for the mixing line G, given in Equation 2.4:

$$G = p_a c_p \frac{M_{air}}{M_{H_2O}} \frac{EI(H_2O)}{(1-\eta)Q} \tag{2.4}$$

with	p_a	Ambient pressure
	c_p	Air constant pressure heat coefficient
	$\frac{M_{air}}{M_{H_2O}}$	Air to water molar mass fraction ratio
	$EI(H_2O)$	Engine Emission Index of water
	η	Aircraft propulsive efficiency
	Q	Fuel heat content

An example of a mixing line resulting in persistent contrail formation is the red line shown in Figure 2.7.

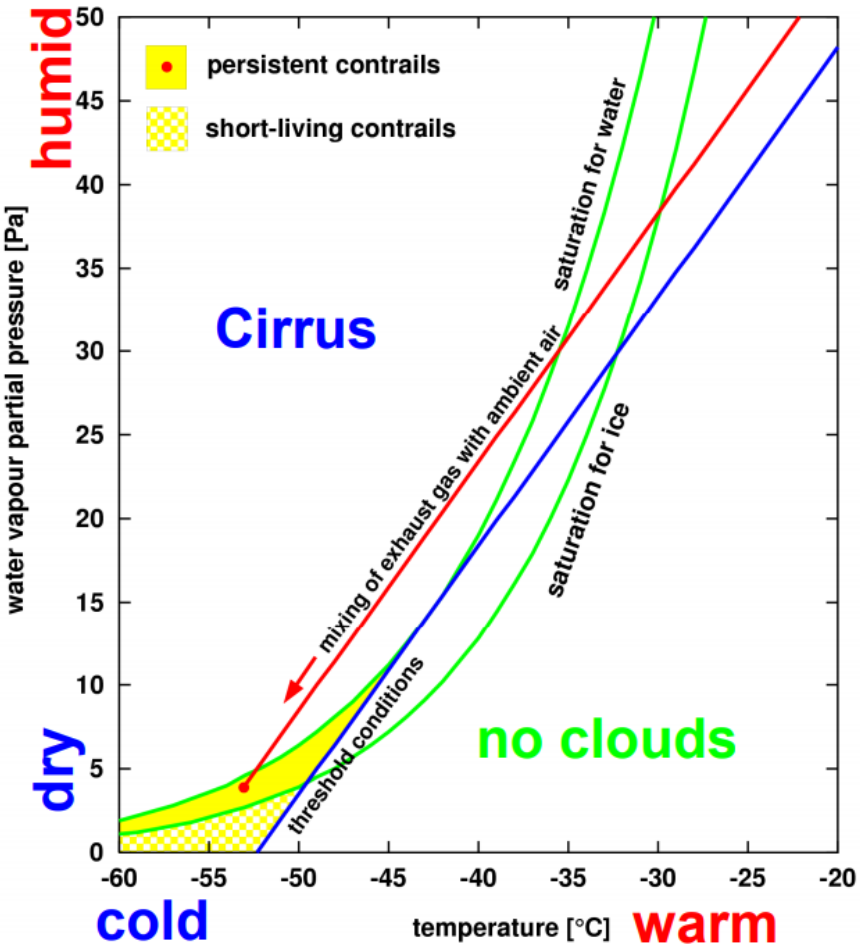

Figure 2.7: Example of a mixing line resulting in persistent contrail formation (red) as well as threshold conditions for contrail formation for mixing lines with the same slope (blue) [9]

Factors influencing Mixing Line Slope

When examining the expression for G given in Equation 2.3, it can be seen that the variable factors are contained in the fraction $\frac{EI(H_2O)}{(1-\eta)Q}$. These factors can be divided into two categories: aircraft dependent and fuel dependent factors.

Fuel dependent factors

- Emission index $EI(H_2O)$.A higher water emission index results in a steeper mixing line and therefore higher likelihood of contrail formation, as could be expected.
- Fuel heat content Q. This parameter correlates to the heat content, and by extension, exhaust temperature of the engine. When examining the graph shown in Figure 2.7, it can be concluded that higher exhaust temperature indeed results in a lower mixing line slope, and a lower likelihood of contrail formation.

Aircraft dependent factors

The aircraft dependent factors influencing contrail formation can be summarized in the single parameter η, representing overall propulsive efficiency, and defined by Equation 2.5.

$$\eta = \frac{Power\ output}{Rate\ of\ work\ input} \tag{2.5}$$

The appearance of $(1-\eta)$ in the expression for the mixing line slope can be interpreted as the fraction of total work performed by the engine that is *not* used for propulsion, and must therefore be left in the exhaust

plume itself. A higher overall efficiency, then, results in a colder (lower energy content) exhaust plume. Again examining Figure 2.7, it can be concluded that this results in a steeper mixing line (the same conclusion can be drawn from Equation 2.3).

Limitations of Current Methods

Aside from the assumptions related to the necessary mixing line criteria for persistent contrail formation that were stated in section 2.4, the SAC is also based on two assumptions for predicting the mixing line itself: Firstly, that mixing is **instantaneous**, and secondly that it is **isobaric**. These assumptions result in a linear mixing line. At the time of development of the SAC, this was a reasonable assumption. However, with the evolution of engine technology, more specifically the ever increasing bypass ratio seen in recent decades, it is fair to question the validity of these assumptions. This was indeed examined by Peters in 1993 [31]. However, the expanded formulas were developed empirically, lacking physical justification. Therefore, while useful for predicting contrail formation of existing aircraft in the 1990s, they do not provide much benefit for designing new aircraft engines or assessing modern civil aircraft contrail formation. Clearly, a need exists for a better understanding of contrail formation from a physical perspective.

2.5. Exhaust Mixing Physics

One of the key aspects of this research will be to model the flow field in the exhaust of a High Bypass Ratio turbofan engine. This requires an understanding of the physical phenomena present in the mixing process between co-axial turbulent jets. The typical flow field for such a mixing process is treated here, followed by a summary of additional factors that influence the characteristics of this flow.

Typical Flow Field

A schematic depiction of the flow field of a coaxial jet can be seen in Figure 2.8. It can be divided into three main regions: The initial merging zone, the intermediate zone, and the fully merged zone. Their definitions and characteristics are as follows:

- **Initial Merging Zone:**:
  Immediately behind the nozzle exit is the initial merging zone. It ends where the secondary (outer) jet potential core disappears. This region is therefore characterized by the appearance of both primary and secondary potential cores. Additionally, Ko and Kwan showed that the radial distance from the center line to the jet outer boundary grows linearly with axial distance from the nozzle exit [18].

- **Intermediate Zone:**
  With the disappearance of the secondary potential core comes the introduction of a shear layer between the inner and outer jet. This transition marks the start of the intermediate zone. Here, the flows from the inner and outer mixing region mix together. The end of the intermediate zone is marked by the reattachment point.

- **Fully Merged Zone:**
  The start of this region is marked by the reattachment point, and it continues downstream. The coaxial jets have mixed together and now behave similarly to a single jet in this zone.

2.5.1. Additional Factors influencing flow characteristics

Some simplifications and assumptions were made in order to analytically describe the near-field region of a coaxial jet. In this section, the most influential factors that were left out are treated in a qualitative fashion.

Diameter Ratio

The diameter ratio β is given by:

$$\beta = \frac{D_o}{D_i} \tag{2.6}$$

with D_o and D_i the diameters of the inner and outer jet respectively. This ratio mainly influences the length of the outer potential core. Increasing β results in a greater outer potential core length.

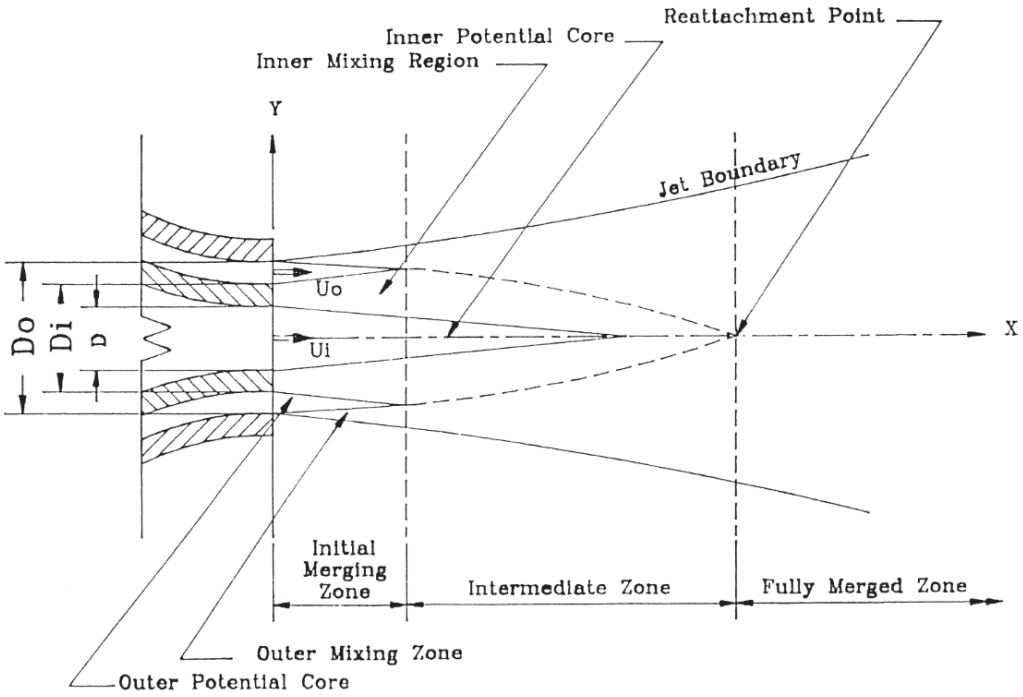

Figure 2.8: Flow field of a coaxial jet [40]

Momentum thicknesses of boundary layers at engine nozzle
In their 1992 paper, Dahm et al. investigated the vortex structures in the near field of a coaxial jet for a velocity ratio smaller than unity [5]. They found that a smaller the momentum thickness of the boundary layers between the jets, corresponding to a thinner boundary layer, resulted in faster rollup of the shear layers in the inner and outer mixing layer. Buresti et al. found similar results in 1994, relating the momentum thickness to the Strouhal number of the vortices within the mixing layer [3]. A thinner boundary layer led to a higher frequency of the vortices and Kelvin-Helmholtz instabilities.

Swirl
The influence of swirl on the development of the flow field in the near-field of a coaxial jet was examined by Ribeiro et al. in 1980 [32]. They found that in the presence of swirl, the coaxial jet developed faster than in the absence of swirl. They posited that this was "due to the mixing layer and vortex shedding that occur in the region downstream of the separation wall between the two streams" [32].

Limitations of Current Methods

The currently existing literature in the field of coaxial jets mostly relates to (from an aviation perspective) low Reynolds number flows, with the highest observed case being in the order of $Re = 10^4$. This is one or two orders of magnitude below what is expected to occur in the near-field flow behind the exhaust of a turbofan. This makes it difficult to predict or compare the behavior of the exhaust flow to existing literature. However, this is mainly a concern for the verification and validation of an eventual mixing model, and will be addressed at that time by finding experimental data or running the simulation at lower Reynolds numbers as a method of comparison to existing literature.

2.6. Research Questions and Objective

Now that a complete picture of the relevant research fields and their limitations has been obtained, the Research Questions and Research Objectives for the upcoming research can be defined.

Research Questions

From the background described in this chapter, and the remaining gaps in current research, the following research questions can be distilled:

1. What is the effect of the mixing physics of core & bypass flow on contrail formation from modern High Bypass Ratio (HBPR) aircraft turbofan engines?
   (a) To what extent does HBPR exhaust mixing deviate from isobaric, instantaneous mixing?
   (b) What is the effect of non-instantaneous non-isobaric mixing on the condensation process?
   (c) What is the influence of key design parameters (such as) Bypass Ratio (BPR) and Overall Pressure Ratio (OPR) on exhaust mixing physics?
2. How can the Schmidt-Appleman Criterion (SAC) be extended or improved to better predict contrail formation from HBPR aircraft turbofan engines?
   (a) How accurate is the current, broadly used criterion in predicting contrail formation from HBPR engines?
   (b) What modifications or extensions can be implemented to improve the accuracy of the SAC for these engines?

Research Objective

The main research objective of this thesis is:

To estimate the impact of engine configurations on contrail formation by analyzing the physics of the mixing process between core and bypass flow through engine performance modelling and exhaust flow simulation.

The sub-goals that need to be achieved for the main objective to be reached are as follows:

1. Develop an engine performance model that accurately predicts the conditions at the core and bypass exit.
2. Develop a mixing physics model that accurately predicts the evolution of humidity, pressure, and temperature within the core and bypass flow.
3. Use the models to predict the mixing lines of modern high bypass ratio turbofans and compare the results to existing literature.
4. Draw conclusions on the accuracy of assumptions underlying the SAC.
5. Make recommendations for the improvement of contrail formation prediction from modern HBPR turbofan engines.

3

Research Setup and Modelling Approach

The previous chapter has resulted in the formulation of two main research questions. These are to be answered by working towards five research objectives. This chapter will briefly describe the approach taken in the current research for achieving these objectives and thus answering the research questions.

3.1. Modelling Framework

To achieve the research objective, a modelling framework has been developed for use in the current research. This is useful for structuring the work to come. Once the model has been completed in accordance with this framework, it will be used to generate results for a case study to prove its validity. Consequently, this modelling framework, and the overview of it as given in this section, can be used to generate results for any other case in future research.

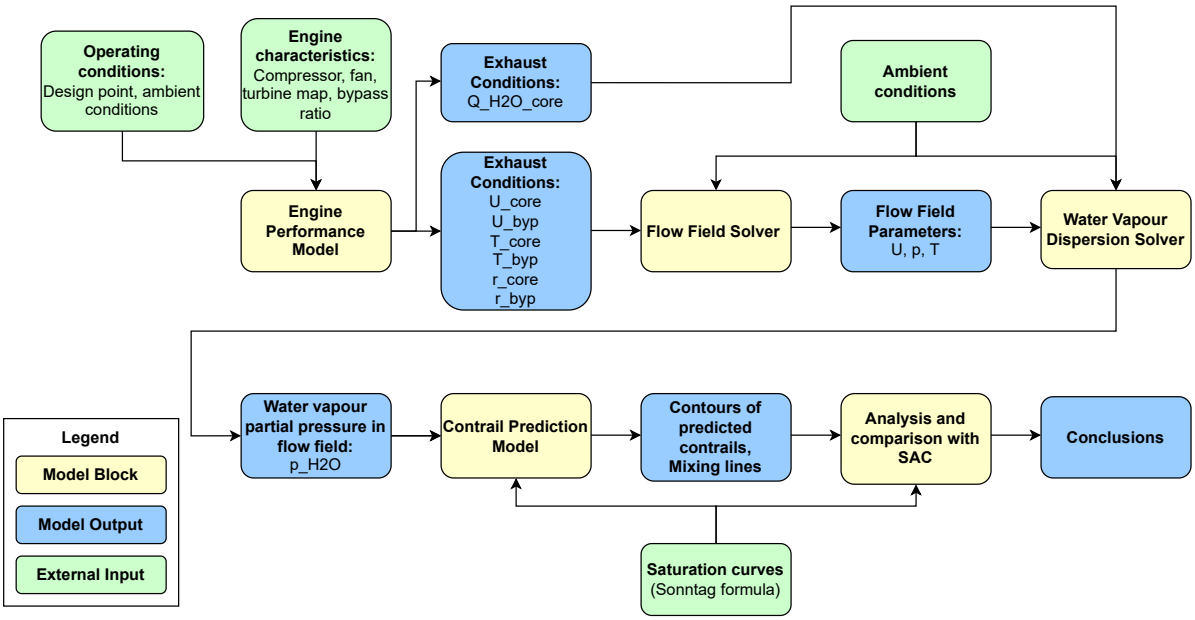

Figure 3.1: Flowchart describing the modelling approach for the current research. Here, the model blocks are shown in yellow, external inputs in green, and model outputs in blue.

For each of the model blocks shown in Figure 3.1, the objective and approach can be summarized as shown in Table 3.1:

Model block	Objective	Approach
Engine Performance Model	Generate output of flow parameters at core and bypass nozzle exits for the given engine type and ambient conditions	1. Use a gas turbine cycle analysis tool to set up a model that is representative for a given engine 2. Run the model at cruise conditions to generate flow parameters required for the next step
Flow Field Solver	Predict the evolution of pressure and temperature within the core and bypass flow	1. Investigate the flow field in the exhaust of a High Bypass Ratio Turbofan in increasing levels of complexity 2. Determine the level of complexity required to accurately resolve the flow field for the relevant conditions 3. Take the outputs of the Engine Performance Model as Boundary Conditions for the modelling of the flow field 4. Resolve the flow field at the required level of complexity to generate contours of flow field variables temperature and pressure
Water Vapour Dispersion Solver	Predict the evolution of water vapour partial pressure within the core and bypass flow	1. Use the outputs of the Engine Performance Model to calculate the water vapour content in the exhaust and ambient air 2. Model the dispersion of this water vapour in the flow field generated by the Flow Field Solver 3. Calculate the water vapour partial pressure based on the water vapour content and pressure in the flow field
Contrail Prediction Model	Use the outputs of the previous models to generate contrail contours and mixing lines	1. Define criteria for formation of contrails based on flow field parameters from previous modelling steps 2. Determine relative humidity in the flow field by comparing water vapour partial pressure to the saturation curves with respect to water and ice 3. Apply criteria to generate contrail contours in the exhaust flow field 4. Track water vapour partial pressure and temperature from the exhaust to draw mixing lines
Analysis and Comparison with SAC	Draw conclusions with respect to the accuracy of the SAC for modern turbofan engines	1. Compare mixing lines from the Contrail Prediction Model to the SAC mixing line for the same case 2. Analyze the results and explain the differences 3. Draw conclusions on the accuracy of the SAC and its underlying assumptions

Table 3.1: Overview of the framework modelling blocks, their objectives, and their approach

3.2. Overview of Chapters

The development of the modelling blocks, along with their respective verification & validation processes, results, and conclusions, is detailed in the upcoming chapters. First, chapter 4 describes the Engine Performance Model. Second, the development of the Flow Field Solver is treated in chapter 5. Consequently, chapter 6 describes the Water Vapour Dispersion Solver and Contrail Prediction Model, as well as a comparison of results with the SAC. Finally, chapter 7 draws conclusions from the results and makes recommendations for the improvement of contrail formation prediction from modern UHBPR engines, as well as recommendations for further research.

4

Engine Performance Modelling

4.1. Introduction

This chapter describes the work done for the first block in the overall modelling framework: the Engine Performance Model. For this purpose, a gas turbine cycle analysis tool is used. The main advantage of such a tool is that it allows for the modification of a single variable such as the bypass ratio. This provides a more scientifically rigorous analysis than the comparison of various engines with different bypass ratios from literature or industry data, because there is no way to isolate the change of a single variable in such an approach. Every engine will be different in various aspects to another engine, not just in its bypass ratio. Additionally, the performance module can be easily validated by recreating an existing engine and comparing its characteristics to known data from this engine.

First, the choice for the software tool to be used is explained in section 4.2. Consequently, the working principles of this tool are treated in section 4.3.Next, in section 4.4, the resulting model setup for the Leap-1A case study is described, followed by a treatment of its validation in section 4.5. In section 4.6, the results from this case study are shown, followed by the conclusions from the current modelling step in section 4.7. The place of the Engine Performance Model within the larger framework can be seen in Figure 4.1.

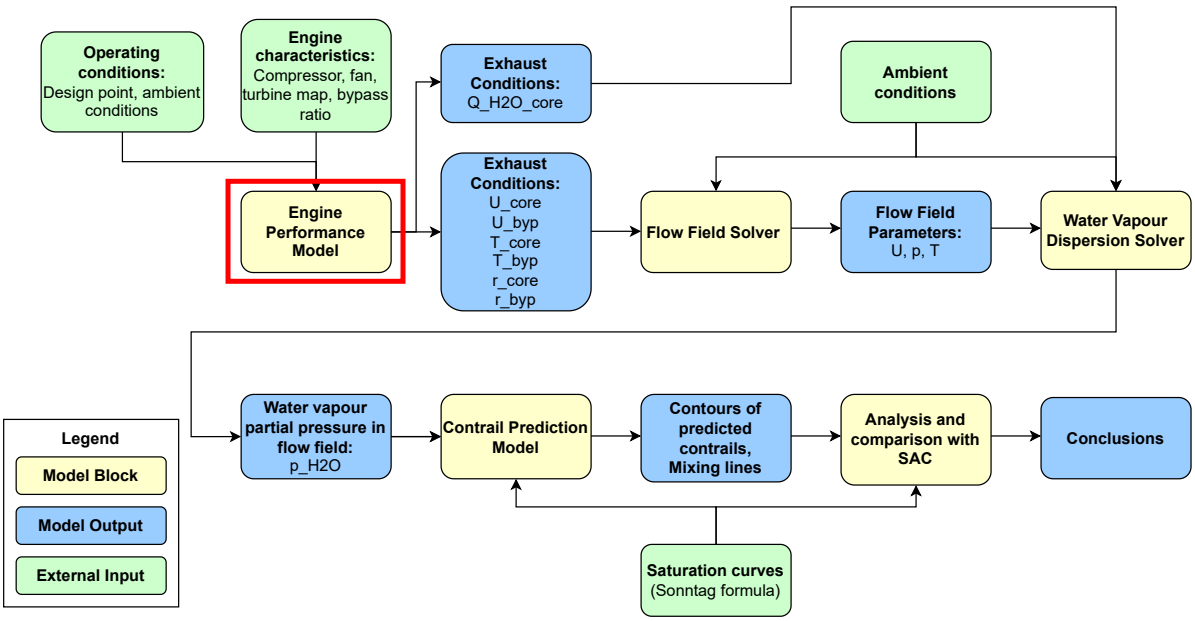

Figure 4.1: Current modelling step in the overall framework

4.2. Choice of Software

For the modelling of the exhaust plume from a given engine, it is necessary to first know the flow conditions in the jets emerging from the core and bypass nozzle of this engine. To achieve this, use is made of an Engine Performance Model. For this research, the choice was made to use the Gas Turbine Simulation (GSP) tool, developed by NLR. Its main advantages can be summed up as follows:

- GSP is flexible and modular in nature, allowing for different configurations and modifications to existing models.
- Compared to alternatives such as pyCycle, it is more user friendly by virtue of its GUI.
- As one of the longest existing and most used tools, it has detailed and deep capabilities.
- A body of knowledge around GSP is already available to the author, including an existing model for use in a case study.

This tool will be used to predict the flow conditions in the exhaust plane of the engine, specifically the temperature, velocity, pressure, and water vapour content. For comparison purposes, an investigation into the capabilities of an alternative tool, pyCycle, is shown in Appendix F.

4.3. Working Principles of GSP

For the current research, the Gas Turbine Simulation Program (GSP) tool developed by NLR was used. [27] Its working principles are treated in this section.

GSP is a well established and long-standing industry tool for modelling gas turbine cycles. Its development finds its origins at the Delft University of Technology in 1975. Its current iteration has been developed in Delphi, whose Object Oriented nature provides ease of adaptation and customization. Additionally, contrary to pyCycle, it features a detailed Graphical User Interface (GUI). An example of a model for a turbofan with afterburner shown in this GUI can be seen in Figure 4.2. In this example, the flexibility and modular nature of the software can be observed. The GUI allows any configuration of components to be generated and run at multiple design - and off-design conditions. [27]

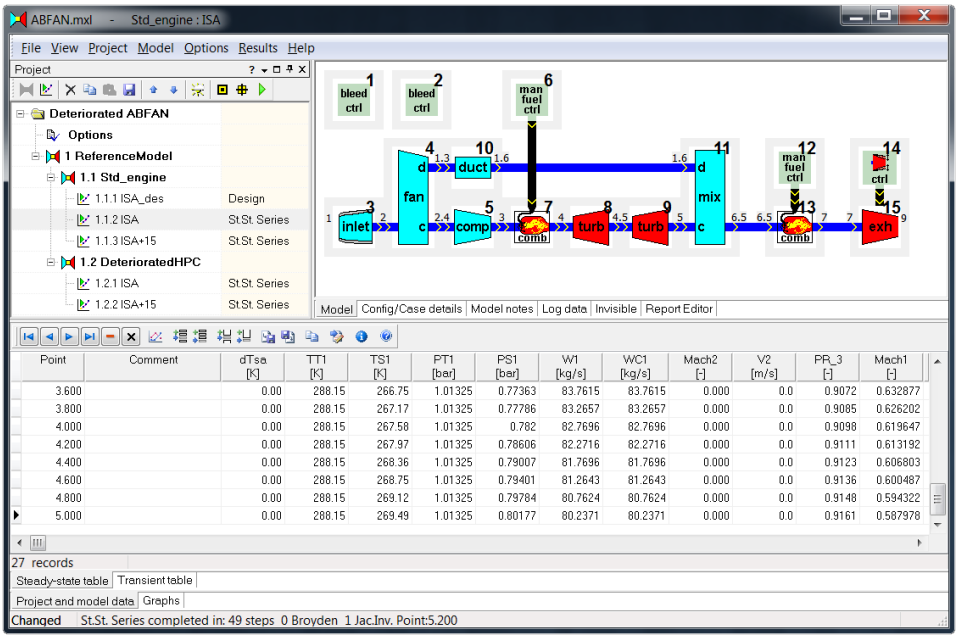

Figure 4.2: Example of an afterburning turbofan designed in GSP and shown in the native GUI [27]

The program functions using a series of 0-D (parametric) components. This means that average values for flow parameters are calculated for every such component. This is done with a combination of aerothermodynamic equations and performance maps, which can either be selected from the generic, built-in

maps or specified by the user for a particular engine or component. By linking the components together, parameters are then passed from one component to the next based on the configuration.

The modelling process for an engine at a given flight condition can be summarized as follows. First, the components are given physical design values and performance parameters by running a Design Condition, for which typically SLS conditions are used. Consequently, the model can be run at as many Off-Design conditions as required. With respect to design optimization, GSP is not specifically developed to facilitate this, as it is not built on gradient-based optimization.

4.4. Leap-1A Case Study

For the purposes of validation as well as applicability to real cases, an existing High Bypass Ratio engine is modelled, namely the CFM Leap-1A engine. The resulting GSP model can be seen in Figure 4.3.

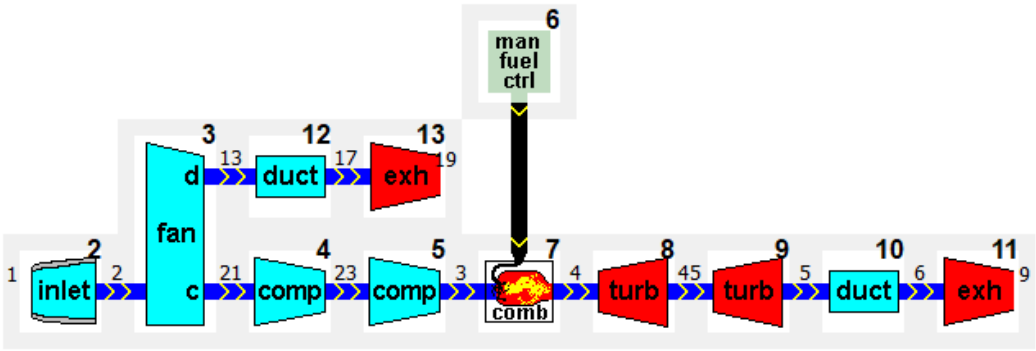

Figure 4.3: Leap-1A engine modelled in GSP

The components are numbered individually from 1 to 13. As can be seen in the figure, generic component types are used in multiple locations where necessary. The component numbering has no physical meaning. However, also visible in smaller font is the station numbering, which conforms to standard practices, summarized in Table 4.1.

Station number	Location
1	Engine intake
13	Fan exit
17	Cold propelling nozzle inlet
19	Cold propelling nozzle exit plane
2	Fan front face
21	Low pressure compressor front face
23	High pressure compressor front face
3	High pressure compressor exit
4	Combustor exit plane
45	Low pressure turbine nozzle guide vane leading edge
5	Low pressure turbine exit
6	Hot nozzle front face
9	Hot propelling nozzle exit plane

Table 4.1: Nomenclature and numbering for engine stations as used in the GSP model for the Leap-1A engine [33]

4.4.1. Modelling Approach

To obtain the desired parameters from a GSP model for a given operating condition, a baseline design condition is first set up, so the model can be validated against known performance parameters in this condition. The validated model can then be run at the desired operating conditions, which are labelled an "off-design point" in the tool. The validated engine characteristics operating at this off-design point will then produce the engine parameters at every station in the engine.

4.4.2. Operating Conditions

Because the objective of this research is to examine cases in which contrails are likely to be formed, the operating conditions need to be that of an aircraft in cruise. These operating conditions are summarized in Table 4.2. For completeness, the baseline design conditions used for the model sizing are included in the first row, followed by the cruise conditions at which the case study is performed in the second row.

Condition	**Psa**	**Tsa**	**Macha**	**Vta**	**Pta**	**Tta**
$[-]$	$[bar]$	$[K]$	$[-]$	$[ms^{-1}]$	$[bar]$	$[K]$
Design (SLS)	0.988	279.80	0.00	0.00	0.988	279.80
Off-Design (Cruise)	0.23842	218.808	0.780	231.316	0.35636	245.433

Table 4.2: The baseline design conditions and conditions at cruise for the GSP model Leap-1A case study

4.5. Validation

The GSP model used for the case study of the Leap-1A engine has been provided by Dr. Yin. It has been externally validated by the original researchers. Their validation efforts showed that, when comparing the Thrust Specific Fuel Consumption (TSFC) of the model to reference data from the real engine, this metric is overestimated by a margin of 1.7%. The researchers conclude that the model therefore shows good agreement with the real Leap-1A engine. [39]

4.6. Results

The results of running the GSP model of the Leap-1A at the operating conditions specified in Table 4.2 are given in the form of flow parameters for the core nozzle and bypass nozzle exits, shown in Table 4.3 and Table 4.4 respectively. The complete set of output parameters from the GSP model is more extensive, but only the relevant values within the context of this research are shown here. These values are passed on to the next step of the model as Boundary Conditions.

Condition	**TS9**	**H9**	**S9**	**PT9**	**PS9**	**V9**	**Ageom8**	**Ageom9**
[-]	$[K]$	$[kJkg^{-1}]$	$[J(kgK)^{-1}]$	$[bar]$	$[bar]$	$[ms^{-1}]$	$[m^2]$	$[m^2]$
Design (SLS)	750.03	-533.16	7936.20	1.28	0.988	337.62	0.2433	0.2433
Off-Design (Cruise)	579.95	-454.42	8026.70	0.368	0.238	391.62	0.2433	0.2433

Table 4.3: Flow parameters at the engine core nozzle exit plane as predicted by the GSP model for the Leap-1A engine case study, at baseline design conditions and cruise conditions

Condition	**TS19**	**H19**	**S19**	**PT19**	**PS19**	**V19**	**Ageom18**
[-]	$[K]$	$[kJkg^{-1}]$	$[J(kgK)^{-1}]$	$[bar]$	$[bar]$	$[ms^{-1}]$	$[m^2]$
Design (SLS)	282.46	-34.91	6840.85	1.48	0.988	264.32	1.2697
Off-Design (Cruise)	229.64	-27.67	6980.59	0.514	0.272	303.91	1.2697

Table 4.4: Flow parameters at the engine bypass nozzle exit plane as predicted by the GSP model for the Leap-1A engine case study, at baseline design conditions and cruise conditions

4.7. Conclusion

From the work done on the Engine Performance Model within the current framework, the following conclusions can be drawn. Firstly, the investigation into the use of pyCycle, as shown in Appendix F, has shown its potential as a design tool for modern gas turbines, especially when used as part of a larger multidisciplinary design optimization process. This is due to its modular capabilities and gradient-based solution algorithms. In addition, its open-source nature is attractive for accessibility and affordability reasons. However, its relative novelty and lack of supporting features such as extensive documentation and GUI make it less desirable for implementation into the current framework. As a long-standing, widely used tool in the industry, GSP has clear advantages in these areas. As its drawbacks with respect to multidisciplinary design optimization and proprietary nature of the software when compared to pyCycle are not as relevant as these advantages for its

implementation in the current framework, GSP was selected as the superior tool for this use case.

With respect to modelling an existing engine to use as a case study for the current research, GSP offers one additional advantage: An existing, validated model of the CFM Leap-1A engine was already available. This meant the remaining work for the current modelling step entailed the generation of results for a relevant ambient condition, in this case cruise conditions at an altitude of 10668 m. The relevant results, namely the ambient conditions and flow conditions at the core and bypass nozzles respectively, have been extracted from the GSP output. These results will be used as Boundary Conditions in the next modelling step, namely the Flow Field Solver described in chapter 5.

5

Flow Field Solver

5.1. Introduction

This module will describe the most crucial and complex phenomenon in the project, namely the mixing of coaxial core and bypass jets within the ambient flow. The position of this module within the overall framework is shown in Figure 5.1. The modelling framework that is being developed is meant to be as accessible and replicable for future research as possible. It is therefore desirable to divide the work into increasing levels of complexity and software requirements. At each level, an assessment is made regarding the validity of the model for the purposes of this research. If its predictive capabilities are deemed insufficient, or its assumptions too far-reaching, the next step is taken. In this case, the distinction is made between 1-dimensional (1D), 2-dimensional (2D) Parametric, 2D Finite Element, 2D Semi-Empirical, 3-dimensional (3D) Computational Fluid Dynamics (CFD), and 2D Axisymmetric CFD analysis. To illustrate the research steps performed to get to a working Flow Field Solver and to document the knowledge and experience gained from it, the approach to each of these steps is described respectively in the upcoming sections.

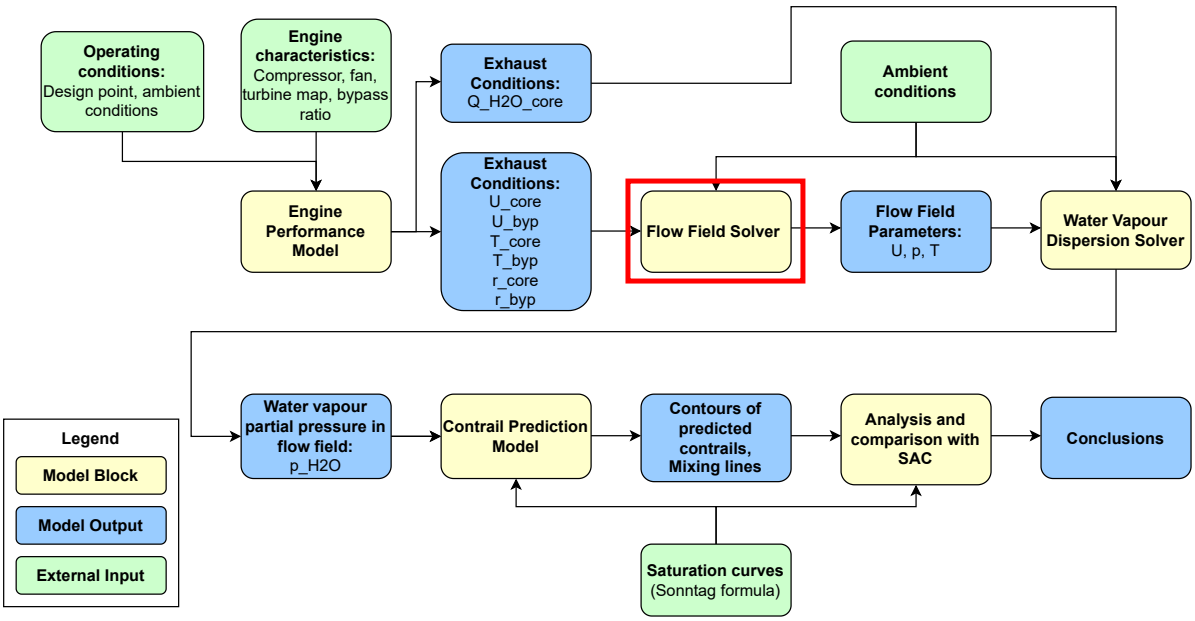

Figure 5.1: Current modelling step in the overall framework

5.2. 1D Approach

The 1D approach examines the current mathematical foundation of the SAC, which is itself a 1D method. The underlying assumptions are questioned, options to include a term for the instantaneous mixing ratio

at the engine exit are proposed, and the effect on the mixing line is examined. The advantage of taking this as a starting point, is that it is still closely connected to a physical and mathematical basis, and allows for underlying simplifying assumptions to be questioned and improved upon in the following steps. The main limitation of the 1D approach is that the evolution of the mixing process between the core and bypass flow as function of distance from the exhaust plane is not addressed. This means the deviation from instantaneous mixing can be examined, but not isobaric mixing, nor the assumption of a straight mixing line.

5.2.1. Revision of SAC using instantaneous mixing ratio

To gain an understanding of the influence of the assumption of instantaneous mixing on the derivation of the mixing line slope, resulting in the expression given in Equation 2.4, the concept of a mixing ratio MR is introduced here, after which a new derivation is shown. This mixing ratio is defined as a value between 0 and 1, indicating the fraction of bypass flow that is instantaneously mixed with the core flow at the engine exit. In other words, the bypass mass flow m_b used in the revised SAC can be redefined by Equation 5.1:

$$m_b = m_c \cdot BPR \cdot MR \tag{5.1}$$

where m_c is the core mass flow and BPR the engine bypass ratio. Using this definition, the slope is calculated along the same lines as before, starting from the definition first stated in Equation 2.3 and restated below:

$$G = \frac{p_{e_{H_2O}} - p_{a_{H_2O}}}{T_e - T_a}$$

From here, the numerator and denominator are calculated separately. The water vapour partial pressures $p_{e_{H_2O}}$ and $p_{a_{H_2O}}$ are derived from their respective mass fractions q_a and q_e according to the expressions:

$$p_{a_{H_2O}} = p_a * q_a * \frac{M_{air}}{M_{H_2O}} \tag{5.2}$$

$$p_{e_{H_2O}} = p_a * q_e * \frac{M_{air}}{M_{H_2O}} \tag{5.3}$$

The water vapour mass fraction q_a depends on ambient conditions, while engine exhaust mass fraction q_e is given by Equation 5.4, using the mixing ratio definition given in Equation 5.1:

$$q_e = \frac{m_c(1 + BPR * MR)q_a + m_f * EI_{H_2O}}{m_c(1 + BPR * MR) + m_f} \tag{5.4}$$

The denominator $T_e - T_a$, meanwhile, can be derived from the definition of enthalpy h as follows:

$$T_e - T_a = \frac{h_e}{c_p} - \frac{h_a}{c_p} \tag{5.5}$$

$$= \frac{1}{c_p} \frac{(1-\eta)m_f Q}{m_c + m_b + m_f} \tag{5.6}$$

Again, the mixing ratio definition from Equation 5.1 can be used to arrive at the expression:

$$T_e - T_a = \frac{1}{c_p} \frac{(1-\eta)m_f Q}{m_c(1 + BPR * MR) + m_f} \tag{5.7}$$

Finally, the numerator and denominator can be combined, resulting in the newly calculated mixing line slope $G_{revised}$:

$$G_{revised} = p_a c_p \frac{M_{air}}{M_{H_2O}} \frac{EI_{H_2O}}{(1-\eta)Q} \tag{5.8}$$

5.2.2. Sensitivity analysis of SAC wrt. mixing ratio

As the observant reader may have expected, this revised expression is identical to the original mixing line slope definition given in Equation 2.4. Mathematically, this can be explained by the fact that the mixing ratio influences the numerator and denominator to the exact same extent. Physically, it means that, while the engine exit conditions do shift for a mixing ratio of 0.5, to a lower temperature and water vapour partial pressure, this shift occurs exactly along the mixing line defined by slope G.

The conclusion that can be drawn is that current methods are not only limited by the assumption of instantaneous mixing, but also that of a straight mixing line. This is why more detailed examination of the actual physical mixing process is needed.

5.3. 2D Parametric Approach

The 2D approach is based on the plume models and jet entrainment models that are typically used in pollutant dispersion modelling. Using the data generated by the engine performance module as inputs, a Python model has been developed. Python is selected as a programming language for three main reasons: Firstly the flexibility that it offers in its wide range of possible applications, secondly the popularity of the language, making many resources and access to others' experience available, and thirdly the author's own experience and comfort with the language. The main improvement this step will bring is the possibility of tracking the evolution of flow properties and water vapour content at different radial and axial stations in the exhaust flow. This allows the assumption of a straight mixing line to be examined.

The assumptions underlying the 2D parametric approach are described in subsection 5.3.1, followed by the modelling approach in subsection 5.3.2, and limitations along with suggested improvements of this approach in subsection 5.3.3.

5.3.1. Assumptions

The assumptions underlying the plume and entrainment model are as follows:

Entrainment model assumptions

- The entrainment of air into the plume follows the behavior of pure jet entrainment, as the high velocity of the exhaust
- The exhaust is unchoked: Exhaust pressure is equal to ambient pressure.
- The bypass jet and core jet have uniform distinct velocities at their respective nozzle exit planes.

Plume model assumptions

- Water vapour content is distributed in a Gaussian curve in the core flow
- Bypass jet water vapour content is equal to ambient conditions
- Entrainment only occurs inwards (no transfer of water from core to bypass)

Some of these assumptions, especially the unchoked exhaust and only inward transfer of water vapour, are not very realistic, and deserve further attention. However, in this stage of the research, they allow the opportunity for a good first approximation of mixing in two dimensions, with simple equations that have a clear physical basis.

5.3.2. Modelling approach

The modelling steps taken in this stage are described below:

1. Split mixing into two phases: the mixing of the core jet with the bypass jet, and the bypass jet with the ambient flow.

2. Calculate entrained mass flow for both phases using pure jet assumptions, where entrainment velocity v_e is defined by Equation 5.9:

$$v_e = \alpha * (U_i - U_o) \tag{5.9}$$

with α the entrainment coefficient, equal to 0.057 for a pure jet. [7] The entrained mass flow can then be calculated by assuming a circular surface area with radius R and axial length dx:

$$\dot{m}_e = \rho AV = \rho \cdot 2\pi R \cdot dx \cdot v_e \tag{5.10}$$

3. Use the definition of enthalpy h_0 to calculate the change of total temperature T_0 due to entrained flow. The total enthalpy H_0 is weighed by the respective mass flows to arrive at a new total temperature:

$$h_0 = c_p \cdot T \tag{5.11}$$
$$H_0 = h_0 \cdot \dot{m} \tag{5.12}$$

4. Assume a Gaussian distribution of water vapour in the exhaust plume.

5.3.3. Limitations and Suggested Improvements

After developing the 2D parametric approach towards resolving the flow field in the engine exhaust, it is clear that the current iteration still has several limitations that preclude it from answering the research questions with sufficient confidence. These limitations can be summarized as follows:

Jet Entrainment Model limitations:
This model provides a good initial impression of the processes involved in the mixing of core and bypass, and bypass and ambient air. However, it still has several key shortcomings.

- The three separate flows (core, bypass, ambient) are only resolved as a single average value over their radius. While this is still an improvement in terms of tracking properties in axial direction when compared to the 1D analysis, it is not possible to validate this model to the required degree of confidence. As we know from literature, the flow field for a co-axial jet is complex and mixing between flows occurs primarily in the turbulent shear layers. This phenomenon is not captured by the jet entrainment model.

- The assumptions of unchoked flow and constant density, while necessary for the 2D model, are not accurate for the cruise conditions the model is meant to represent. Because the mixing in the model depends on mass flows and velocities, and these in turn depend on the aforementioned assumptions, this inaccuracy carries over to the end result.

- In reality, the flow in the near-field of the engine exhaust is highly turbulent. The above 2D approach does not incorporate any turbulence models, and therefore misses the turbulent phenomena involved in the mixing process.

Plume Dispersion Model limitations:
In a rotationally and axially symmetric simple jet, it is reasonable to assume the concentration of a given species disperses according to a Gaussian curve. However, as the flow field in question is more complex, it also has its shortcomings in this case. Most important is the assumption that air is only entrained inward. Along with the averaging of flow properties over the radius of each separate flow (core, bypass, ambient), this means that the Gaussian curve only applies to the core jet. While the jet, and therefore the concentration curve, does expand when moving downstream, this still fails to properly address the merging of bypass and core flows to a single, self-similar jet as described in literature. By extension, the concentration of water is not properly dispersed along the entire radial axis of the jet, especially further downstream, which significantly limits the accuracy of mixing lines predicated upon this model.

Suggested Improvements
Based on the limitations described above, a number of additional steps can be taken to improve the accuracy:

- Introduce an ambient co-flowing annular jet to represent the forward velocity of the aircraft at cruise

- Improve the physical basis for entrainment coefficient α. Introduce variable entrainment coefficient dependent on age of the jet (or axial distance)
- Investigate the impact of incompressible assumptions on the entrainment rate
- Introduce microphysical processes to ice crystal formation prediction
- Improve heat content modelling by taking into account enthalpy changes due to water phase changes

To address some of these shortcomings, a 2D Finite Element model was developed. This is treated in the following section.

5.4. 2D Finite Element Model

The plume model and entrainment model provide a good first estimate for the entrainment of ambient air into the exhaust flow with a solid physical basis. However, the assumptions required for this approach are such, that the results cannot be considered reliable or conclusive enough. Therefore, the logical next step is to reduce the number of assumptions and simplifications, in order to more accurately represent real exhaust flow. Two assumptions that deserve to be revisited are:

- The exhaust is unchoked
- Entrainment only occurs inwards (no transfer of water from core to bypass)

In most cases, the flow will not have fully expanded at the engine nozzle plane, and as explained in section 2.5, the mixing of coaxial jets is more complex than just "entrainment of flow from outer to inner jet". To address these shortcomings, a module for Python called FEniCS is employed, which was designed for the purpose of solving partial differential equations (PDEs) through the Finite Element (FE) method. The main advantages of this approach are:

- Written in Python, allowing for seamless integration into the overall model structure.
- Stays close to the real physics by implementing custom PDE's and boundary conditions directly.
- Output format of data allows for visualization of flow field.

The inputs required by the FEniCS sub-module are:

- Ambient conditions (pressure, temperature, air density, and water vapour content)
- Exhaust conditions (pressure, temperature, air density, and water vapour content)
- Exhaust dimensions (inner and outer jet radius)

The following assumptions are required:

- Incompressible flow
- No turbulent phenomena
- 2D flow

The calculations are then divided into three main steps: First, the Navier-Stokes equations are used to determine the velocity and pressure field in the exhaust flow. Secondly, the advection-diffusion equations are imposed on this flow in order to find the dispersion of water vapour. Finally, the temperature field also needs to be known.

Finite Element Model Results

An example of flow field output generated by the FEniCS model can be found in Figure 5.2. From this image, the shortcomings of this approach can be observed. By modelling the velocity and pressure according to the Navier-Stokes equations without providing a turbulence model, the closure problem is not addressed and the solution remains unstable. It is conceivable that these shortcomings could be addressed by including additional Finite Element equations. However, this would effectively amount to building a custom CFD solver from scratch, which is not feasible or desirable within the context of the current research. Therefore, this method is discarded as a valid option for the Flow Field Solver sub-module of the current model.

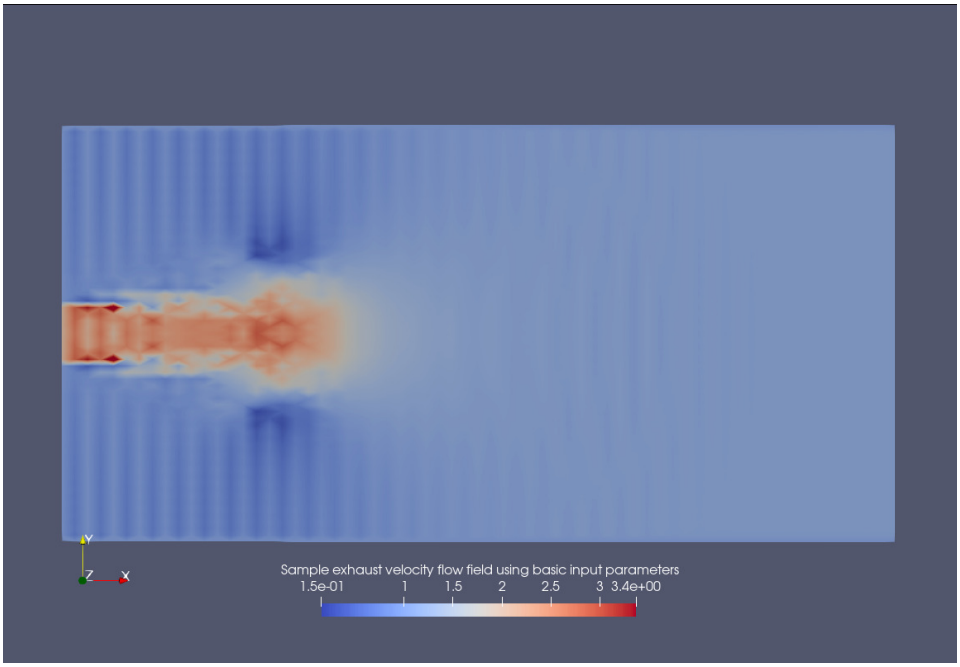

Figure 5.2: Velocity field produced by the FEniCS model

5.5. 2D Semi-Empirical Approach

The semi-empirical approach aims to combine the simplicity of mathematical models with empirical knowledge from previous experimental research. The current model is largely based on the Morton-Taylor-Turner (MTT) entrainment law as well as basic conservation of mass and momentum. The approach can be summarized as follows:
Divide the domain into discrete cells. Consequently, obtain an accurate description of the velocity distribution within the exhaust and thus the flow of mass from cell to cell by applying the MTT entrainment law. Then use these values to describe heat transport based on flow of enthalpy, and calculate the temperature at each point within the exhaust. A plume dispersion model can then be implemented over this flow field to predict the spreading of water vapour from the core. This finally allows for the drawing of mixing lines on a $p_{H_2O} - T$ graph for comparison with the SAC mixing lines.
The mathematical derivation of this approach is quite extensive, and is therefore not included in the main body of this chapter. It can be found in Appendix A. In theory, the computational efficiency and mathematical elegance of this method are attractive and promising. However, in practice, obtaining physically meaningful and validated results has proved challenging. Therefore, the decision has been made to switch to a Computational Fluid Dynamics Approach. However, the efforts done in pursuit of the Semi-Empirical Approach are kept in the current document as inspiration for future research.

5.6. 3D CFD Approach

To address the shortcomings of the previous approaches, the decision was made to switch to Computational Fluid Dynamics (CFD). This approach should yield the following advantages with respect to the previous attempts:

- CFD simulations can account for pressure gradients and compressible flow, meaning initial conditions, including a choked exhaust, can be accurately represented.
- Turbulence modelling is a core component of CFD methods. This means the regions of greatest interest, namely turbulent shear layers where mixing primarily occurs, can be resolved and investigated in detail.
- Once the flow field properties are determined, the dispersion of water vapour can be modelled accurately and relatively easily with an advection-diffusion solver over the given velocity field.

- Validating a CFD model can be done by recreating (experimental) cases for which the results are known from literature.

5.6.1. Choice of Software

In this stage of the research, the OpenFOAM software is selected to be used. [29] Because of its open-source nature, it is available not only for the author during this research, but also for any potential further steps undertaken by the author after losing access to student resources after graduation, or by other researchers interested in building on the results of this thesis. In addition, it is a widely used tool for which many resources and experiences by other users are freely available. The author is also already familiar with the capabilities of the software beforehand.

5.6.2. Modelling Approach

The simulation of the exhaust mixing process contains two main steps: First, a compressible Navier-Stokes solver is used to accurately resolve the key flow field variables, namely velocity, temperature, pressure, and turbulence properties. Secondly, an advection-diffusion solver is applied to model the dispersion of water vapour within this flow field. An advantage of this approach is that finally, the assumption of isobaric mixing is removed. In addition, turbulent mixing is properly taken into account. A limitation of this approach is the sensitivity to the quality of input data and proper setup: small errors in either step can lead to non-physical or inaccurate output data. Validation of this step is therefore key.

5.6.3. Navier-Stokes Solver

The flow in the exhaust jet of a turbofan engine can best be described as a high Reynolds transonic 3D axisymmetric steady field. To model this flow accurately, therefore, a steady-state approach should be employed, with a turbulence model and grid capable of accurately resolve the mixing in the shear layers between the co-annular jets. The modelling choices deemed most suitable, and therefore selected for this task, are summarized in Table 5.1.

Choice of software	OpenFOAM v2106
Solver	rhoSimpleFoam (compressible, steady-state)
Turbulence Model	$k-\omega-SST$
Grid generation	Gmsh Structured OH-mesh

Table 5.1: Choices and settings for the 3D RANS model

Turbulence Modelling

For the turbulence model, there are two main criteria: It should perform well for external flows, but also be able to resolve flows with strong pressure gradients, as the core, bypass and ambient flows all have distinct pressures. Traditionally, the $k-\epsilon$ model is chosen for external flows, while the $k-\omega$ model is deemed more suitable for internal flows and those with strong pressure gradients. The $k-\omega-SST$ model combines the advantages of both, and is therefore chosen for this simulation. [14]

Mesh Generation (Gmsh)

The initial grid generation for this model was done using the open-source tool Gmsh, which allows structured meshes to be generated from a user-defined script defining the geometry and blocking setup. As mentioned above, the exhaust jet is assumed to be axisymmetric. Therefore, it would be a waste of computational resources to model the entire circular domain. In fact, if swirl and other 3D effects did not play a role, there would be no need for 3D modelling at all. However, because these effects do need to be taken into account, a 3D flow field is required. The solution with respect to computational efficiency is to model only a wedge of the flow field, and impose periodic boundary conditions along its two edges. This approach has the advantage of keeping the 3D character of the flow field, while minimizing the amount of cells required in the circular direction.

The other main characteristic of the flow field setup, is the definition of inlet conditions. The inlet is defined as the plane immediately behind the engine, and is therefore divided into three inlet fields: the core jet in the center, above it the bypass jet, and finally the ambient inlet above that. These inlets take their conditions directly from the Engine Performance model block. The circular upper part of the domain is defined as the Far

Field, and the far end of the domain in axial direction is the Outlet, where ambient static pressure is imposed. The resulting grid setup can be seen in Figure 5.3 and Figure 5.4.

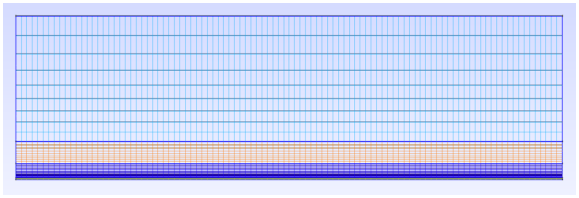

Figure 5.3: Side view of the RANS computational domain

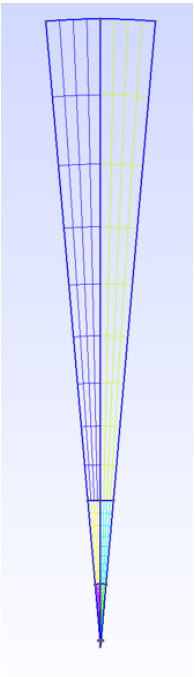

Figure 5.4: View of the inlet of the RANS computational domain

Mesh Generation (snappyHexMesh)
Although Gmsh is an efficient tool for generating highly structured meshes, it has its limitations when applied to complex geometries. If the nozzle geometry itself is included as part of the mesh, therefore, other options need to be explored. One widely used tool is snappyHexMesh, which is native to OpenFOAM. The meshing process for this case can be summarized as follows:

1. 3D nozzle geometry is generated in a CAD tool. In this case, SolidWorks was used. The exhaust geometry is modelled as two simple concentric converging pipes.

2. Surface geometry is extracted from the CAD geometry, and separated into the different boundary elements: Core nozzle, bypass nozzle, core inlet, bypass inlet, far field, and outlet. This was done in Blender.

3. A dictionary is made called the "snappyHexMeshDict", in which the domain is defined, geometry elements are imported, and all meshing controls are set up.

4. This dictionary is passed to the snappyHexMesh module of OpenFOAM, which generates a 3D unstructured mesh based on the dictionary settings

5. A check is done on the meshing parameters to ensure quality.

Boundary Condition Definitions
In order to accurately resolve the flow field, the proper boundary conditions need to be defined. It is important that these boundaries have a sound physical basis, and that they place the necessary amount of constraints on the system of equations to be solved. If the problem is under-constrained, a steady-state solution will never be reached, and if it is over-constrained, a physical solution cannot be found. Table 5.2 and Table 5.3 show the chosen conditions for this simulation.

Boundary	**p**	**T**
Core & Bypass Inlets	Total Pressure	Total Temperature
Ambient inlet	Total Pressure	Total Temperature
Nozzle walls	Zero gradient	Adiabatic
Far Field	Wave Transmissive	Wave Transmissive
Outlet	Wave Transmissive	Wave Transmissive

Table 5.2: Boundary conditions for the 3D OpenFOAM simulation (Pressure and temperature)

Boundary	**U**	**k**	**ω**
Core & Bypass Inlets	Zero gradient	Turbulent Intensity	Mixing Length
Ambient inlet	Zero gradient	Turbulent Intensity	Mixing Length
Nozzle walls	No-Slip	Wall function	Wall function
Far Field	Wave Transmissive	Zero gradient	Zero gradient
Outlet	Wave Transmissive	Zero gradient	Zero gradient

Table 5.3: Boundary conditions for the 3D OpenFOAM simulation (Velocity, turbulence kinetic energy and specific turbulence dissipation rate)

5.6.4. Advection-Diffusion Solver

Once the general flow field parameters (U, p, T, ν_t) are known within the exhaust, they can be used as input for the next step: calculating the water vapour dispersion within this field. To this end, a custom advection-diffusion solver was developed based on the OpenFOAM native scalarTransportFoam solver. The main reason a custom solver needed to be set up, is that the native solver only takes into account molecular diffusion. In the case of transonic, highly turbulent flow, this type of diffusion is negligible compared to the transport of species due to turbulent structures. Therefore, a turbulent diffusion term needs to be taken into account. The development of this solver is explained in this section.

The Partial Differential Equation for Advection - Diffusion of a species concentration C can be stated as follows:

$$\frac{\partial C}{\partial t} = \nabla \cdot (D \nabla C) - \nabla \cdot (\mathbf{U} C) + R \tag{5.13}$$

Here, D represents the diffusivity, U the velocity field, and R the increase in concentration due to reactive processes. In the steady-state case, and assuming no chemical reactions present, this equation simplifies to:

$$\nabla \cdot (D \nabla C) - \nabla \cdot (\mathbf{U} C) = 0 \tag{5.14}$$

In the scalarTransportFoam solver, the diffusivity term D is given a fixed value, and is meant to represent molecular diffusivity. As explained above, this term needs to be adjusted to include turbulent diffusion. Therefore, a new diffusion term is introduced: effective diffusion D_{eff}:

$$D_{eff} = D_{molecular} + D_{turbulent} \tag{5.15}$$

The turbulent diffusion coefficient D_{eff} is defined here as equal to the eddy diffusivity K, derived from the turbulent Schmidt number Sc_t by the following relation:

$$D_{turbulent} = K = \frac{Sc_t}{\nu_t} \tag{5.16}$$

5.6.5. Conclusions

Using the approach described in this section, OpenFOAM modelling was extensively attempted. However, including third party consulting, using powerful grid computing provided by the TU Delft, and attempting over 500 different meshing strategies, providing a converged solution was not possible. While the final results for this thesis were eventually generated using a different approach, which is described in section 5.7, future researchers or students may still benefit from the OpenFOAM work done. This is available upon request to the author.

5.7. 2D Axisymmetric CFD Approach

The methods described in the previous sections, while promising in certain respects, all have their own shortcomings that ultimately made them unfeasible for the current research. The early 1D and 2D approaches have the advantage of being computationally inexpensive, as well as physically and mathematically simple. However, they also miss key phenomena such as turbulence and therefore their results are unreliable. The 3D approach using OpenFOAM does capture these more complex phenomena, but is computationally too expensive and producing a properly verified and validated model with this approach requires more time and resources than are available for this thesis.

Because the geometry of an engine exhaust consists of two circular concentric nozzles, another approach can be employed: 2D Axisymmetric Computational Fluid Dynamics modelling. Here, a domain is examined that represents a 2D slice of a cylindrical coordinate system, where symmetry conditions are assumed in angular direction. This approach combines the computational advantage of 2D analysis with the accuracy of a fully 3D model. Going forward, this is the final approach used within the framework of the current research. In the upcoming sections, the application of this method to the Leap-1A engine case study is described.

5.7.1. Choice of Software

For this analysis, the choice was made to use the ANSYS Fluent software. As a professional, commercial package, this software provides the advantage of having a detailed GUI, extensive documentation, and a wide range of modelling options. It also has a native, built-in function for 2D axisymmetric analysis.

5.7.2. Geometry Definitions

A basic engine exhaust geometry is designed at the lower left corner of the domain. The dimensions are such that they match the parameters obtained from the Engine Performance Model. That is to say, the inner and outer radii of the core and bypass nozzles are calculated to correspond to the nozzle areas given by GSP, while also maintaining an overall exhaust geometry modelled after a typical High Bypass Ratio engine shape. [38]. This results in the nozzle geometry shown in Figure 5.5. For the purposes of creating a reliable, structured mesh, the geometry is simplified with respect to a real engine shape. Firstly, the exhaust conditions given by the Engine Performance Model are for the exit planes of the core and bypass nozzles respectively. This is reflected in the geometry by making these planes the boundaries of the model. Secondly, the curved surface of the engine nacelle is replaced with a straight outer nozzle wall. Lastly, the ambient inlet boundary is placed at the start of the engine nacelle.

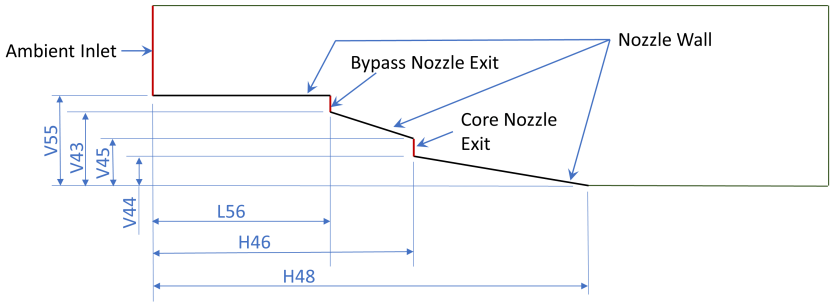

Figure 5.5: Leap-1A engine geometry for the 2D Axisymmetric Model. The dimensions shown here are quantified in Table 5.4. Within the overall domain shown in Figure 5.6, this geometry is represented by the red area in the lower left corner.

For this model to be representative of the mixing in the exhaust of a given engine, the flow parameters from the core and bypass nozzles need to correspond to those given as outputs from the Engine Performance Model. For most parameters, this is a matter of implementing the correct boundary conditions, as will be described in subsection 5.7.4. One parameter that is not directly implemented in the boundary conditions, but is of significant importance to the mixing process, is the mass flow coming from the core and bypass nozzles. As mass flow $\dot{m}$ perpendicular to a given area A is given by:

$$\dot{m} = \rho U A \tag{5.17}$$

and parameters ρ (density) and U (velocity) are both determined by the boundary conditions, defining the cross sectional area A for both core and bypass nozzles is sufficient to ensure matching mass flow to the Engine Performance Model outputs. In the axisymmetric domain, cross sectional area of the nozzles is defined as:

$$A_{core} = \pi(r_{o_{core}}^2 - r_{i_{core}}^2) \tag{5.18}$$

where r_o is the outer radius and r_i the inner radius. As no exact dimensions are known for the engines used as case studies for this research, an assumption is made for the radius of the cone with respect to the core nozzle radius based on examples from literature [38]: cone radius (equal to inner radius r_i of the core nozzle) is assumed to be $\frac{2}{3}$ of the core nozzle radius (equal to outer radius r_o):

$$r_{i_{core}} = \frac{2}{3} r_{o_{core}} \tag{5.19}$$

This allows the nozzle inlet area to be defined solely by the outer radius r_o:

$$A_{core} = \pi(r_{o_{core}}^2 - (\frac{2}{3} r_{o_{core}})^2) \tag{5.20}$$

$$A_{core} = \frac{5}{9} \pi r_{o_{core}}^2 \tag{5.21}$$

From the results of the Engine Performance Model given in section 4.6, area A is known. This allows outer radius r_o and in turn inner radius r_i to be calculated from Equation 5.21 and Equation 5.19 respectively.

A similar approach can be applied to the inner and outer radius for the bypass nozzle. Again, an assumption needs to be made for the inner radius r_i. In this case, the distance between core nozzle outer radius and bypass nozzle inner radius is assumed to be the same as the radius of the inner cone. Remembering that this cone radius is equal to the inner radius of the core nozzle r_i, this allows the inner radius of the bypass to be expressed as follows:

$$r_{i_{bypass}} = r_{o_{core}} + r_{i_{core}} \tag{5.22}$$

The cross-sectional area for the bypass nozzle can again be expressed as a function of inner and outer radius:

$$A_{bypass} = \pi(r_{o_{bypass}}^2 - r_{i_{bypass}}^2) \tag{5.23}$$

Rewriting Equation 5.23 yields the outer radius of the bypass nozzle.

To ensure that the imposition of boundary conditions does not significantly influence the solution, they need to be placed far enough away. The Far Field boundary is therefore placed at 50 times the engine diameter, and the Outlet boundary at 150 diameters. The complete domain is shown in Figure 5.6.

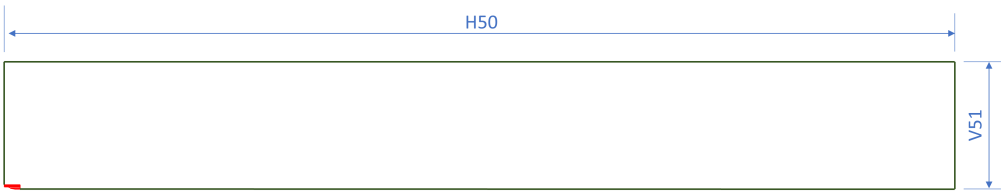

Figure 5.6: Complete domain for the 2D Axisymmetric Model. The red area in the lower left corner represents the nozzle geometry shown in Figure 5.5. The dimensions are specified in Table 5.4.

A complete overview of the dimensions used for the 2D axisymmetric model, corresponding to the definitions given in Figure 5.5 and Figure 5.6, can be found in Table 5.4.

Dimension	Value	Unit
L56	2.01	[m]
H46	3.00	[m]
H48	5.00	[m]
H50	300	[m]
V43	0.833	[m]
V44	0.33	[m]
V45	0.50	[m]
V51	40	[m]
V55	1.0478	[m]

Table 5.4: Domain dimensions for the 2D Axisymmetric model of the Leap-1A Engine

5.7.3. Grid Generation

The first decision to make is whether a structured or unstructured mesh should be designed. Unstructured meshes have the advantage of being quick and easy to generate, as well as applicable to complex geometries. In addition, local grid refinement can be easily achieved by dividing existing elements. However, when solving an unstructured grid, computing times can be significantly higher than for a structured grid due to its complex data structure. A structured mesh has the advantage of simple topology and implementation, and easy quality control. Additionally, the data structure is very simple compared to an unstructured grid, as cells can be simply saved in a 2D array, with each cell connecting to its neighbours in the array. This allows for highly efficient solution algorithms and therefore reduced computing times when compared to an unstructured grid. The difficulty for structured grids resides in properly refining areas of interest and regions close to complex geometries. To address this, use can be made of a multi-block grid.

Clearly, if a structured mesh is able to be generated for a given case, this is the preferred approach based on the above reasoning. It will result in lower computing times and allow for better quality control. Therefore, the model geometry as described in subsection 5.7.2 has already been set up in such a way that multi-block structured meshing is facilitated. The geometry has been made no more complex than necessary. The next step is then to divide the domain into blocks so local refinement can be applied. This division is shown by the yellow lines in Figure 5.7.

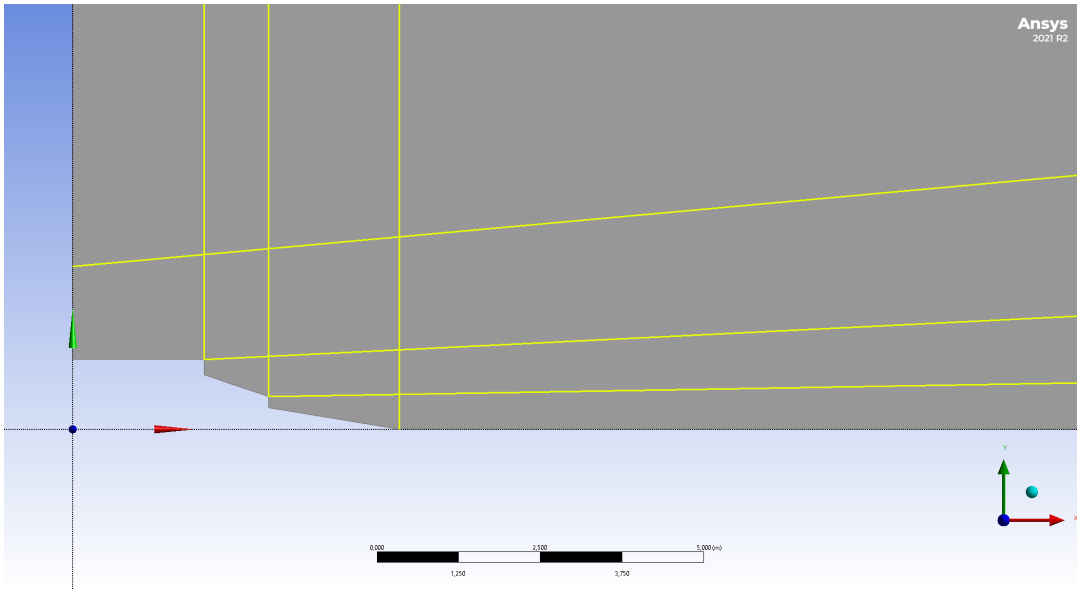

Figure 5.7: Division of the model domain into a multi-block grid

As the domain is now divided into blocks that each have four edges, these edges can be used to size the cells within them to the required degree of refinement. The regions close to the engine in the lower left corner of the domain need the highest level of refinement, while coarser cells can be used further downstream and towards the far field. In the end, the resulting mesh comprises a total of 303 500 quadrilateral elements. The resulting complete grid is shown in Figure 5.8. The refined regions around the core nozzle, bypass nozzle, and complete engine can be seen in Figure 5.9, Figure 5.10, and Figure 5.11 respectively. From these figures, it can be seen that the regions of interest near the engine exhaust indeed have closest mesh spacing. Additionally, the mesh is highly orthogonal in all regions, with a mesh check reporting a minimum orthogonal quality of 0.9465. It can also be seen that some high aspect ratio cells are present, most notably in the upper ambient region above the engine towards the Far Field. This is due to the refinement methods used. In this region, the highest aspect ratio found is 265. This would be unacceptable if it were in a region of interest close to the engine, where larger gradients of flow properties are expected in all directions. However, as gradients in this region of the domain are very small, this aspect ratio is not considered problematic, and the tradeoff with respect to computational efficiency is worthwhile.

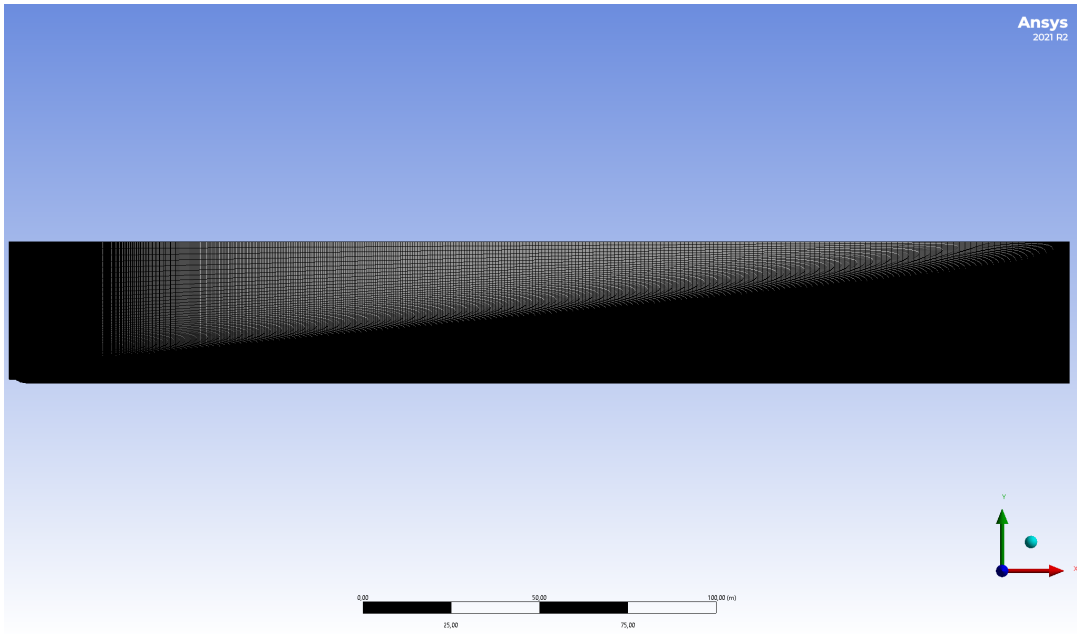

Figure 5.8: Complete mesh for the axisymmetric 2D model of the Leap-1A engine exhaust

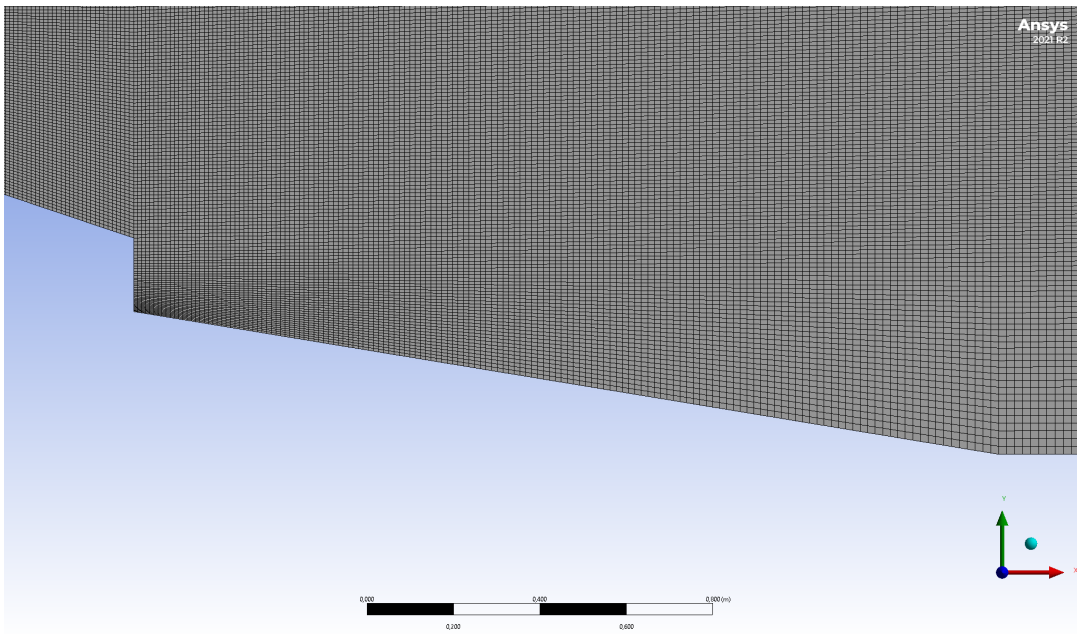

Figure 5.9: Refinement region close to the core inlet within the mesh for the axisymmetric 2D model of the Leap-1A engine exhaust

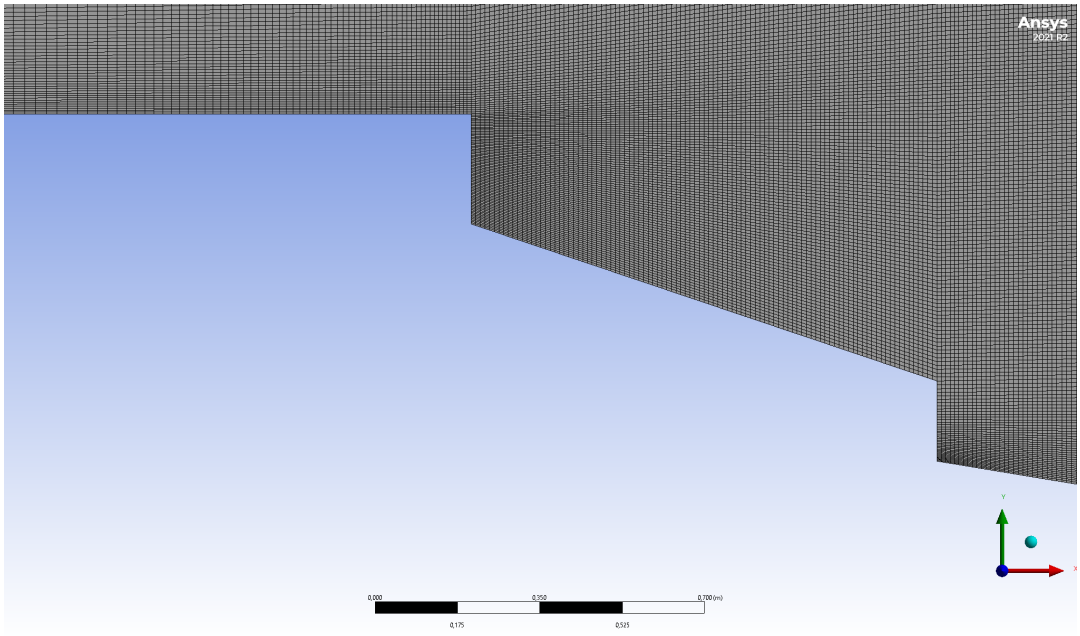

Figure 5.10: Refinement region close to the bypass inlet within the mesh for the axisymmetric 2D model of the Leap-1A engine exhaust

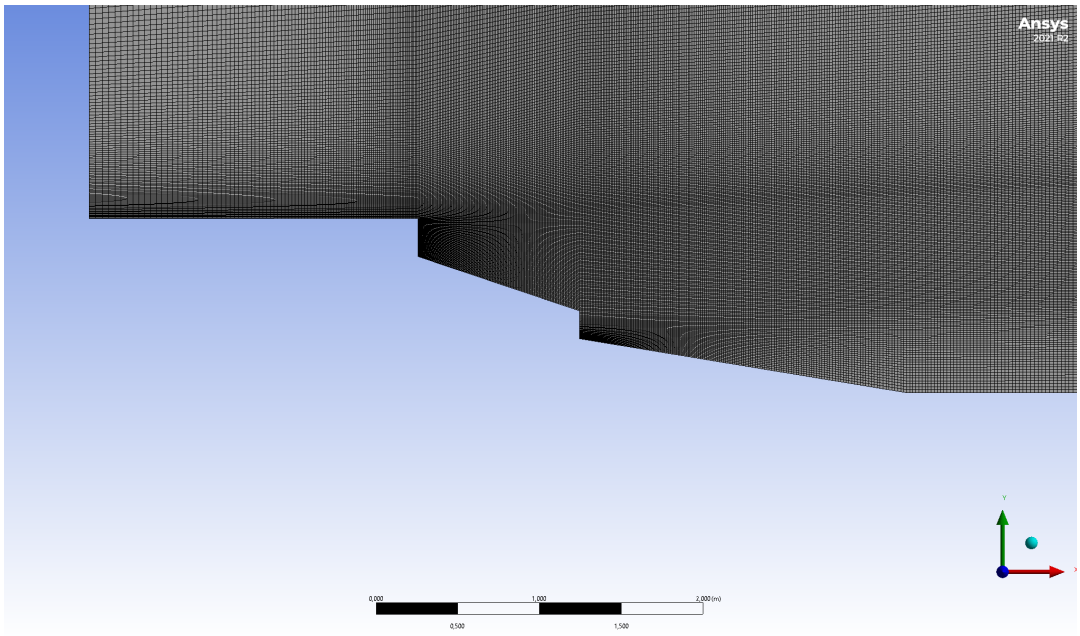

Figure 5.11: Refinement region close to the complete engine within the mesh for the axisymmetric 2D model of the Leap-1A engine exhaust

5.7.4. Boundary Conditions

A summary of the chosen Boundary Condition types is given in Table 5.5. The locations of the boundaries they are applied to can be seen in the accompanying Figure 5.12. The considerations for the choice of boundary conditions are similar to those in section 5.6: They need to be defined such that the model is properly constrained. A comprehensive overview of the values used for the boundaries can be found in Appendix D. The values listed in these tables are those for the case study of the Leap-1A engine at cruise conditions, resulting from the Engine Performance Model described in chapter 4.

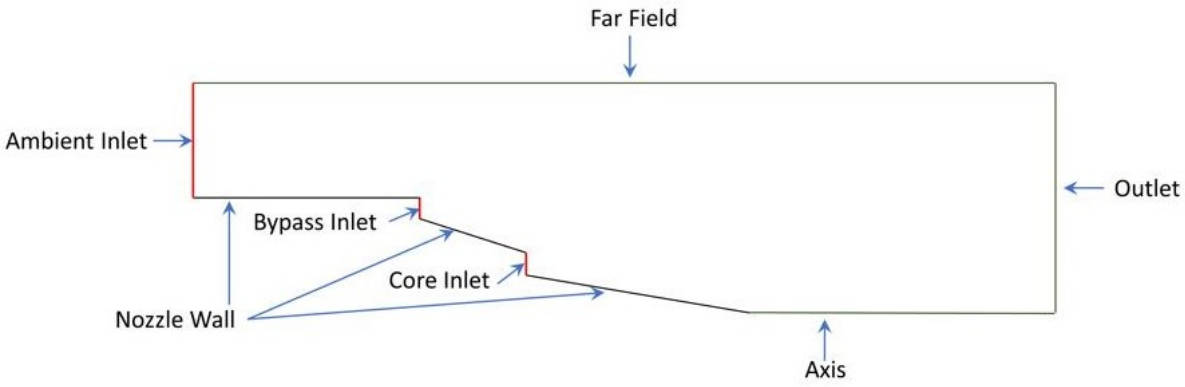

Figure 5.12: Location of the boundary conditions for the Leap-1A Case Study. For clarity, the Far Field and Outlet boundaries are shown in this zoomed in figure. In reality, they are placed at the far upper and right edges of the domain respectively. The full domain is shown in Figure 5.6.

Boundary	Boundary type
Core Inlet	velocity-inlet
Bypass Inlet	velocity-inlet
Ambient Inlet	velocity-inlet
Far Field	pressure-far-field
Nozzle Wall	wall (adiabatic no-slip)
Outlet	pressure-outlet
Axis	axis

Table 5.5: Summary of boundary condition type definitions for the Leap-1A Case Study

5.7.5. Turbulence and Solver Settings

The aim of the CFD simulation is to accurately model the mixing process between core, bypass, and ambient flow in the engine exhaust, so predictions of contrail formation can be made based on its results. Because this flow occurs at high Reynolds numbers, turbulence is an important phenomenon that needs to be modelled properly. Ansys Fluent offers many different turbulence models, suitable for different situations. The main candidates for this simulation are the Spalart - Allmaras, $k-\epsilon$, $k-\omega$, and $k-\omega-SST$ models.

Spalart-Allmaras

As a simple one-equation model designed specifically for aerospace applications, this model is a good starting point. It is known to give good results for boundary layers and wall-bounded flows. Its main drawback is its questionable reliability for free shear flows. As the current research involves co-axially flowing jets with shear layers between them, this is a potential problem.

k*−*ϵ

The $k-\epsilon$ model solves two transport equations to model turbulence while using the Eddy Viscosity proposition to model the Reynolds stress. It is one of the most widely applicable and therefore popular turbulence models. Its main shortcoming is its inaccuracy in predicting separation of boundary layers under adverse pressure gradients. The current research does not involve boundary layers, other than the ones forming over the nozzle walls. However, these are not areas of interest in answering the research questions and in any case,

separation is not expected here. Therefore, the $k-\epsilon$ model is a candidate for this research.

k − ω
Similarly to the $k-\epsilon$ model, the $k-\omega$ model solves two transport equations. However, instead of solving for the turbulence dissipation rate ϵ, it solves for *specific* turbulence dissipation rate ω. This results in a better treatment of adverse pressure gradients in boundary layers, at the cost of the solution being very sensitive to inlet and ambient conditions for turbulence parameters k and ω. In its base form, therefore, it is not ideal for this research, as some level of estimation is required for these parameters. However, there are extensions to this model that can be used most notably the $k-\omega-SST$ model.

k − ω − SST
This model combines the advantages of the $k-\epsilon$ and $k-\omega$ models, resulting in a solution that is better at predicting boundary layers with adverse pressure gradients than $k-\epsilon$ while being less sensitive to initial turbulence conditions than $k-\omega$.

For the verification process, an initial choice is made to use the $k-\omega-SST$ turbulence model. After grid independence has been verified, validation efforts will be made using the different turbulence models. The model that shows the best agreement with results from literature will then be selected for use in the current research.

5.8. Verification

Two methods of verification are employed for the Flow Field Solver in this section. First, the consistency of nozzle parameters from the Engine Performance Model to the Flow Field Solver is performed in subsection 5.8.1. Subsequently, in subsection 5.8.2, a Grid Convergence Study is done to determine the numerical error.

5.8.1. Consistency of Nozzle Parameters

As a first verification step, a check is done for consistency between the current model parameters and the results from the Engine Performance Model described in chapter 4. As mentioned in subsection 5.7.2, the dimensions for the nozzle geometry are based on the geometric area output from the Engine Performance Model, combined with assumptions derived from an example geometry. If the Flow Field Solver is indeed consistent with the Engine Performance Model, these dimensions along with the boundary conditions should result in the same mass flows predicted by the Engine Performance Model.

For a nozzle with cross-sectional area A, the mass flow through this nozzle is given by:

$$\dot{m} = \rho U A \tag{5.24}$$

The velocity U and area A are known inputs for the model. As both pressure and temperature are also known, density ρ can be determined solving the Ideal Gas Law for density:

$$\rho = \frac{p}{R_{gas} T} \tag{5.25}$$

The resulting values for both core and bypass nozzles are summarized in Table 5.6.

Parameter	Core nozzle	Bypass nozzle	Unit
U	391.6165	303.9	$[ms^{-1}]$
A	0.24333	1.26793	$[m]$
p	23842	27160	$[Pa]$
T	579.85	229.63	$[K]$
ρ	0.1432	0.4120	$[kgm^{-3}]$

Table 5.6: Flow conditions at the core and bypass nozzle used for verification of mass flow for the Leap-1A engine

Inserting the parameters from Table 5.6 into Equation 5.24 results in the calculated values for mass flow in

the Flow Field Solver for the Leap-1A engine. They are compared to the mass flow given by the Engine Performance Model in Table 5.7

Parameter	Core nozzle	Bypass nozzle	Unit
Mass flow (Flow Field Solver)	13.64979	159.0009	$[kgs^{-1}]$
Mass flow (Engine Performance Model)	13.64739	158.9886	$[kgs^{-1}]$
Percentage difference	0.018	0.008	[%]

Table 5.7: Comparison of mass flow values predicted by the Flow Field Solver and the Engine Performance Model for the Leap-1A engine

From this comparison, it can be seen that the predicted mass flows correspond with an accuracy in the order of 0.01%. This verifies the consistency of nozzle flow parameters between the Engine Performance Model and the Flow Field Solver.

5.8.2. Grid Convergence Study

When performing a CFD simulation, there will always be a difference between the predicted solution and the actual solution. This difference can be expressed as:

$$\Delta = u_{nature} - u_{discrete} \tag{5.26}$$

$$= (u_{nature} - u_{exp}) + (u_{exp} - u_{exact}) + (u_{exact} - u_{discrete}) \tag{5.27}$$

The first term, $(u_{nature} - u_{exp})$, indicates the difference between the proposed experiment and the natural phenomenon it is meant to represent.
The second term, $(u_{exp} - u_{exact})$, is defined as the modelling error, and is determined by the validation process. It is a measure for the predictive power of the model when compared to an analogous experiment, if it were to provide an exact solution.
The final term, $(u_{exact} - u_{discrete})$, is the difference between the theoretical exact solution and the solution predicted by the numerical model. It is called the numerical error, and determining this error is part of the verification process.
The goal of a grid convergence study is to investigate to which degree the discrete solution is influenced by numerical rather than physical parameters. In the ideal case, a numerical model converges to the exact physical solution. In practice, this is not feasible, because there are always numerical errors present. However, an estimate for the exact solution of certain chosen parameters can be made, and the model's convergence towards these exact solutions observed. If the convergence falls within the asymptotic range, the grid is considered suitable.

Choice of criteria

To achieve a sufficiently complete picture of the grid convergence of this model, a selection of parameters is made. For validation purposes, the velocity field is the most important, while for the subsequent calculations on contrail formation, temperature is the key variable. Therefore, these parameters are evaluated at various stations within the jet.

Order of Convergence

The Order of Convergence refers to the convergence of the solution error as a function of grid spacing. This solution error E is defined as:

$$E = f(h) - f_{exact} = Ch^p + H.O.T \tag{5.28}$$

where f is the solution, C is some constant, h is a measure of the grid spacing, p is the order of convergence, and $H.O.T.$ are Higher Order Terms.

If three simulations with a constant grid refinement ratio r between them are performed, the order of convergence can be evaluated through the following expression:

$$p = ln(\frac{f_3 - f_2}{f_2 - f_1}) ln(r) \tag{5.29}$$

where f_1, f_2, f_3 are the solutions for the respective grid spacings.

Exact solution
Using a Richardson extrapolation, the exact solution can be estimated from the discrete solutions as follows:

$$f_{h=0} = f_1 + \frac{f_1 - f_2}{r^p - 1} \tag{5.30}$$

Grid Convergence Index
To estimate how close the computed value is to the theoretical exact value, the Grid Convergence Index is used. It is a measure for how much the solution changes upon further refinement.

It is defined as:

$$GCI = \frac{F_s|\epsilon|}{r^p - 1} \tag{5.31}$$

where F_s is a safety factor, taken to be 1.25 in this study.

Asymptotic Range of Convergence
By comparing two subsequent Grid Convergence Indices between grids, an assessment can be made on the overall convergence of the solution. If the value of C remains close to constant, the grid is deemed to be within the asymptotic range of convergence. From Equation 5.28, it can be derived that:

$$C = \frac{E}{h^p} \tag{5.32}$$

This expression can be rewritten in terms of the grid convergence indices as follows:

$$C = \frac{GCI_{23}}{r^p GCI_{12}} \tag{5.33}$$

Here, GCI_{23} and GCI_{12} are the grid convergence indices between grid 2 and 3 and grid 1 and 2 respectively. If the value C is close to one, the simulation falls within the asymptotic range of convergence [28].

Results
The results of the convergence study are summarized in the following tables.

Normalized Spacing	$T_{min}[K]$	$T_{max}[K]$	$U_{min}[ms^{-1}]$	$U_{max}[ms^{-1}]$
0.5	224.4444	609.9913	239.4852	416.9799
1	224.5499	607.4865	239.2802	426.847
2	224.0843	607.5970	239.1438	441.3602

Table 5.8: Values of maximum and minimum temperature and velocity along the jet center-line for three levels of grid refinement

Normalized Spacing	$T_{min}[K]$	$T_{max}[K]$	$U_{min}[ms^{-1}]$	$U_{max}[ms^{-1}]$
0.5	222.0064	246.5943	233.6878	268.3096
1	221.2336	243.8846	233.4192	270.3920
2	221.6677	242.9398	233.7809	269.0133

Table 5.9: Values of maximum and minimum temperature and velocity at axial location $\frac{x}{d} = 80$ for three levels of grid refinement

	$T_{min}[K]$	$T_{max}[K]$	$U_{min}[ms^{-1}]$	$U_{max}[ms^{-1}]$
p	2.1418	-4.5026	-0.58778	0.5567
$f_{h=0}$	224.4135	607.3709	238.8726	396.02476
GCI_{12}	0.01721	-0.53697	-0.31975	6.2818
GCI_{23}	0.07593	-0.02379	-0.2129	9.0261
C	0.9995	1.0041	1.0009	0.9769

Table 5.10: Results of the grid convergence study for the values along the jet center-line

	$T_{min}[K]$	$T_{max}[K]$	$U_{min}[ms^{-1}]$	$U_{max}[ms^{-1}]$
p	-0.8320	-1.5200	0.4293	-0.5949
$f_{h=0}$	220.2431	242.4340	234.4627	274.4719
GCI_{12}	-0.9928	-2.1089	0.4145	-2.8709
GCI_{23}	-0.5596	-0.7435	0.5588	-1.8861
C	1.0034	1.0111	1.0012	0.9923

Table 5.11: Results of the grid convergence study for the values at axial location $\frac{x}{d} = 80$

From these results, it can be concluded that for the parameters examined in this study, the grid indeed falls within the asymptotic range of convergence, as C is close to 1 in all cases.

Evolution of parameters with Normalized Grid Refinement

A more visual and intuitive representation of grid convergence can be observed when the minimum, maximum, and average values for velocity and temperature are plotted against the normalized grid refinement, which is defined as the original grid spacing divided by the current grid spacing. In other words, a normalized grid refinement of two corresponds to a mesh two times finer than the original. The results of doing so can be seen in Figure 5.13 and Figure 5.14. In the case of velocity, the average value remains largely constant, while the minimum and maximum show a decline of approximately 10% over the range of normalized grid refinement values from 0.5 to 2. This indicates that the exact solution has not yet been reached. The temperature values show much less variation as a function of grid refinement. The steepest gradient in both cases is in the range of normalized grid refinement from 0.5 to 1, while past a ratio of 1.5 very little change occurs. From this it can be concluded that grid independence is achieved at a normalized grid refinement of 1.5.

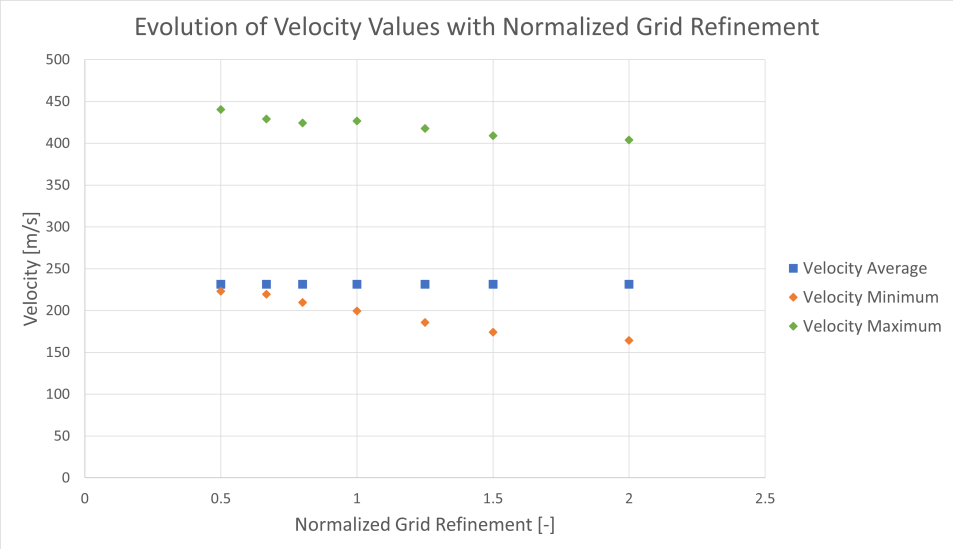

Figure 5.13: Maximum, minimum and average velocity values plotted against Normalized Grid Refinement

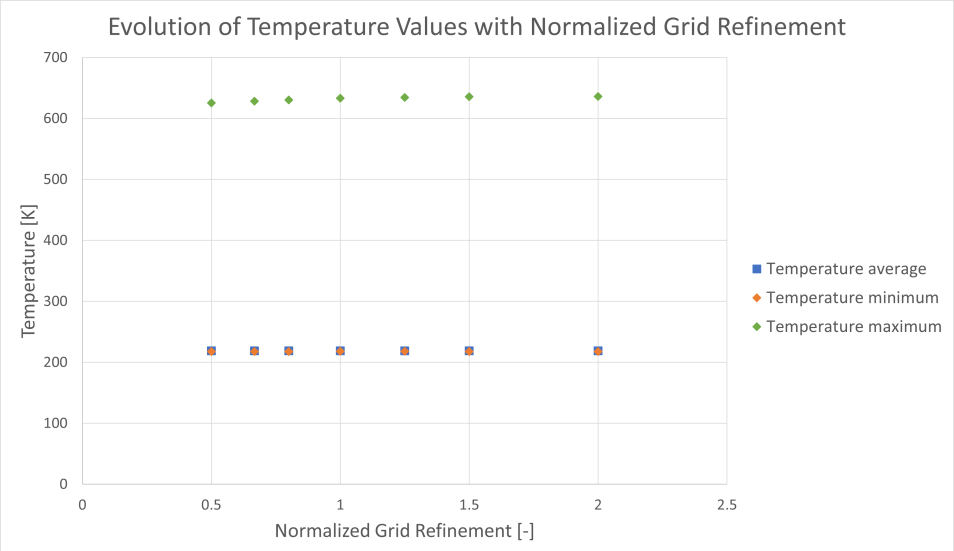

Figure 5.14: Maximum, minimum and average temperature values plotted against Normalized Grid Refinement. It can be seen that average and minimum values are nearly identical for all data points. This is because in the overall domain, nearly all nodes have a temperature equal or very close to ambient conditions.

5.9. Validation

The Flow Field Solver is likely the most critical to the accuracy of the entire research, because of its sensitivity to (in)correct input data and setup. Therefore, it is important to validate it with real experimental data. This is done in the following steps:

1. **Simple free round jet validation.** An experiment from literature replicated with the model settings from this research. The predictive power of the model for the velocity field is determined by comparing the results of similar models with the one from this research as well as the original experimental results. Key parameters in this comparison are the development of self-similarity within the jet, the predicted length of the potential core and overall axial velocity evolution, and the spreading rate of the jet.

2. **Co-flow experiment validation** A transonic round jet in co-flow is replicated using the model settings. Again the results are compared to those of similar models and original experimental data.

3. **Conclusions** are drawn regarding the validity of the model and its predictive power for the velocity field in the near-field of co-axial turbulent jets.

To ensure correct simulation of the flow-field in the exhaust, the model will be set up to replicate an existing physical experimental study that examines co-flow between a jet and a surrounding ambient flow. If resulting velocity fields of the model and experiment match with sufficient accuracy, the model can be said to have predictive power that can be extrapolated to the various cases relevant to this research. Special attention is paid to the influence of the choice of turbulence model in each case.

5.9.1. Simple free round jet Validation (part 1)

For simple round jets as well as co-axial jets, research has been done to show their development into what is defined as a self-similar jet. The concept of self-similarity is briefly introduced here, after which the semi-empirical model's capability to predict self-similarity is compared to experimental results for simple jets.

Self-similarity parameters

The hypothesis of self-similarity posits that, after an initial developing region, the velocity distribution within the jet at a given axial distance from the nozzle does not significantly change in shape anymore. If the shape of the distribution can be plotted at various axial distances with the differences being within a certain margin, the jet is said to have achieved self-similarity.
For the purposes of the current research, a simplified approach to similarity parameters is employed. Because there is no need to compare jets of different diameters and velocities among each other, it is sufficient

to non-dimensionalize the velocity and distance by dividing by the initial jet velocity U_1 and diameter D respectively. This is also the method employed by the literature used in the validation cases.

Model setup
To validate the model's capability for predicting the development of self-similarity, the experiment by Wygnanski & Fiedler [43] is recreated and compared to the experimental results. The turbulence models used for this validation case are the $k-\omega-SST$ and the Spalart - Allmaras model. The boundary conditions for this simulation are shown comprehensively in Appendix D.
Results
The development of self-similarity can be observed in Figure 5.15. The velocity profiles normalized with respect to center-line velocity are shown compared to experimental results from Wygnanski & Fiedler [43]. This indicates that the model shows good predictive power with respect to the downstream development of velocity characteristics for simple round jets.

Figure 5.15: Development of self-similarity in the far-field region of a simple round jet, compared to experimental results [43]

A comparison of turbulence models can be found in Figure 5.16. The simulation was performed for two different models: the Spalart - Allmaras model (S-A) and the $k-\omega-SST$ model. The resulting normalized velocity profiles are shown in comparison to the original experiment, as well as the profiles predicted for the same turbulence models by Bardina et al. [2]. In terms of accuracy, the $k-\omega-SST$ model performs significantly better as it is closer to the experimental results than the S-A model. Additionally, its precision in developing self-similarity is higher than that of the S-A model. A final observation is that both models are more accurate with respect to the original experiment than predicted originally Bardina et al.

Validation summary
From this validation case, three main conclusions can be drawn. Firstly, the $k-\omega-SST$ turbulence model is able to replicate the simple round jet from the experiment with a higher degree of accuracy than the $S-A$ model. Secondly, both models are significantly more accurate than the simulations from literature they were compared to, which used the same turbulence models. And lastly, self-similarity is achieved in the simple jet for both turbulence models. However, the literature that was used as a comparison was published in 1997. As the field of CFD has undergone significant developments and improvement in the past 25 years, this literature cannot be considered representative of the current state of the art. Therefore, another validation case is examined.

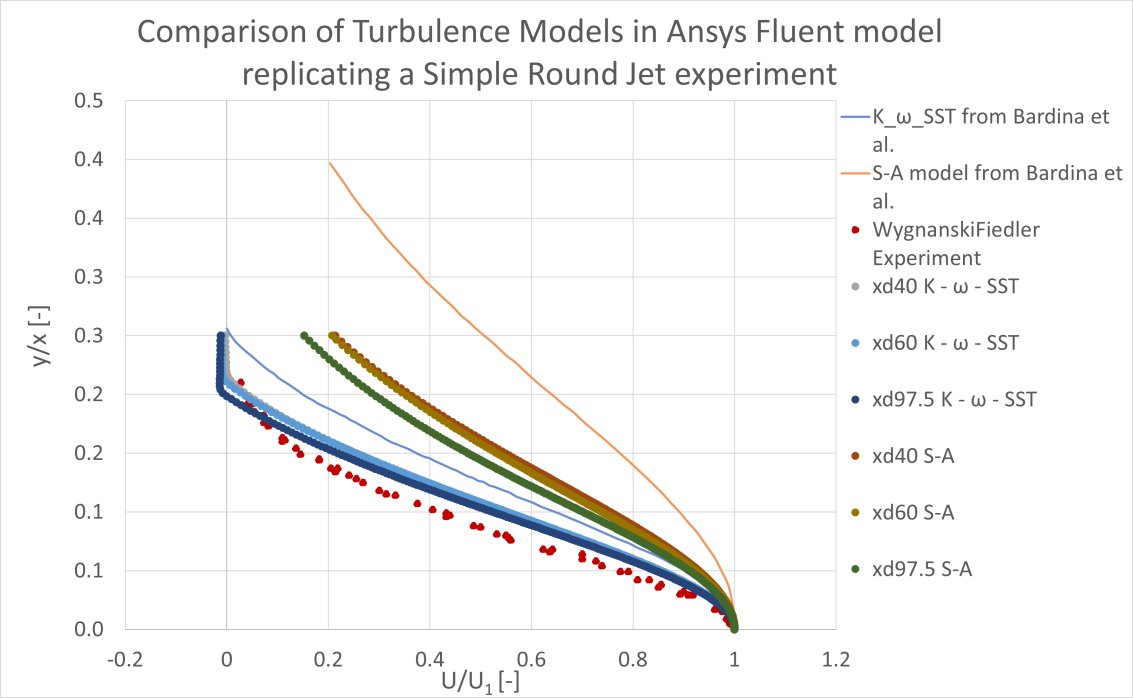

Figure 5.16: Comparison of velocity profiles for different turbulence models, alongside original experimental results [43] and predictions [2]

5.9.2. Simple Free Round Jet Validation (part 2)

The paper by Weaver and Miskovic on RANS turbulence models in fully turbulent jets is used as a validation case [41]. Like the previous case, it describes a simple round turbulent free jet, comparing various turbulence models to an original physical experiment performed by Hardalupas et al. [12]. As this paper was published in 2021, it is a much better representation of the state of the art of CFD simulations and turbulence models.

From the previous validation case, it can be concluded that the $k-\omega-SST$ turbulence model performs significantly better than the Spalart - Allmaras model for turbulent round jets. Therefore, the latter is discarded as a viable model, and instead the $k-\omega-SST$ model is compared to the realizable $k-\epsilon$ model, which is known to produce good results for turbulent free jets, and for which validation data is also available in the chosen case.

In Figure 5.17, the evolution of velocity along the jet center-line as predicted by the model is compared to the simulations by Weaver et al., as well as the original experiment by Hardalupas et al. The largest discrepancy between the current model and experimental results is in the initial region of the jet, where the potential core as predicted by the model extends beyond the experimental case. The same phenomenon occurs to a lesser extent for the reference simulations. A possible explanation for this is the difficulty of capturing the phenomena occurring in a 3D jet with a a 2D axisymmetric model, as the velocity profile given by Figure 5.17 is extracted from the axis boundary of the model.

Further downstream, the model more closely represents the validation data for both turbulence models. The accuracy of the model is still not as high as the state of the art in literature, in the order of 20% error compared to 10% for the literature.
In Figure 5.18, the radial velocity distribution at location $\frac{x}{D} = 20$ can be seen, as predicted by the model, compared to the simulations by Weaver et al. and the original experiment. The distributions given by the model follow those from literature quite closely. Both overestimate the spreading rate of the jet slightly compared to the experimental case, and the $k-\omega-SST$ turbulence model gives slightly better accuracy across the width of the jet than the realizable $k-\epsilon$ model.

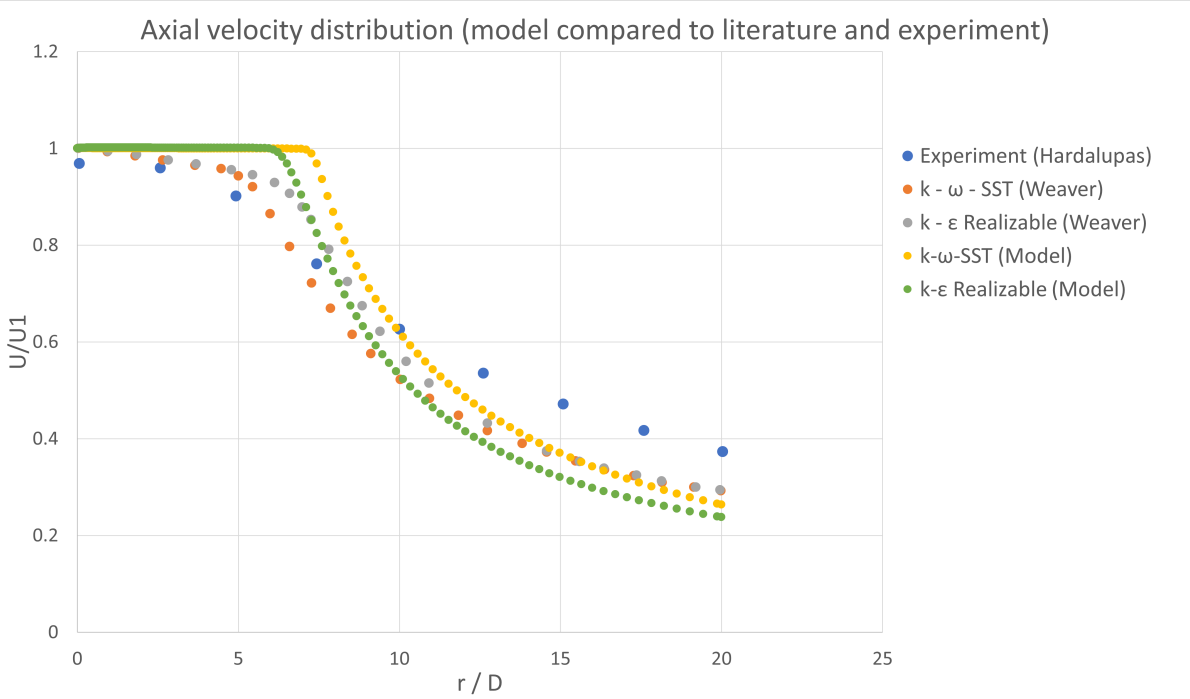

Figure 5.17: Axial velocity profiles compared to experimental results and simulations from literature using the same turbulence models

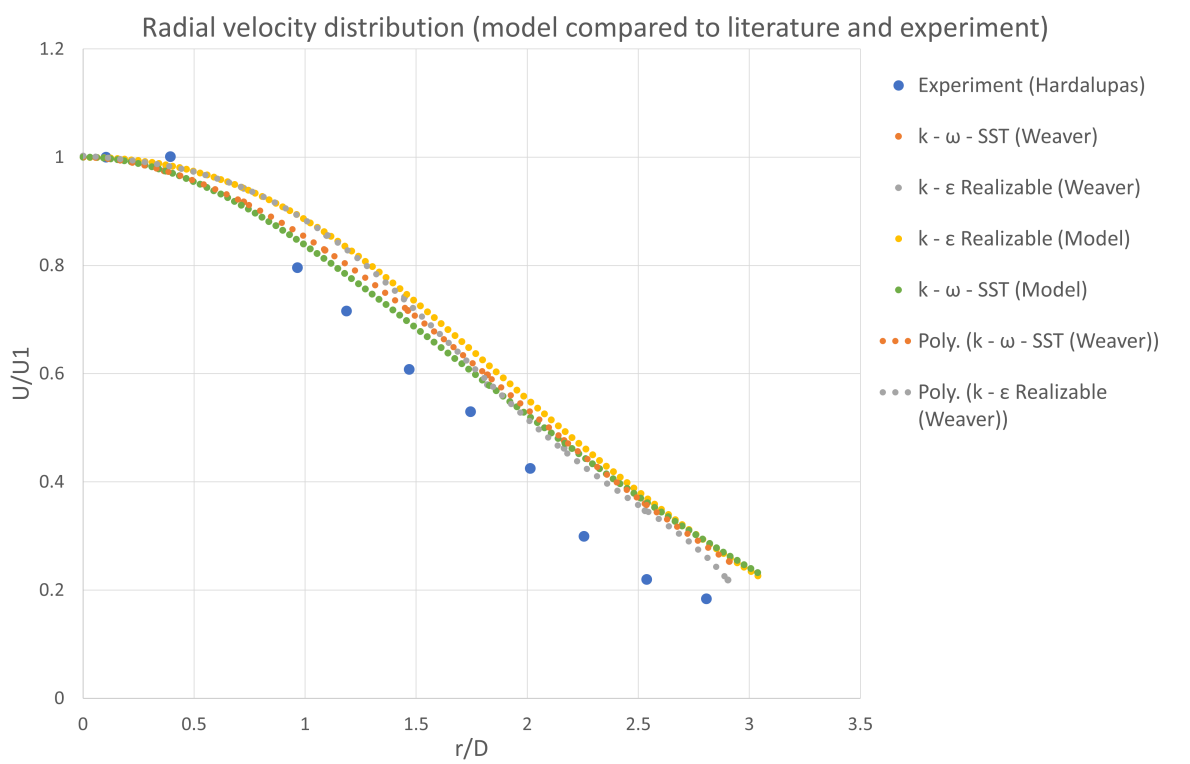

Figure 5.18: Radial velocity profiles compared to experimental results and simulations from literature using the same turbulence models

5.9.3. Co-flow experiment validation

To improve confidence and gain a better understanding of the influence of the turbulence model, another comparison is made between the two models and experimental results for the research done by Ouzani et al. [30]. With a core jet and co-flow jet Mach number of 0.5 and 0.57 respectively, the conditions are a closer representation to the case being considered in the current research.

Model setup

The boundary conditions for the model replicating the co-axial validation case can be seen in section D.3. The model represents an inner heated jet surrounded by a co-flowing annular jet at room temperature, flowing into an ambient stationary environment. The boundary conditions are set up in a manner that as closely as possible matches the approach used in the Flow Field Solver.

Results

The resulting axial velocity distributions predicted by the model along the center of the inner and outer jet can be seen in Figure 5.19 and Figure 5.20 respectively. Similarly to the simple jet case, the potential core length is overestimated by the model, and further downstream the agreement to experimental results improves, with the $k-\omega-SST$ model performing better than the Spalart - Allmaras model. The center-line and outer jet velocity is still underestimated with respect to the experimental values, just as with the simple jet case.

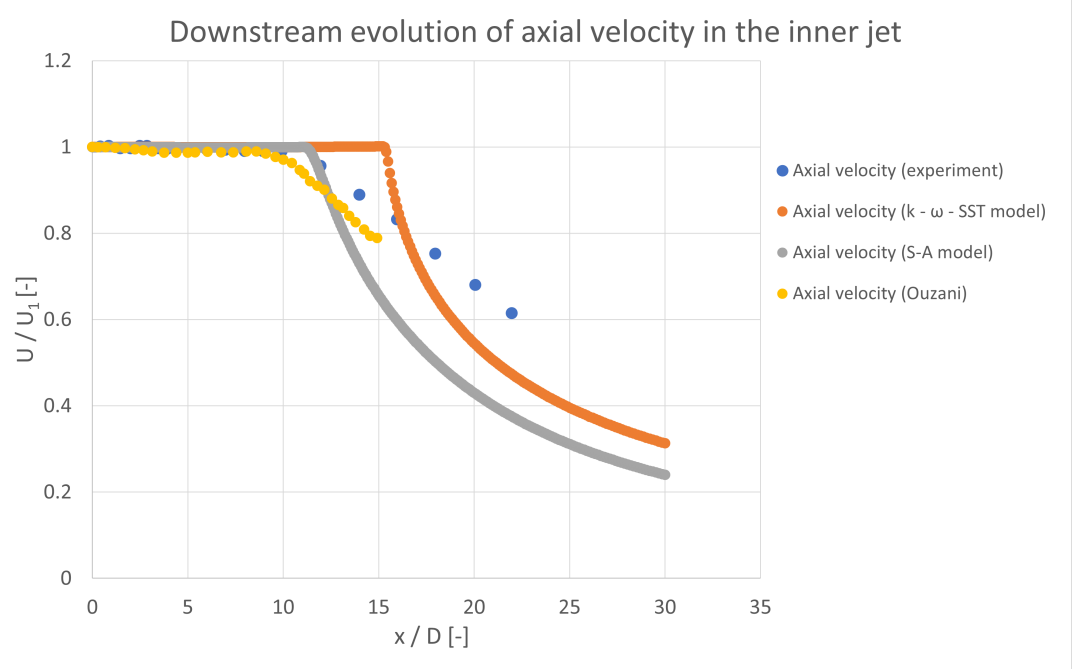

Figure 5.19: Comparison of center-line velocity profiles predicted by both turbulence models to the experimental results and a state-of-the-art simulation from literature [30]

5.9.4. Validation summary

After the validation process for the predictive power of the co-axial mixing model for the velocity field in simple and co-axial jets, the following conclusions can be drawn:

1. The Spalart - Allmaras turbulence model does not give satisfactory results for the modelling of free turbulent jets and is discarded for the current research.
2. The $k-\omega-SST$ and the realizable $k-\epsilon$ turbulence models both yield good agreement with comparable models from literature when it comes to spreading rate and self-similarity for both the simple jets and co-axial jet.
3. In all cases, the length of the potential core is overestimated in the model compared to experimental and simulation results.

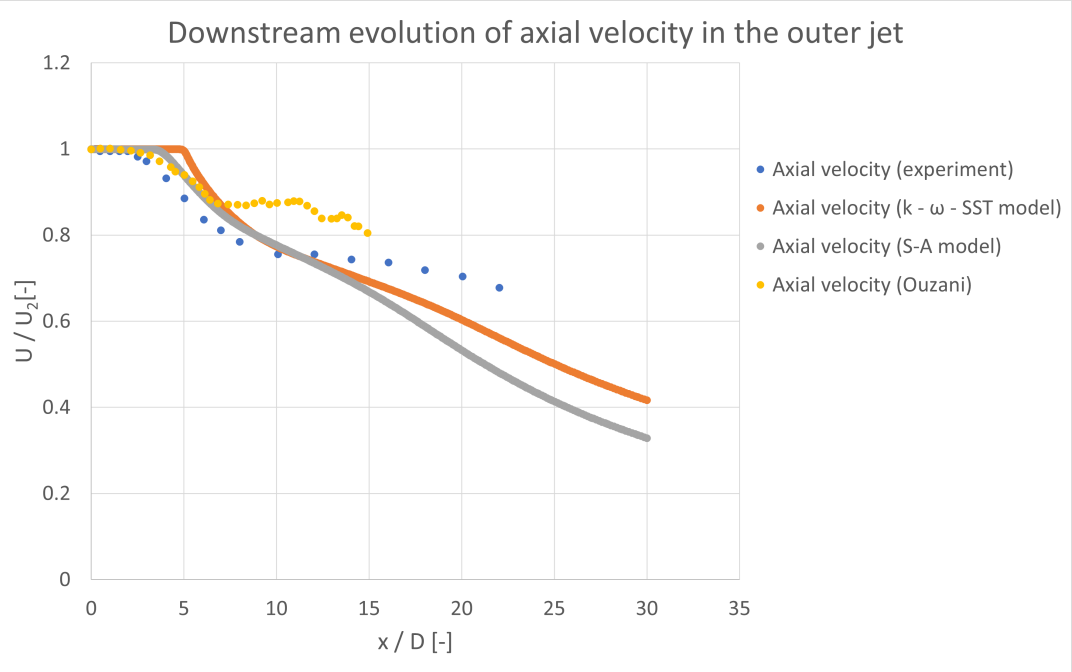

Figure 5.20: Comparison of outer jet velocity profiles predicted by both turbulence models to the experimental results and a state-of-the-art simulation from literature [30]

The main shortcomings of the current model exist within the very near field, and accuracy improves further downstream. As the formation of contrails occurs due to cooling over a larger distance, the co-axial mixing model is determined to be sufficiently accurate to answer the research questions for this thesis. However, improving the accuracy especially in the near-field should be considered in further research.

5.10. Results

The key results from the Co-axial Mixing Model are the temperature and pressure fields in the exhaust of the engine. These fields will be used in chapter 6 to predict the water vapour content and finally the formation of contrails. For a more complete understanding of the flow, the velocity and density fields are also shown. Additional results are also given in Appendix E.

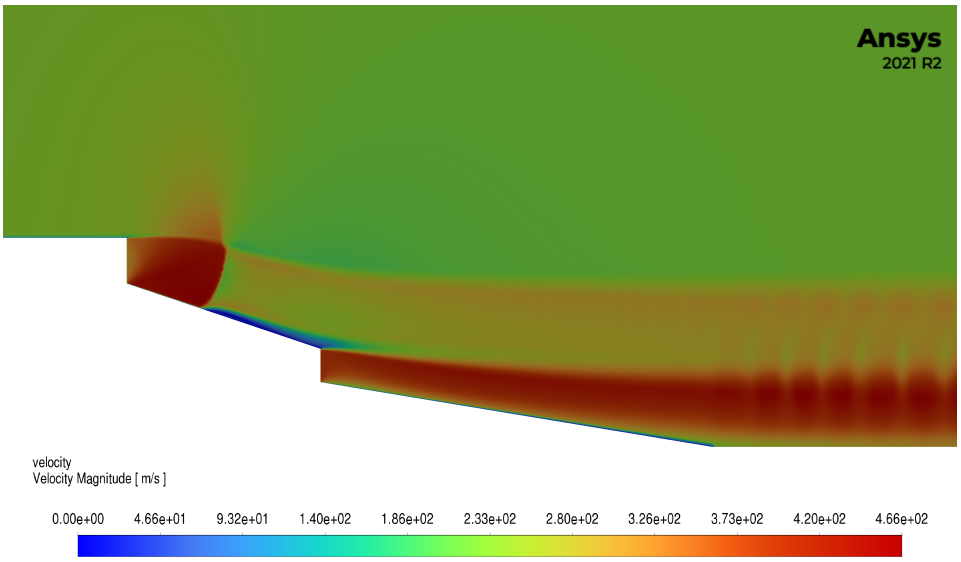

Figure 5.21: Contour plot of the velocity in the very near-field of the Leap-1A engine

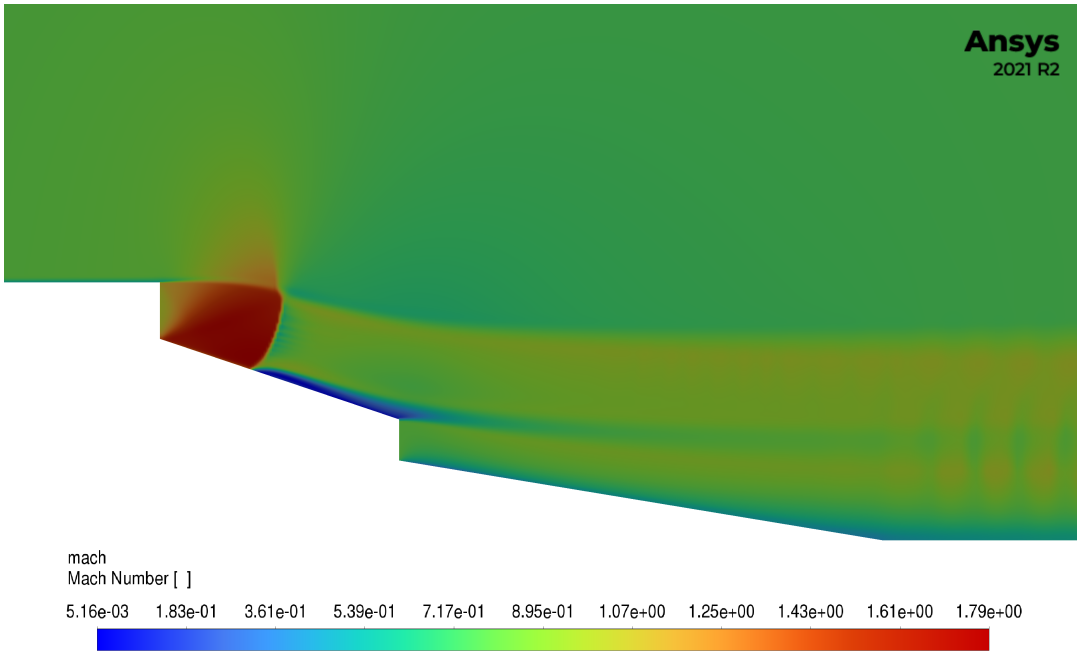

Figure 5.22: Contour plot of the Mach number in the very near-field of the Leap-1A engine

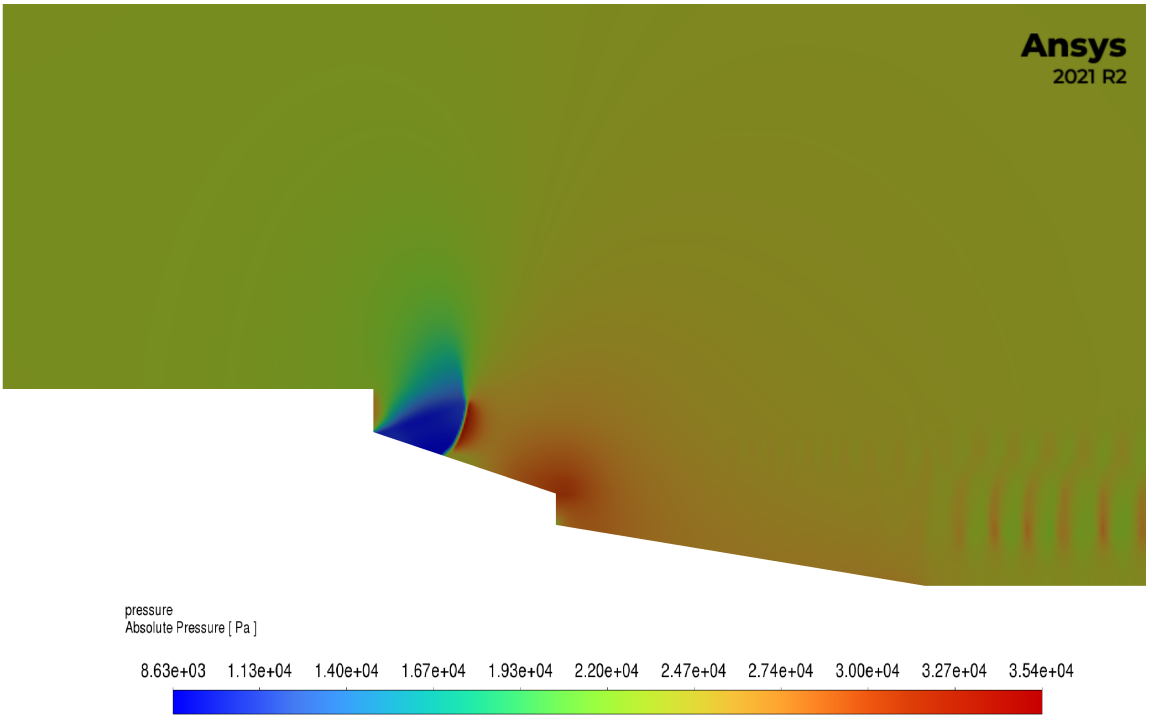

Figure 5.23: Contour plot of the pressure in the very near-field of the Leap-1A engine

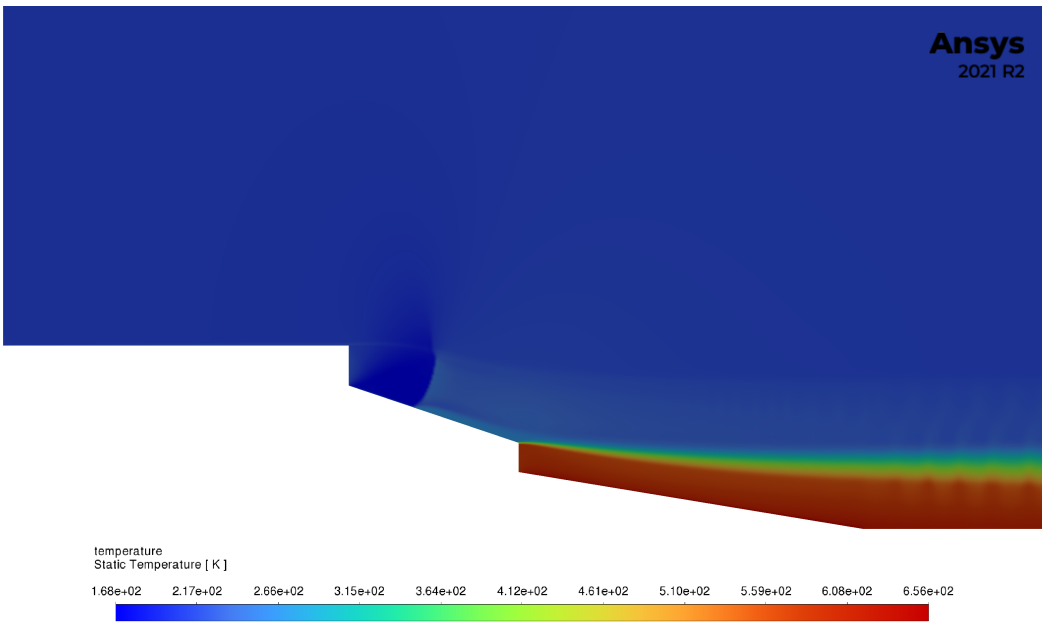

Figure 5.24: Contour plot of the temperature in the very near-field of the Leap-1A engine

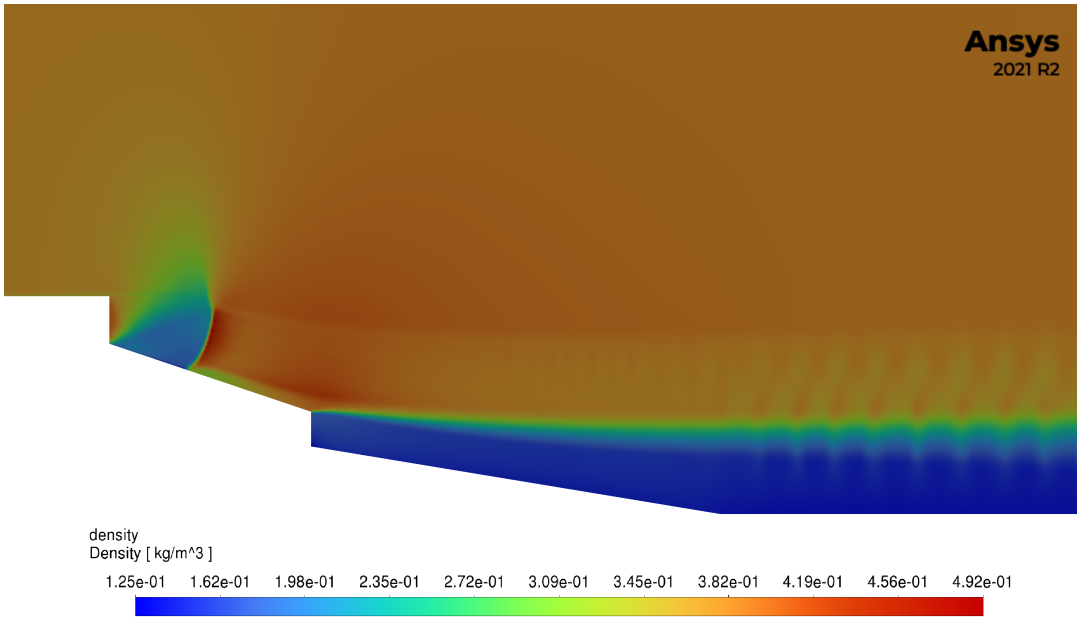

Figure 5.25: Contour plot of the density in the very near-field of the Leap-1A engine

From the velocity contour plot shown in Figure 5.21 the Mach number contour plot in Figure 5.22, the pressure contour plot in Figure 5.23, the temperature contour plot in Figure 5.24, and the density contour plot in Figure 5.25, the following observations can be made:

- The flow entering the domain from the bypass nozzle is under-expanded. This was known from the results of the Engine Performance Model, as the static pressure at the bypass nozzle exit is higher than ambient. It is confirmed by the fact that the Mach number is equal to one at the nozzle exit, and increases upon expanding into the ambient air. As the ambient flow velocity is subsonic ($M_{ambient} = 0.78$), the bypass flow too must be slowed down to subsonic speed. This occurs by the mechanism of a normal shock, which is indeed clearly present in the contour.

- The core jet is fully expanded, as the nozzle pressure is equal to ambient pressure. Therefore there is no further expansion outside the nozzle and no normal shock present.

- In the mixing region between the core and bypass flows, fluctuations in pressure and velocity are found. An initially hypothesized explanation for these fluctuation is the occurrence of Kelvin-Helmholtz instabilities. These occur when two fluid flows with a different velocity and / or density over the shear layer between them interact. This difference in velocity between the two flows introduces small perturbations in the shear layer, which are unstable and roll up into vortices. The flow field in the engine exhaust fulfills the prerequisites for Kelvin-Helmholtz vortices to be formed, as both the velocity and density differ between core and bypass jets. To determine the validity of this hypothesis, as well as the overall sensitivity of the model to input parameters, further investigation is done in section 5.11.

5.11. Sensitivity Analysis

After analyzing the results of the 2D Axisymmetric CFD model for the exhaust of the Leap-1A engine, two aspects lend themselves to further investigation. Firstly, the occurrence of flow expansion and acceleration past Mach 1 out of the bypass nozzle, and secondly, the oscillation of pressure and velocity in the near-field of the exhaust. Both phenomena seem to arise from the bypass flow, and therefore an analysis is performed of the sensitivity of the flow field to the inlet conditions for the bypass nozzle. Specifically, the velocity and pressure are both varied, after which the impact on the velocity and pressure contours in the near-field is examined. The resulting pressure and velocity contours for various bypass nozzle inlet conditions are shown in Appendix B. A summary of the effect of varying pressure and velocity at the bypass nozzle inlet on the appearance of oscillations and shockwaves can be seen in Table 5.12 and Table 5.13 respectively.

$U_{bypass}\ [ms^{-1}]$ \ $p_{bypass}\ [Pa]$	23842	26000	27160
275	No	No	No
300	Yes	Yes	Yes
303	Yes	Yes	Yes
303.9	No	No	Yes

Table 5.12: Occurrence of pressure and velocity oscillations for different combinations of bypass nozzle boundary conditions

$U_{bypass}[ms^{-1}]$ \ $p_{bypass}[Pa]$	23842	26000	27160
275	No	No	No
300	No	No	No
303	No	No	No
303.9	Yes	Yes	Yes

Table 5.13: Occurrence of shockwave for different combinations of bypass nozzle boundary conditions

Looking at these results, a number of observations can be made:

- At the original choked bypass condition $U_{bypass} = 303.9 ms^{-1}$, the model is very sensitive to changes in the bypass velocity condition. If it is lowered to $U_{bypass} = 303 ms^{-1}$, the shockwave disappears.
- To investigate at what bypass velocity the shockwave disappears, an additional simulation was performed at $U_{bypass} = 300 ms^{-1}$. However, the shockwave already disappears at $U_{bypass} = 303 ms^{-1}$, and no significant difference exists between these two conditions.
- The influence of bypass nozzle pressure at $U_{bypass} = 303.9 ms^{-1}$ is twofold. Firstly, the maximum velocity increases with increasing pressure, from $450 ms^{-1}$ to $466 ms^{-1}$. Secondly, the location of the shock is moved slightly downstream.
- The main factor influencing the occurrence of the oscillations in velocity and pressure seems to be the bypass velocity. At the lower velocity of $U_{bypass} = 275 ms^{-1}$, no oscillations occur regardless of the bypass pressure. Conversely, at the higher velocity $U_{bypass} = 300 ms^{-1}$, oscillations are present for all bypass pressures. Only at the original condition of $U_{bypass} = 303.9 ms^{-1}$ is there an influence of the bypass pressure.

From the observations listed above, the following conclusions regarding the shockwave and oscillations can be drawn:

- The disappearance of the shockwave at $U_{bypass} = 303 ms^{-1}$ can be explained by the fact that the velocity is now slightly below the threshold of $M = 1$. It is known that the relation between acceleration of the flow and expansion of area inverts at $M = 1$ (this can be understood from the Area - Velocity relation given in Equation 5.34).

$$\frac{dA}{A} = (M^2 - 1)\frac{dU}{U} \tag{5.34}$$

  Because the flow is given room to expand into when entering the domain from the bypass nozzle, its Mach number will dictate whether it accelerates further or decelerates. In the choked condition, the Mach number is slightly above unity, and therefore acceleration occurs with expanding area. Because ambient flow Mach number $M_{ambient}$ is equal to 0.78, deceleration back to subsonic velocity then occurs through a normal shock. In the case of a lower bypass velocity, expansion results in deceleration and therefore there is no region of supersonic flow. Therefore, there is also no shockwave present.
- The appearance of oscillations for certain combinations of velocity and pressure from the bypass nozzle has a number of plausible causes:

1. Acoustic waves (noise) due to turbulent mixing. It is known from literature that round compressible jets emit a significant amount of pressure fluctuations in the near-field [11]. These can also occur in the form of Mach wave radiation in the case of a supersonic jet [37]. This would explain the highly directional nature of the waves in axial direction, as well as the fact that they disappear at lower velocities and pressures.
2. Transonic resonance. This phenomenon occurs near Mach numbers of unity from pipe jets [42]. Close to the speed of sound, the flow can resonate with the existing geometry in a manner that produces significant noise. This corresponds to the waves occurring for the underexpanded jet.
3. Other effects due to the setup of the CFD model. It is possible that the boundary conditions and geometry of the model generate the oscillations in pressure and velocity. One suggestion to investigate this possibility further would be to model the flow inside the core and bypass nozzles, in stead of treating the nozzle exits as boundaries of the domain.

In conclusion, the shockwave behaves as expected with respect to changes in the boundary conditions. In addition, there are multiple plausible explanations for the oscillating pressure and velocity found in this sensitivity study. It is recommended that these phenomena are investigated further. However, as the phenomena described here correspond to what is known from literature, and they do not have a major influence on the development of the mixing between core and bypass flow, this investigation is considered outside the scope of the current thesis, and is kept as a recommendation for future research.

5.12. Conclusion

In the development of the Flow Field Solver, a large number of iterations were made before arriving at the final 2D axisymmetric model setup. While these approaches were ultimately discarded, they provided lessons that were necessary to arrive at the final model.

- From the 1D mathematical derivation, the understanding emerged that while keeping the underlying assumptions of the Schmidt-Appleman Criterion in place, the same result will be obtained regardless of the mixing ratio between core and bypass flow.
- The 2D plume and entrainment approach extends existing jet entrainment and plume models from a simple 1D analysis to a 2D model. This allows for a more complete analysis of the mixing between the core and bypass flow compared to the 1D approach. It also has its shortcomings. Most notably, the flow properties are assumed constant across the core and bypass jets respectively, flow is assumed to be incompressible, and ambient velocity is assumed to be zero. This results in a model that is internally consistent but requires assumptions that are too far removed from the real phenomena occurring in the exhaust.
- The next step in complexity is the discretization of the flow field in radial direction to create a truly 2D domain. For this purpose, a Python module for the implementation of PDE's through the Finite Element method was employed. While this addresses the shortcoming of the previous iteration with respect to constant flow properties in radial direction, the phenomenon of turbulent mixing still cannot be reliably accounted for in this approach. As the exhaust behind a turbofan engine is highly turbulent, this ultimately means this approach is not sufficient to answer the research questions with confidence.
- From the previous model approaches, the conclusion is drawn that turbulence needs to be modelled for an accurate representation of reality to be made. To achieve this, a 3D CFD model was set up. Over the course of many iterations, the conclusion was reached that the full 3D approach, while theoretically providing the best agreement with reality, requires more time and resources than are available for the current research.

The final approach that has proved successful is the 2D axisymmetric model developed in Ansys Fluent. This model has been verified through a Grid Convergence Study and validated by comparison to multiple experiments and similar models from state-of-the-art literature. The conclusions from this modelling process can be summarized as follows:

- The Grid Convergence Study showed that the numerical error can be considered negligible after a refinement by factor 1.5 with respect to the original grid.

- From the validation process, it can be concluded that the current model setup results in good agreement with literature in terms of predicted spreading rate for simple round jets. In addition, the development of self-similarity is observed in accordance with expectations from theory. The potential core length is overestimated in both simple and co-axial jets. This also occurs in simulations in literature, but to a lesser extent. It is hypothesized that a fully 3D approach would improve this aspect of the model. This falls outside the scope of the current research, but is suggested as a possible avenue for further investigation.
- The mixing of core and bypass jets in the exhaust of the Leap-1A engine results in a fluctuating flow field in terms of velocity, pressure, density, and temperature. It is hypothesized that this represents noise due to turbulent mixing, or transonic resonance with the engine geometry. It is suggested that this phenomena be investigated in future research.

In the following chapter, the flow field generated by the Flow Field Solver will be used to predict the formation of contrails in the engine exhaust.

6

Contrail Formation Prediction Model

6.1. Introduction

The final module in the chain is the Contrail Formation Prediction Model. Now that the 2D axisymmetric CFD approach has been validated for modelling the flow parameters in the exhaust, it can be applied to determine the spreading of water vapour throughout the domain. Consequently, using the knowledge of the contrail formation process described in section 2.3, criteria for contrail formation are set out and applied to the resulting water vapour and temperature fields from this model. As a result, contours can be drawn of regions in which the criteria for contrail formation are met in the exhaust. Finally, as the goal of this research is to examine the accuracy of the Schmidt-Appleman Criterion, mixing lines are drawn from the results of the model and compared to the original mixing line predicted by the SAC. This allows the drawing of conclusions with respect to the research questions set out in section 2.6.

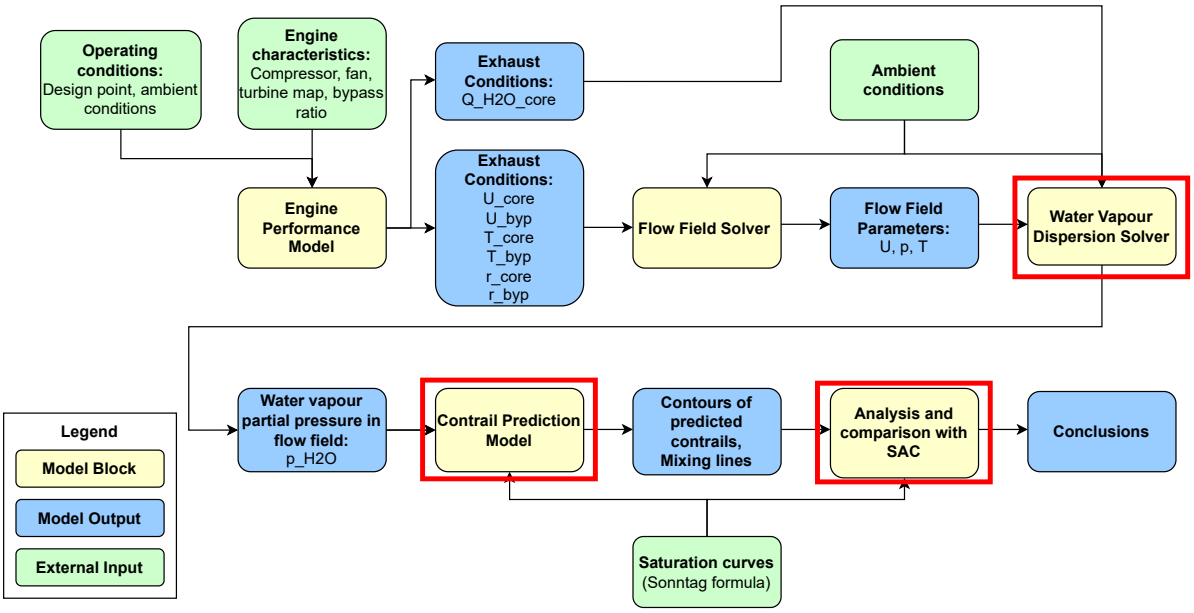

Figure 6.1: Current modelling step in the overall framework

6.2. Additional Literature

For the completion of the Contrail Formation Model, additional definitions specific to this step are taken from literature and briefly discussed here. First, the concept of homogeneous freezing is explained, after which the Emission Index of a species is defined. Finally, the definition and mathematical expression for Dilution Ratio are treated, which can later be used for validation purposes.

6.2.1. Nucleation of crystals (homogeneous freezing)

In a region of the atmosphere where there is more than 100% relative humidity with respect to ice, one could expect ice to already be present. However, without nuclei to form around, ice crystals do not spontaneously form at freezing temperatures. This principle explains the existence of "supercooled water", where temperatures can be brought below $0\,^{\circ}C$ with the water remaining in liquid or gaseous form. In fact, in many regions of the atmosphere, saturation with respect to ice can reach levels of 140% to 170% without ice being formed. This supersaturation can be maintained all the way down to the temperature threshold for homogeneous nucleation, which is known to be at $-38^{\circ}C$. Below this temperature, the balance of the reaction equation for homogeneous nucleation is such that it occurs spontaneously. [19]

6.2.2. Engine Emission Indices

The additional boundary conditions for the Contrail Formation Model are the species concentrations for water vapour, air, and carbon dioxide. In reality, the exhaust of a turbofan engine contains several other species, as can be seen in Figure 6.2. Here, the mean Emission Indices for species in the exhaust of aircraft are shown. The Emission Index is defined as the mass of an emitted species per unit mass of fuel. In the case of Figure 6.2, this is given in gkg^{-1}.:

$$EI = \frac{m_{species}}{m_{fuel}} \tag{6.1}$$

Species	Emission index, g kg^{-1} (ranges)
Kerosene	
CO_2	3160
H_2O	1240
NO_x	14 (12–17)
Soot	0.025 (0.01–0.05)
SO_2	0.8 (0.6–1.0)
CO	3 (2–3)
HC	0.4 (0.1–0.6)

Figure 6.2: Mean Emission Indices (EI) for emitted species for the fleet of aircraft in 2000, using kerosene jet fuel [21]

6.2.3. Dilution Ratio

The dilution ratio N is defined in accordance with the description given by Schumann et al.: "The dilution ratio N [...] measures the amount of air mass with which the exhaust resulting from a unit mass of burned fuel mixes per unit flight distance within the bulk of the plume" [35]. This ratio can be mathematically expressed as follows:

$$N = \frac{AFR}{Z} \tag{6.2}$$

where AFR is the Air to Fuel Ratio of the engine and Z the mixing ratio between gas from the exhaust and ambient air. This ratio Z in turn can be calculated by comparing the concentration of an inert species at a given location Z_l to the initial concentration in the core jet $Z_{i,jet}$ and the ambient air $Z_{i,amb}$:

$$Z = \frac{Z_l - Z_{i,amb}}{Z_{i,jet} - Z_{i,amb}} \tag{6.3}$$

This results in $Z = 1$ at the core nozzle and $Z = 0$ at ambient conditions. It is common practice to relate this dilution ratio not to the distance behind the engine, but the plume age t, as this is allows for a more universal comparison between different jets. This requires the axial distance x in the model to be translated to a measure of time, which is done by the following relation:

$$t = \frac{x}{U_{cl}} \tag{6.4}$$

where U_{cl} is the center-line velocity of the exhaust plume.

6.3. Prediction of Water Vapour Content

To predict the concentration of water vapour at a given location in the exhaust, two options are considered. The most complete approach would be to include species mixing and multi-phase analysis in the CFD model. However, initial efforts in this direction indicate that this approach may introduce additional complexity and require more computational resources. Therefore, a simplified approach is first employed: Predicting the water vapour concentration by deriving it from the temperature gradient within the flow.

6.3.1. Temperature gradient based mixing

In this section, the underlying assumptions are first laid out. Consequently, the mathematical derivation for the water vapour content as function of temperature gradient is described. Finally, a conclusion is drawn regarding the feasibility of this approach for the current research.

Assumptions

The temperature gradient based approach rests on the following assumptions:

1. The mass fraction of water vapour is low, such that its effect on the overall momentum and mass transfer within the flow is negligible

2. The temperature gradient is an accurate predictor for the mixing of the core, bypass, and ambient flow. This is a reasonable assumption because the mixing model does not include any chemical processes or radiation terms. Therefore, any temperature gradient in the flow field should be directly analogous to the mixing gradient of flows with different temperatures.

3. The Schmidt number of the mixture of air and water vapour is unity within the flow. The Schmidt number is defined as:

$$Sc = \frac{\nu}{D} = \frac{\text{Kinematic viscosity}}{\text{Molecular diffusivity}} \tag{6.5}$$

   Taking a closer look at the kinematic viscosity term, it can be defined as relating the viscous stresses within a fluid to the rate of deformation of this fluid. Stress, in turn, is defined as force per unit area, while rate of deformation is a velocity term and therefore linked to the momentum of the flow. Therefore, kinematic viscosity can be interpreted as the ability of a fluid to transport momentum by molecular means.

   This means the relation represented by the Schmidt number can be restated as follows:

$$Sc = \frac{\text{molecular momentum transport}}{\text{molecular species transport}} \tag{6.6}$$

   In a gas, both of these phenomena occur by the same mechanism, namely the movement of the molecules relative to each other. Therefore, the Schmidt number is indeed close to unity. This is also confirmed by experiments in the case of a mixture of air and water vapour.

If the above assumptions are all deemed plausible, it can then be concluded that the mixing of water vapour follows the same gradient as the temperature within the exhaust. The remaining parameters that need to be known are then the concentration of water vapour in both the core exhaust and then ambient air. The first is given by the results of the engine performance model. The second depends on ambient conditions, and can

be assumed based on the case that needs to be examined.

Mathematical Derivation
To derive the water vapour concentration field from the temperature field, a linear relation between the two is postulated of the following form:

$$q_{H_2O} = \frac{dq_{H_2O}}{dT} T + q_{H_2O_0} \tag{6.7}$$

The gradient term $\frac{dq_{H_2O}}{dT}$ is derived from the linear slope between the two points where both water vapour concentration and temperature are known quantities:

$$\frac{dq_{H_2O}}{dT} = \frac{q_{H_2O_{core}} - q_{H_2O_{ambient}}}{T_{core} - T_{ambient}} \tag{6.8}$$

Consequently, the theoretical value $q_{H_2O_0}$ for a temperature of $T = 0K$ can be obtained by rewriting Equation 6.7 for $q_{H_2O_0}$ and substituting the known values $q_{H_2O_{core}}$ and T_{core}:

$$q_{H_2O_0} = q_{H_2O_{core}} - \frac{dq_{H_2O}}{dT} T_{core} \tag{6.9}$$

Feasibility
The feasibility of the temperature-gradient based approach depends on the validity of the underlying assumptions. To assess this, the predictive power of this approach has been compared to validation experiments from literature. For these cases, the assumptions can be considered validated. However, the main difference between the conditions in the validation cases and the conditions encountered in the current research, is that the former are subsonic and therefore incompressible, while the engine exhaust is in the transonic domain and compressible flow is therefore encountered. In the case of compressible flow, temperature gradients are no longer solely due to mixing of flows. This can most clearly be seen in the results from chapter 5, where the shockwave in the bypass flow exhibits strong temperature gradients. The second assumption is therefore no longer valid in the compressible case, and this approach is discarded as an option for the current research. Because this approach is not used in the final version of the model, the validation efforts are shown in Appendix C.

6.3.2. Species Transport in Ansys Fluent

The second approach is to directly model the transport of species in the Ansys Fluent software. The current model treats the species as inert, so no reactions occur, and the Emission Index of the remaining species is orders of magnitude lower than that of CO_2 and H_2O. Therefore, their impact can be considered negligible in the current model, and only air, water, and carbon dioxide concentrations are taken into account. A preset mixture of species corresponding to air in our atmosphere is provided by Fluent and used in this case.

The boundary conditions are imposed in the form of mass fractions q_{H_2O} and q_{CO_2}, which can easily be derived by dividing the species mass flows by the total core mass flow $\dot{m}_{core}$:

$$q_{species} = \frac{\dot{m}_{species}}{\dot{m}_{core}} \tag{6.10}$$

The mass fraction of air q_{air} is then automatically determined by Ansys as the remainder of the mixture:

$$q_{air} = 1 - q_{H_2O} - q_{CO_2} \tag{6.11}$$

6.4. Water Vapour Partial Pressure

The formation of contrails occurs if the relative humidity with respect to ice is above 100%. Relative humidity is defined by the following fraction:

$$rh = \frac{p_{H_2O}}{e_s} \tag{6.12}$$

where p_{H_2O} is the water vapour partial pressure and e_s the saturation pressure. As the calculation of water vapour content thus far has resulted in the mass fraction of water vapour, this needs to be translated to the

water vapour partial pressure.

The partial pressure of a gas is defined as the pressure this gas would have if it alone occupied the same volume as the complete mixture if the temperature is kept constant. According to Dalton's Law, the total pressure of a mixture is equal to the sum of the partial pressures of the constituent gases in the mixture, assuming ideal gases. [6] For a theoretical mixture of gases 1,2,3:

$$p = p_1 + p_2 + p_3 \tag{6.13}$$

Again assuming ideal gases, the partial pressure of one gas is dependent on its fraction of molecules in the mixture:

$$p_1 = x_1 \cdot p \tag{6.14}$$

where x_1 is the molar fraction of gas 1 in the mixture. The final ingredient needed then, to derive the partial pressure from the mass fraction, is the relationship between mass fraction q and molar fraction x. This calculation is done internally by the Fluent solver. The water vapour partial pressure can then be found by the relation below:

$$p_{H_2O} = x_{H_2O} \cdot p \tag{6.15}$$

6.5. Boundary Conditions

The boundary conditions for the core inlet are based on the results from the Engine Performance Model combined with the EI values given in Figure 6.2. The fuel mass flow $\dot{m}_{fuel}$ can be multiplied by the respective Emissions Indices to arrive at the corresponding mass flows $\dot{m}_{H_2O}$ and $\dot{m}_{CO_2}$ from the core nozzle.

In the ambient air and bypass flow, no additional CO_2 is present beyond what is already taken into account by the air mixture. Therefore, only the water vapour content needs to be determined here. In this research, two ambient conditions are examined: One in which no ambient water vapour is present, in which case the mass fraction q_{H_2O} is zero. The second case is an Ice Supersaturated Region (ISSR). The ambient humidity is chosen such that it lies halfway between the ice and water saturation curves at the ambient temperature. This point is chosen such that there is enough water vapour content for persistent contrails to be formed, without liquid water already being present in the air. The water vapour content is first calculated as a partial pressure value p_{H_2O}. This is then translated back to a mass fraction by inverting the process described in section 6.4.

6.6. Criteria for Contrail Formation

The criteria for the formation of contrails in a given region of the engine exhaust are defined as follows:

- Water vapour partial pressure is above saturation pressure with respect to water (relative humidity is above 100%).
- The temperature is below the threshold for homogeneous freezing ($T < 235K$).
- A sufficient number of soot particles are present to act as nuclei.
- For persistent contrails: The ambient air is supersaturated with water vapour with respect to ice (the aircraft is flying through an Ice Supersaturated Region (ISSR)). At the same time, ambient air should be below saturation with respect to water, or cirrus clouds would already be present in the atmosphere.

6.6.1. Saturation with respect to liquid

As explained in section 2.4, relative humidity is defined as the water vapour partial pressure relative to the saturation vapour pressure. This relation was given originally in Equation 2.1. The water vapour partial pressure is derived using the approach described in section 6.3. The saturation pressure depends solely on temperature, and is given by the Sonntag formula [36].

6.6.2. Temperature Threshold

As explained in section 6.2, the dominant mechanism by which ice crystals form within the water droplets that have condensed around soot particles is homogeneous freezing. This also explains why contrails do not just form within the engine exhaust on a winter day on the runway for example, when temperatures are below 0 °. While these temperatures are enough for water to freeze heterogeneously, i.e. when attached to a solid surface, homogeneous freezing has a much lower temperature threshold. This threshold is typically agreed in literature to be at $-38°C$, or $235K$. [19].

6.6.3. Additional criteria for contrail persistence

Whether a contrail formed by the exhaust of an engine persists in the atmosphere for minutes, hours or days depends on atmospheric conditions. If the water vapour partial pressure is above saturation with respect to ice, but below saturation with respect to water, the ambient conditions are said to be an Ice Supersaturated Region (ISSR). The same approach as in subsection 6.6.1 is used for saturation of water vapour with respect to ice. It is not immediately relevant for the formation of contrails, as this depends on saturation with respect to water. However, it is relevant for predicting the persistence of these contrails, as below saturation with respect to ice the balance of the evaporation - condensation reaction will be such that water evaporates back into the air until the ice crystals disappear again.

6.7. Validation

The validation of the Contrail Formation Model is done in two steps. Firstly, the model's capacity to predict dilution ratio is compared to that of state-of-the-art models from literature as well as empirical formulas. Secondly, the formation of contrails as predicted by the model is compared to predictions from literature for a validation case.

6.7.1. Dilution Ratio Validation

To validate the capabilities of the model to accurately predict the transport of species in the exhaust, an analysis is done on the dilution ratio N predicted by the model compared to results from literature. As a validation case, the paper on "Modeling capabilities on the formation of contrails in a commercial CFD code" by Cantin et al. is used. [4] In this research, the formation of contrails from the Leap-1A is also examined, making it very suitable for comparison. The same approach to validation is employed in this paper, comparing its predicted dilution ratio to calculated values taken from in situ experiments by Schumann et al. [34]. This allows the results from the current model to be compared to both a state of the art simulation and real data simultaneously.

Boundary Conditions

For a valid comparison, the conditions from the reference case should be replicated as closely as possible. Therefore, instead of using the data from the GSP model as inputs for the simulation, the conditions stated in the paper by Cantin et al. are used. [4]. They are summarized in Table 6.1

Parameter	Unit	Core inlet	Bypass inlet	Ambient
Mach number	[−]	1	1	0.85
Total pressure	$[Pa]$	39310	50000	38171
Total temperature	$[K]$	637	278	250.428
Water vapour molar fraction	[−]	$2.2E-02$	$6.08E-05$	$6.08E-05$

Table 6.1: Boundary conditions for the plume dilution validation case

Results

In Figure 6.3, the dilution ratio as a function of plume age can be seen, as predicted by the Contrail Formation Model, in comparison with the validation case and experimental measurements, as well as an empirical formula derived by Schumann et al for the dilution of plumes. [35] This formula can be stated as follows:

$$N = 7000 \frac{t}{t_0}^{0.8} \tag{6.16}$$

where reference scale t_0 is typically taken as $1s$. It is noted by the authors of this formula that individual cases can deviate from this approximation by factors of 3 to 5.

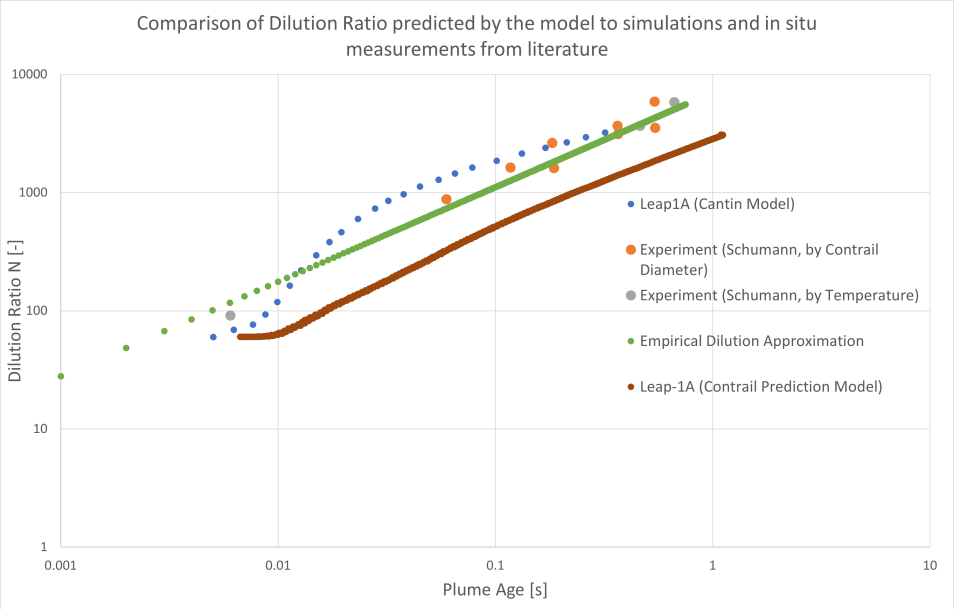

Figure 6.3: Comparison of dilution ratio predicted by the model to the prediction by Cantin et al. [4] as well as experimental in-situ measurements by Schumann et al. [34] and an empirical approximation [35].

When comparing the results from the model to the simulation by Cantin et al., two main differences can be seen: Firstly, the dilution ratio for all plume ages is estimated to be lower than the reference simulation. Secondly, the slope of the current model is much more constant than that of the reference simulation.

The contrail formation model shows good agreement with the empirical formula given in Equation 6.16 in terms of slope for the majority of the evolution of the plume. The only exception is in the very early moments. This corresponds to earlier observations in the validation of the Co-axial Jet Mixing Model, where the extended potential core when compared to literature suggests mixing is not entirely accurately predicted in the very near-field of the exhaust, but accuracy improves beyond this region.
In terms of magnitude, the dilution ratio is predicted to be lower than the empirical formula. However, this falls within the expected range of a factor 3-5 as suggested by Schumann et al. [35].

In conclusion, the dilution ratio as a function of plume age is within the expected range when compared to literature. The good agreement of the slope with empirical formulas indicates that for the spreading of water vapour from a modern turbofan engine exhaust, this model can be considered valid.

6.7.2. Contrail formation prediction validation

Now that species transport has been validated, the end result of contrail formation prediction based on the criteria set out in section 6.6 can be put to the test. To validate the model in this capacity, the same reference case by Cantin et al. is used. [4]. This simulation results in the prediction of saturation ratio and ice particles in the exhaust of the Leap-1A engine shown in Figure 6.4. As indicated in this contour, the formation of contrails starts to occur in the outer mixing zone of the jet, at 15.5 m from the core nozzle.
For the same conditions, the Contrail Formation Model predicts a water vapour saturation contour as shown in Figure 6.5. On this contour, the criteria for contrail formation can be imposed to find the regions where contrails are predicted to form. Specifically, the saturation with respect to water needs to be above unity, and the temperature should be below the threshold of $-38°C$. Implementing these thresholds as lines in the existing contour results in the white boundaries shown in the figure.
From this figure, the location at which contrails are first formed can be seen. The first regions where both water saturation and temperature threshold conditions are met, occur in the outer mixing region, at 15.77 m from the core exhaust. This corresponds almost exactly to the prediction by Cantin et al. From this comparison, it can be concluded that the ability of the model to predict contrail formation for a modern turbofan engine corresponds to that of state-of-the-art simulations for the examined case. Therefore, the Contrail Formation Model is considered to be validated.

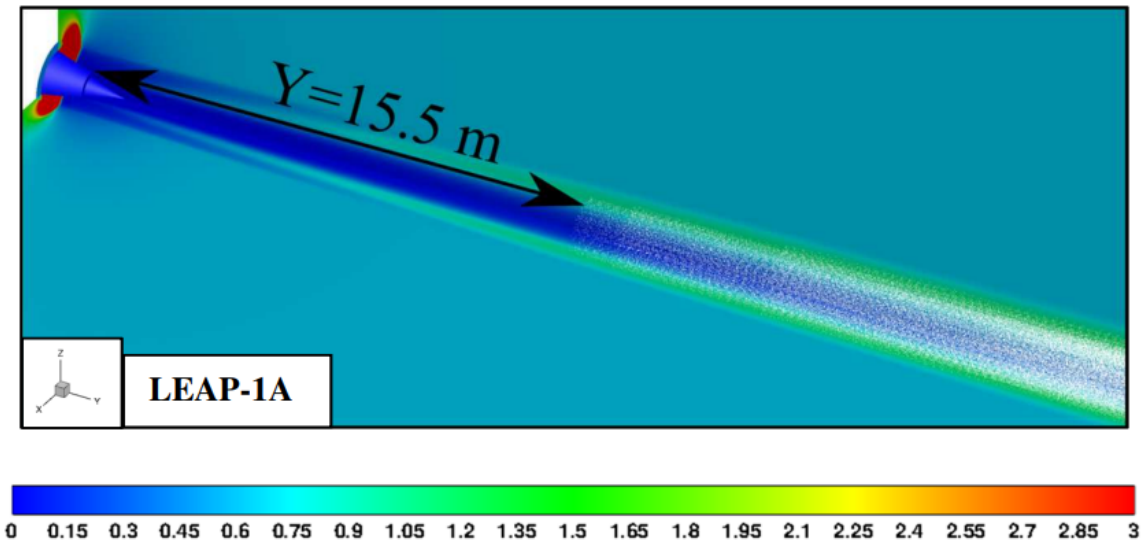

Figure 6.4: Contour plot of the water saturation in the exhaust of the Leap-1A engine at cruise as predicted by Cantin et al. [4]

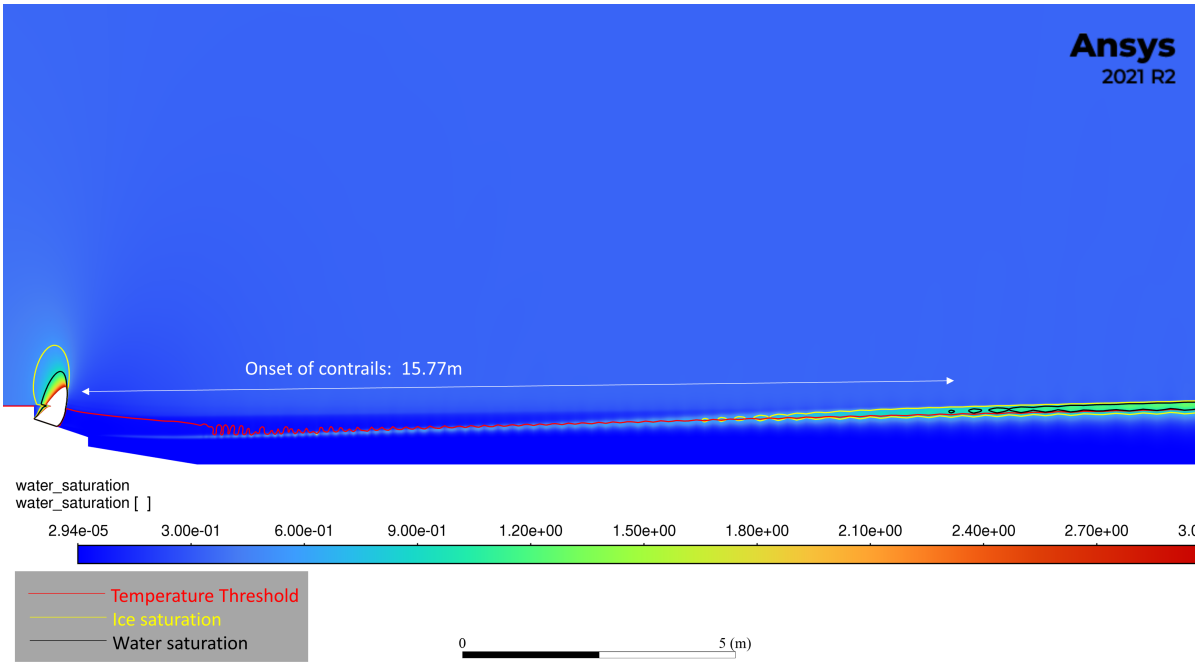

Figure 6.5: Contour of the water vapour saturation in the very near-field of the Leap-1A engine for conditions matching the reference case, as predicted by the Contrail Formation Model, with imposed criteria for contrail formation, and the distance at which onset of contrails occurs annotated

6.8. Results

With the Contrail Formation Model now completed and validated, it can be applied to the Leap-1A engine case study. This is done by first defining the boundary conditions, subsequently generating contours of water vapour saturation and determining contrail formation locations, and finally comparing the resulting mixing lines to those predicted by the SAC.

6.8.1. Case definition and Boundary Conditions

For the prediction of contrail formation from the Leap-1A engine at cruise conditions, the model is using the same settings as the Co-axial Jet Mixing Model described in chapter 5, but now including the species transport equations for water vapour, carbon dioxide and air. These additional boundary conditions are calculated by the process described in section 6.5. These parameters and their prerequisites are summarized for dry ambient conditions and ISSR conditions in Table 6.2

Species	$EI[gkg^{-1}]$	$\dot{m}_{core}[kgs^{-1}]$	$q_{core}[-]$	$q_{ambient_{dry}}[-]$	$q_{ambient_{ISSR}}[-]$
H_2O	1240	0.753	0.0552	0	$8.027E-05$
CO_2	3160	1.920	0.1406	0	0

Table 6.2: Species concentration boundary conditions for the Leap-1A Contrail Formation Model in dry ambient conditions and ISSR conditions

6.8.2. Water Saturation Contours and Contrail Locations

Using the boundary conditions specified in Table 6.2, the contour plots for water vapour saturation are generated for the Leap-1A case study, for both dry ambient conditions and an ISSR. The results for both cases, both close to the engine and further away, can be seen in Figure 6.6 to Figure 6.11.

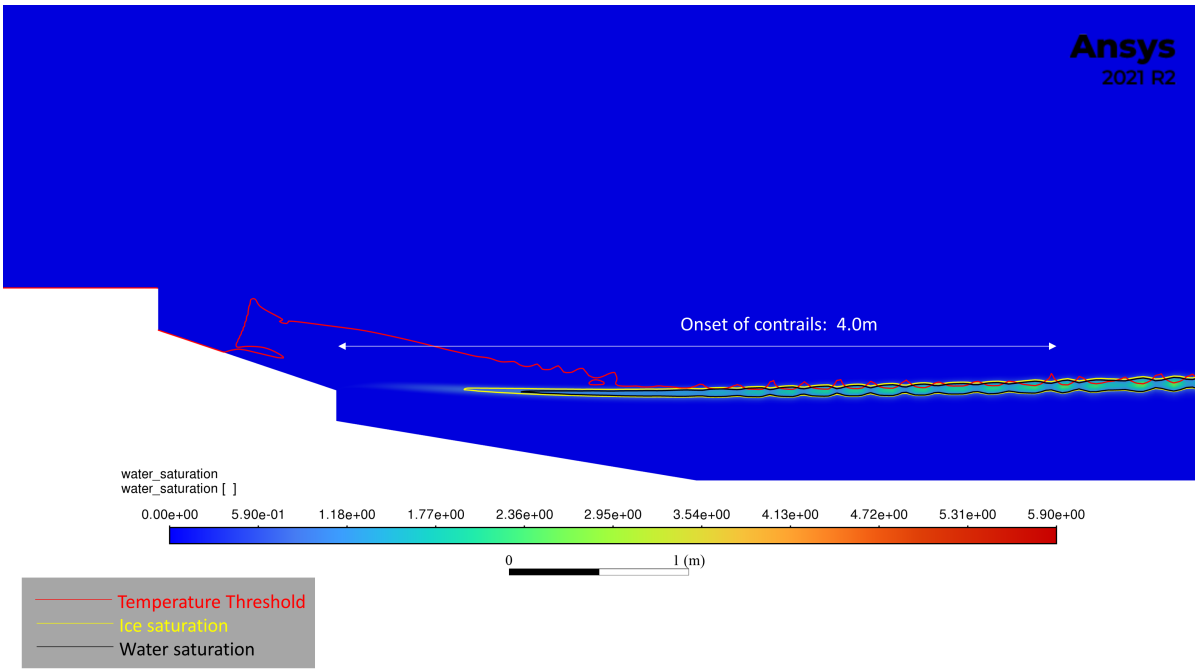

Figure 6.6: Contour of the water vapour saturation in the very near-field of the Leap-1A engine for ambient humidity of 0%, as predicted by the Contrail Formation Model, with imposed criteria for contrail formation, and the distance to onset of contrails annotated

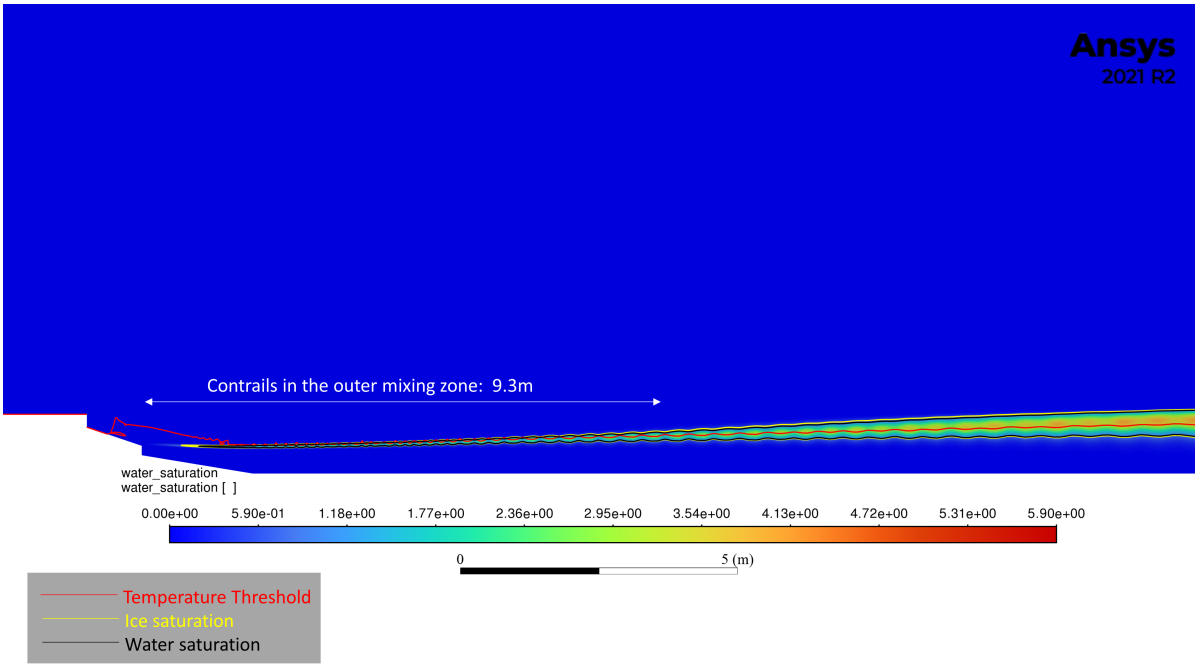

Figure 6.7: Contour of the water vapour saturation in the near-field of the Leap-1A engine for ambient humidity of 0%, as predicted by the Contrail Formation Model, with imposed criteria for contrail formation, and the distance to the appearance of contrails in the outer mixing zone annotated

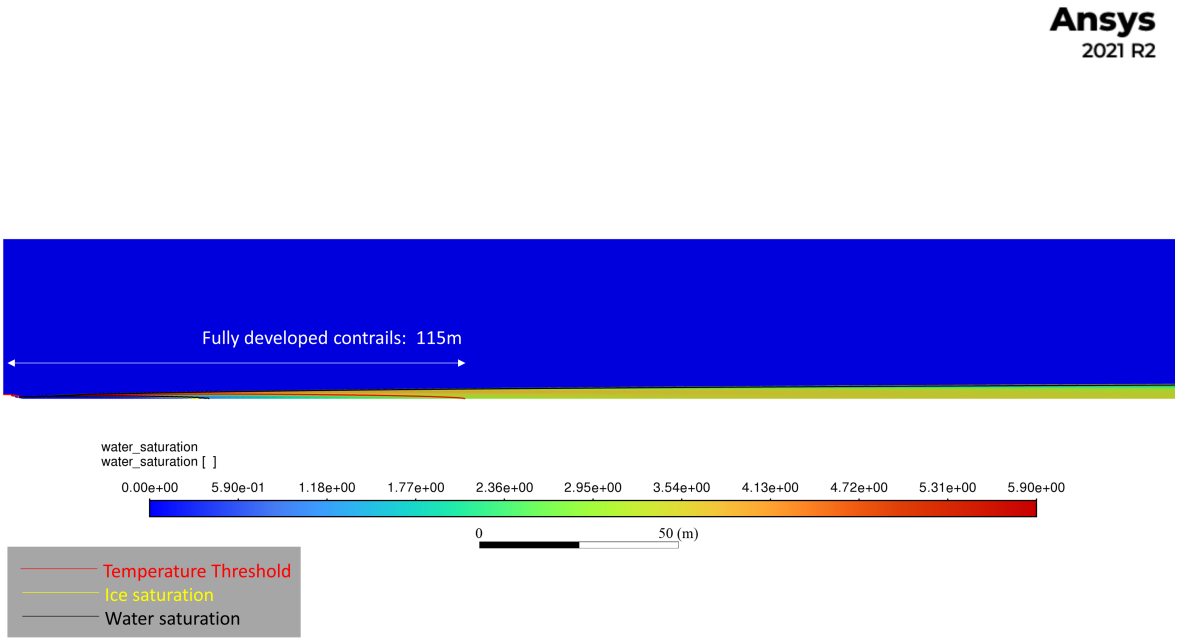

Figure 6.8: Zoomed-out contour of the water vapour saturation in the exhaust of the Leap-1A engine for ambient humidity of 0%, as predicted by the Contrail Formation Model, with imposed criteria for contrail formation, and the distance to fully developed contrails as well as their end annotated

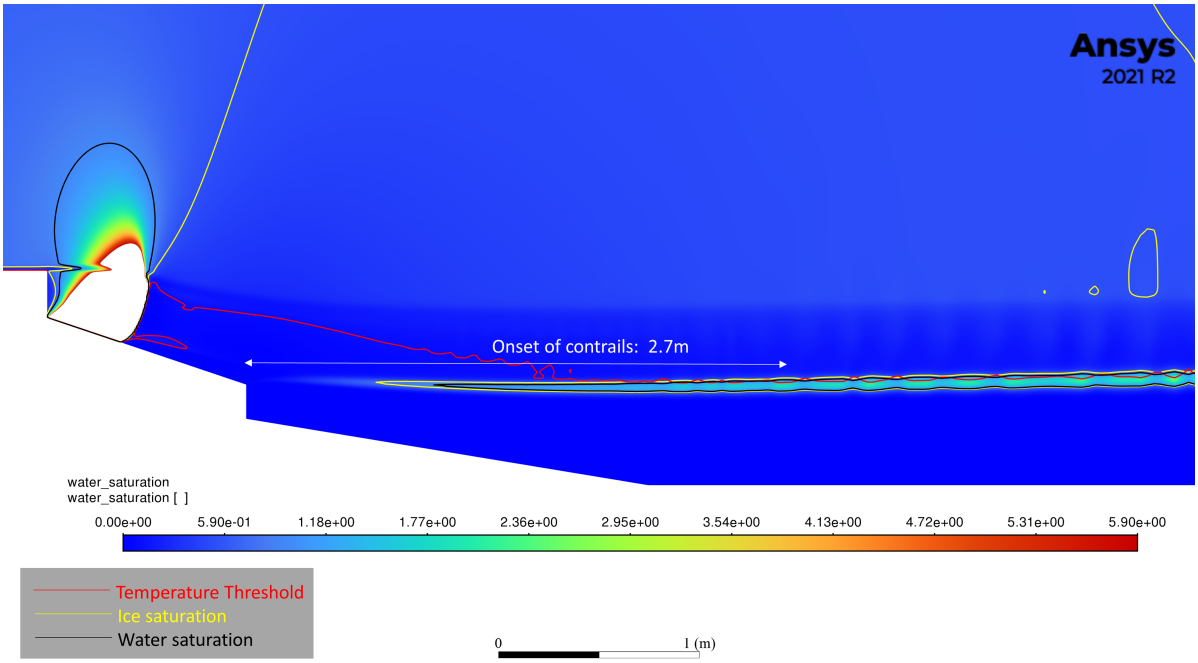

Figure 6.9: Contour of the water vapour saturation in the very near-field of the Leap-1A engine for ambient humidity of 79% (ISSR), as predicted by the Contrail Formation Model, with imposed criteria for contrail formation, and the distance to onset of contrails annotated

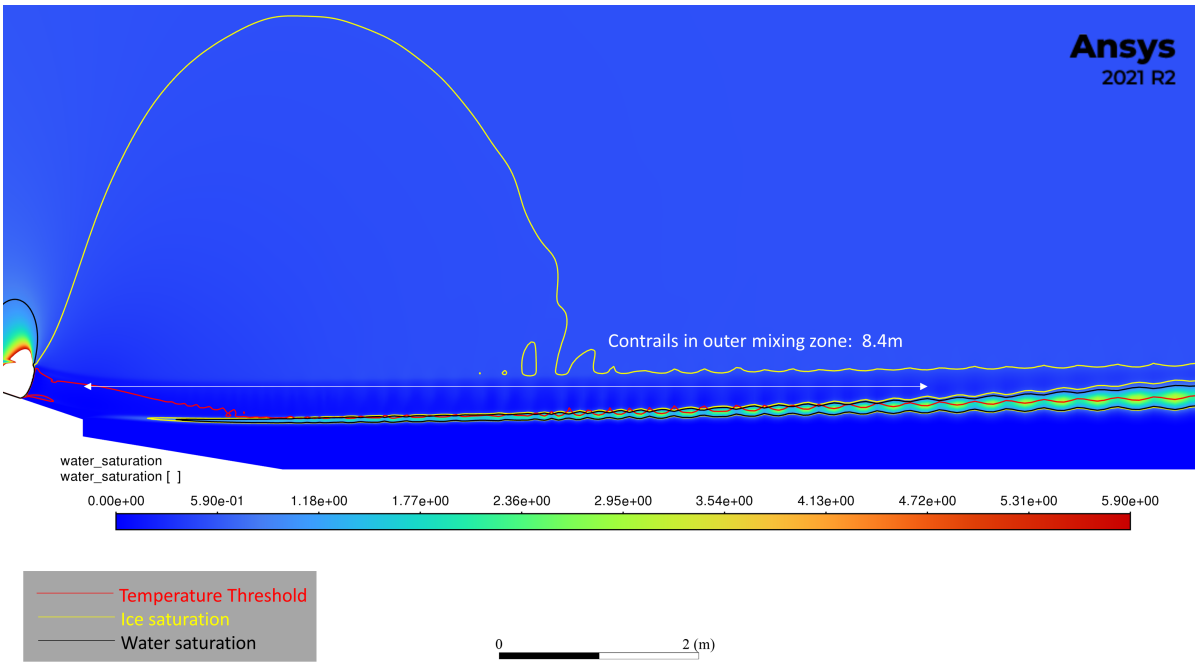

Figure 6.10: Contour of the water vapour saturation in the near-field of the Leap-1A engine for ambient humidity of 79% (ISSR), as predicted by the Contrail Formation Model, with imposed criteria for contrail formation, and the distance to the appearance of contrails in the outer mixing zone annotated

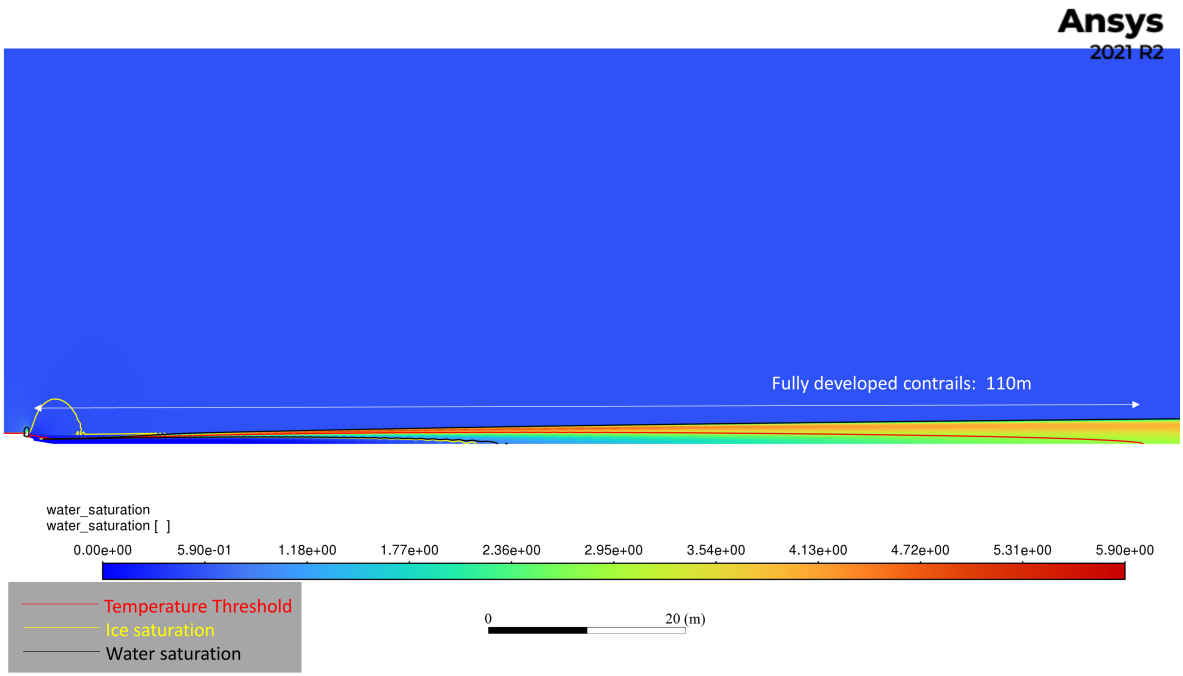

Figure 6.11: Zoomed-out contour of the water vapour saturation in the exhaust of the Leap-1A engine for ambient humidity of 79% (ISSR), as predicted by the Contrail Formation Model, with imposed criteria for contrail formation, and the distance to fully developed contrails annotated

From the contour plots in Figure 6.6 to Figure 6.11, it can be observed that for both dry ambient conditions and ISSR conditions, it is predicted that contrails are formed based on the criteria. However, their development differs between both cases. These differences are summarized in Table 6.3.

Ambient humidity [%]	Onset [m]	Outer Mixing Zone [m]	Full jet [m]	Dissipation [m]
0	4.0	9.3	115	-
79 (ISSR)	2.7	8.4	110	-

Table 6.3: Location of contrail formation and dissipation for two ambient conditions: Dry air and an Ice Supersaturated Region

6.8.3. Comparison of mixing lines to SAC predictions

One of the main objectives of this research is to investigate the accuracy of the Schmidt - Appleman Criterion in predicting contrail formation from modern (U)HBPR turbofan engines. The SAC is based on a single mixing line representing the flow from an engine, which is then compared to the saturation curves for water and ice to determine whether criteria for contrail formation have been met. This process has been described in section 2.4. Now that a complete model has been developed that determines the water vapour partial pressure and temperature in the exhaust field, this data can be used to generate mixing lines for comparison. This is done by injecting massless particles at the core nozzle boundary and tracking their path through the flow. Along these particle paths, the flow properties can then also be tracked, and the evolution of these properties can be plotted against each other. If water vapour partial pressure is plotted against temperature, the result is a mixing line that can be compared to the SAC mixing line. However, by tracking multiple particles that are injected, emanating from the entire length of the core nozzle boundary, a complete set of mixing lines is generated instead of just one mean. The result is a "fan" of mixing lines representing the entire flow from the core jet. In theory, this approach could be extended to include mixing lines from the bypass boundary. However, one of the prerequisites for the formation of contrails in the exhaust is the existence of soot particles as Cloud Condensation Nuclei, which only come from the core flow. Therefore, particle pathways from the bypass nozzle are not included in this comparison. The resulting plots for dry ambient conditions and ISSR conditions can be seen in Figure 6.12 and Figure 6.13 respectively.

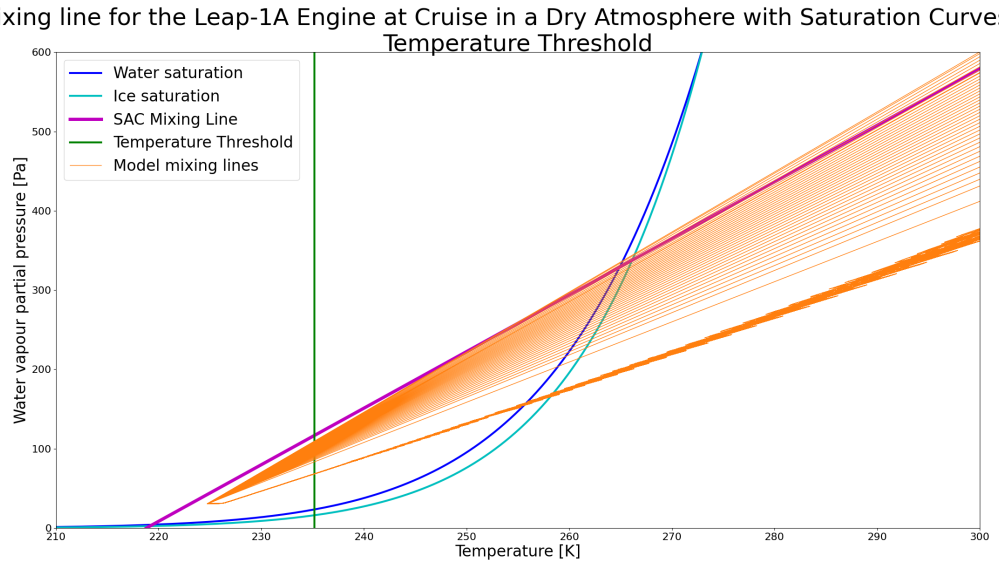

Figure 6.12: Mixing lines at the exhaust jet axis and the core nozzle center as predicted by the model, compared to the SAC mixing line, with saturation curves and temperature threshold, for dry ambient conditions (zoomed in)

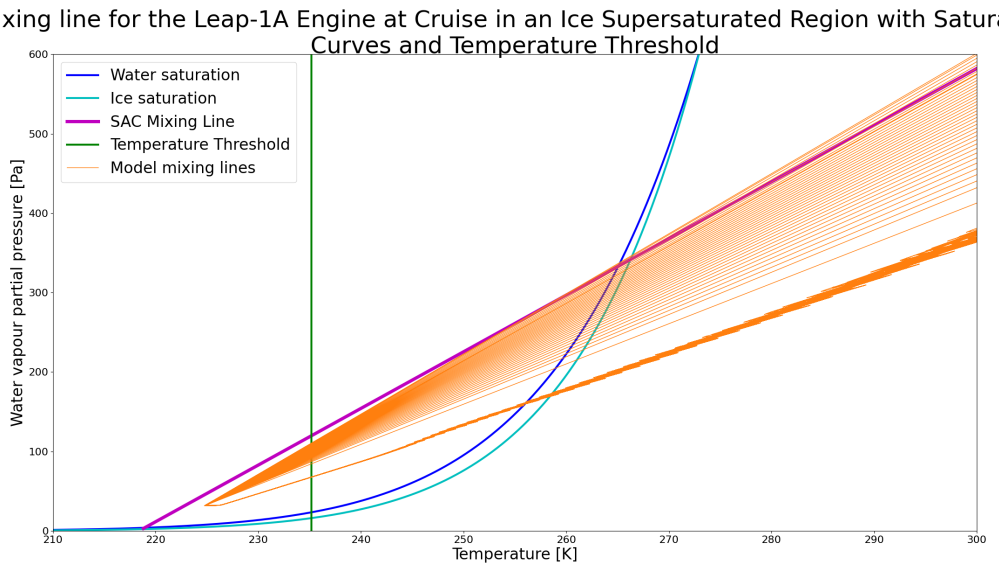

Figure 6.13: Mixing lines at the exhaust jet axis and the core nozzle center as predicted by the model, compared to the SAC mixing line, with saturation curves and temperature threshold, for ISSR conditions (zoomed in)

From the comparison of mixing lines between the SAC and the Contrail Formation Model, the following observations can be made::

- The set of mixing lines from the core nozzle of the engine is represented by a fan of lines that converges towards ambient conditions. This indicates that the single straight mixing line from the SAC is a simplification of reality, as was expected.
- The SAC mixing line is close to the upper limit of the set of mixing lines predicted by the model. This also matches expectations, as the flow from the core nozzle is hotter than the mean temperature of the total exhaust flow which includes the bypass and is used for the SAC mixing line.
- For the Leap-1A case study, this difference does not result in a discrepancy in whether contrails are predicted to form. The mixing lines still all cross above water saturation, which corresponds to the contrails being formed over the entire span of the jet.
- The mixing lines given by the model do not extend fully to the ambient conditions. This indicates that the end of the domain is reached before the center of the jet has returned to ambient conditions.

6.9. Conclusion

From the validation process, the following conclusions can be drawn with respect to the validity of this module for predicting contrail formation:

- Prediction of dilution ratio as a function of plume age is within the expected range when compared to literature. Its slope is identical to that of empirical formulas for modern turbofan engines. Its magnitude is lower than the comparable cases from literature. This discrepancy falls within the expected range of variation.
- The prediction of water vapour saturation as well as onset of contrail formation shows good agreement with the validation case. This give confidence for the use of this model for contrail formation prediction.

The results from the case study done on the Leap-1A engine at cruise conditions in this chapter can be summarized as follows:

- For dry ambient conditions, the Leap-1A engine produces non-persistent contrails fully developed over the jet width from 163 meters to 258 meters behind the nozzle.

- For ISSR conditions, the Leap-1A engine produces persistent contrails fully developed over the jet width from 115.10 meters onwards.

The comparison of mixing lines from the current model to the SAC mixing line yields the following conclusions:

- It can be concluded that the SAC overestimates the slope of the majority of mixing lines from the core nozzle for engines with a bypass. The larger the bypass ratio, the greater this effect will be, as the mean temperature which is used to determine this slope is brought down further for larger bypass ratios compared to the core jet temperature.
- In the current case, there is no discrepancy in contrail formation prediction between the SAC and the Contrail Formation Model. The mixing lines still pass above water saturation and beyond the temperature threshold.
- Further research into edge cases needs to be done to determine whether there are situations in which the SAC predicts contrail formation where the current Contrail Formation Model does not.
- For completeness and consistency, it is recommended that the current research is repeated for a larger domain. This way, it can be ensured that mixing lines fully return to ambient conditions before the end of the domain is reached.

In the final chapter, the research questions will be revisited and answered where possible based on the results from this model. In addition, recommendations for future research will be done.

7

Conclusions and Recommendations

The model framework for the prediction of contrail formation from modern (U)HBPR engines has now been developed and validated, and results have been generated for a case study of the Leap-1A engine. This means the Research Questions laid out in section 2.6 can now be revisited and answered based on these results. This is done in section 7.1.

7.1. Answering the Research Questions

1. **What is the effect of the mixing physics of core & bypass flow on contrail formation from modern High Bypass Ratio (HBPR) aircraft turbofan engines?**

   (a) *To what extent does HBPR exhaust mixing deviate from isobaric, instantaneous mixing?*
   The results of the Flow Field Solver in chapter 5 show that the mixing in the exhaust is neither isobaric nor instantaneous. The flow coming from the core nozzle is in most cases fully expanded and its pressure is therefore equal to ambient pressure. However, the bypass nozzle can be choked and exhibit a higher pressure than that of the ambient air. In addition, the flow properties emerging from the core and bypass nozzle show significant differences close to the engine. The complete exhaust only approaches the characteristics of a simple jet beyond the initial merging zone and intermediate zone.

   (b) *What is the effect of non-instantaneous non-isobaric mixing on the condensation process?*
   In chapter 6, the dispersion of water vapour in the exhaust has been modelled. This results in the generation of contrail contours as well as mixing lines. The case study done for the Leap-1A engine shows that persistent contrails are formed for ISSR conditions, and non-persistent contrails for dry ambient conditions. Whereas instantaneous, isobaric mixing results in straight mixing line, the curved nature of mixing lines in the Leap-1A case study reflects the non-instantaneous, non-isobaric nature of the real contrail formation process.

   (c) *What is the influence of key design parameters (such as) Bypass Ratio (BPR) and Overall Pressure Ratio (OPR) on exhaust mixing physics?*
   The influence of OPR has been left out of the scope for the current research. However, the influence of BPR can be inferred from the results of the model framework for the Leap-1A case study. For modern (U)HBPR engines, the bypass flow becomes more and more dominant in terms of mass flow and jet radius with respect to the core jet flow, with the case study for example exhibiting a BPR of 11.9. As the bypass flow consists of ambient air, which is cold and dry compared to the engine core flow, the evolution of temperature and water vapour content follows a different trajectory than predicted by the SAC, as this calculates a single mixing line slope based on the average temperature and water content of the complete exhaust. The higher the BPR, the larger this discrepancy, and the higher the initial temperature and water vapour content when compared to the average of the complete exhaust.

2. **How can the Schmidt-Appleman Criterion (SAC) be extended or improved to better predict contrail formation from HBPR aircraft turbofan engines?**

(a) *How accurate is the current, broadly used criterion in predicting contrail formation from HBPR engines?*
For the case study performed on the Leap-1A engine, the results show agreement with the SAC in the prediction of contrails for both dry and ambient conditions. However, when comparing the mixing lines for both methods, it can be observed that the SAC approaches an upper limit with respect to the mixing lines predicted by the current model. This can be explained by the fact that the core jet, from which the contrails are formed, exhibits a higher temperature than the average of the entire jet. Therefore, the resulting mixing lines have a lower gradient than predicted by the SAC. This indicates that the SAC may predict contrails to be formed in certain cases where the current model would not. As a fraction of the mixing lines predicted by the model also extends above the SAC line, there may also be edge cases where partial contrails are formed that would not be predicted by the SAC.

(b) *What modifications or extensions can be implemented to improve the accuracy of the SAC for these engines?*
The results from the work done in this research do not immediately support a simple mathematical adjustment to the equations used in the SAC that would help it better reflect the mixing in the exhaust of modern turbofan engines. However, the framework that has been presented can be used to model any modern engine and compare the results to the predictions of the SAC.

7.2. Recommendations

The current research has resulted in a complete and validated modelling framework for the prediction of contrails in the exhaust of modern HBPR turbofan engines. From the lessons learned in the course of the development of this framework, several recommendations can be made. With respect to improvements on the current state of the modelling blocks, these recommendations include the following:

- Improve the flow of information between the various modelling steps by synthesizing them in a single overall modelling chain. For example, an overarching model can be set up using Python-designed structure where the modelling steps are called one by one and their outputs and inputs are directly linked. This would reduce the amount of user input required and make the framework more flexible in its application to different engine models and conditions.
- Investigate the remaining questions with respect to the accuracy of the Flow Field Solver module in resolving the very near field of the engine exhaust. Specifically, the estimation of the potential core length in validation studies as well as the fluctuations in flow field variables in the case study can be taken as starting points for further investigation and possible improvements. It is suggested that a fully 3D analysis of the flow field is done to determine the effect of the 2D axisymmetric assumption used in the current model. Additionally, modelling the flow within the exhaust nozzles themselves can provide additional insight into the origin of the aforementioned fluctuations in flow field variables.
- Although the water vapour dispersion and resulting contrail formation predicted by the current model shows good agreement with validation cases, it is worth noting that the current iteration of the model only accounts for basic aspects of the microphysical processes involved in contrail formation, such as the temperature threshold for homogeneous freezing and the requirement of soot particles for nucleation. From literature, it is known that more complex phenomena occur in reality. It is recommended that the effect of including these processes is studied in future research.

The results of the current research can also serve as a starting point for further research in other areas:

- The necessity of accurately predicting contrail formation arises from their significant climate impact and the importance of reducing this impact for the continued habitability of our planet. Therefore, a very valuable next step would be to use the current modelling framework as a tool in the improvement of the design of modern HBPR turbofan engines with respect to their formation of contrails. Just as designs are currently optimized with respect to parameters such as maximum thrust, TSFC, noise, and NO_x emissions, their propensity to form contrails in the exhaust can be added as a parameter to consider in the design process.
- The engine design is one of the two factors that determine whether contrails are formed for a given flight. The other is the ambient condition. With a better method of predicting contrail formation,

aircraft flight paths can potentially also be adjusted to avoid this. Further research into the feasibility of this approach is recommended.

- The current research has been centered around the influence of engine BPR on the formation of contrails. In future research, other engine design parameters such as OPR can also be included. The better the understanding of the relation between various design parameters and the formation of contrails, the more intelligently a future engine can be designed with contrail formation in mind.

Bibliography

[1] H. Appleman. The formation of exhaust condensation trails by jet aircraft. *Bulletin of the American Meteorological Society*, 34(1):14 – 20, 1953. doi: 10.1175/1520-0477-34.1.14.

[2] Jorge Bardina, P. Huang, and T. Coakley. Turbulence modeling validation, testing, and development. *NASA Technical Memorandum*, 05 1997.

[3] Guido Buresti, Alessandro Talamelli, and Paolo Petagna. Experimental characterization of the velocity field of a coaxial jet configuration. *Experimental Thermal and Fluid Science*, 9(2):135–146, 1994. ISSN 0894-1777. doi: https://doi.org/10.1016/0894-1777(94)90106-6. URL https://www.sciencedirect.com/science/article/pii/0894177794901066. Special Issue on Measurement in Turbulent Flow.

[4] Sebastien Cantin, François Morency, and François Garnier. Modeling capabilities on the formation of contrails in a commercial cfd code. 09 2019.

[5] Werner J. A. Dahm, Clifford E. Frieler, and Grétar Tryggvason. Vortex structure and dynamics in the near field of a coaxial jet. *Journal of Fluid Mechanics*, 241:371–402, 1992. doi: 10.1017/S0022112092002088.

[6] John Daintith. A dictionary of chemistry, 2008. URL https://www.oxfordreference.com/view/10.1093/acref/9780199204632.001.0001/acref-9780199204632-e-1190.

[7] I. Dedoussi. Lecture: Aircraft emissions and climate effects, part 11. 2020.

[8] V. Grewe. Lecture: Aircraft emissions and climate effects, part 2. 2020.

[9] V. Grewe. Lecture: Aircraft emissions and climate effects, part 3. 2020.

[10] V. Grewe. Lecture: Aircraft emissions and climate effects, part 6. 2020.

[11] Silvano Grizzi. Experimental investigation of the near-field noise generated by a compressible round jet. *Journal of Physics: Conference Series*, 318:092003, 12 2011. doi: 10.1088/1742-6596/318/9/092003.

[12] Y. Hardalupas, A. M. K. P. Taylor, James Hunter Whitelaw, and Felix Jiri Weinberg. Velocity and particle-flux characteristics of turbulent particle-laden jets. *Proceedings of the Royal Society of London. A. Mathematical and Physical Sciences*, 426(1870):31–78, 1989. doi: 10.1098/rspa.1989.0117. URL https://royalsocietypublishing.org/doi/abs/10.1098/rspa.1989.0117.

[13] Eric S. Hendricks and Justin S. Gray. pycycle: A tool for efficient optimization of gas turbine engine cycles. *Aerospace*, 6(8), 2019. ISSN 2226-4310. doi: 10.3390/aerospace6080087. URL https://www.mdpi.com/2226-4310/6/8/87.

[14] Stefan Hickel. CFD for Aerospace Engineers: Lecture notes part 4. 2020.

[15] J.O. Hinze and B.G. Van Der Hegge Zijnen. Transfer of heat and matter in the turbulent mixing zone of an axially symmetrical jet. *Appl. Sci. Res.*, 1949. doi: https://doi.org/10.1007/BF02120346.

[16] Intergovernmental Panel on Climate Change. Climate change 1995: Ipcc second assessment report. 1995.

[17] Intergovernmental Panel on Climate Change. Summary for policymakers. *Global Warming of 1.5° C. An IPCC Special Report on the impacts of global warming of 1.5° C above pre-industrial levels and related global greenhouse gas emission pathways, in the context of strengthening the global response to the threat of climate change, sustainable development, and efforts to eradicate poverty*, 2018.

[18] N. W. M. Ko and A. S. H. Kwan. The initial region of subsonic coaxial jets. *Journal of Fluid Mechanics*, 73 (2):305–332, 1976. doi: 10.1017/S0022112076001389.

[19] Bernd Kärcher. Formation and radiative forcing of contrail cirrus. *Nature Communications*, 9, 12 2018. doi: 10.1038/s41467-018-04068-0.

[20] David S. Lee, David W. Fahey, Piers M. Forster, Peter J. Newton, Ron C.N. Wit, Ling L. Lim, Bethan Owen, and Robert Sausen. Aviation and global climate change in the 21st century. *Atmospheric Environment*, 43(22):3520–3537, 2009. ISSN 1352-2310. doi: https://doi.org/10.1016/j.atmosenv.2009.04.024. URL https://www.sciencedirect.com/science/article/pii/S1352231009003574.

[21] D.S. Lee, G. Pitari, V. Grewe, K. Gierens, J.E. Penner, A. Petzold, M.J. Prather, U. Schumann, A. Bais, T. Berntsen, D. Iachetti, L.L. Lim, and R. Sausen. Transport impacts on atmosphere and climate: Aviation. *Atmospheric Environment*, 44(37):4678–4734, 2010. ISSN 1352-2310. doi: https://doi.org/10.1016/j.atmosenv.2009.06.005. URL https://www.sciencedirect.com/science/article/pii/S1352231009004956.

[22] D.S. Lee, D.W. Fahey, A. Skowron, M.R. Allen, and U. Burkhardt. The contribution of global aviation to anthropogenic climate forcing for 2000 to 2018. *Atmospheric Environment*, 244:117834, 2021. ISSN 1352-2310. doi: https://doi.org/10.1016/j.atmosenv.2020.117834.

[23] Timothy M. Lenton, Hermann Held, Elmar Kriegler, Jim W. Hall, Wolfgang Lucht, Stefan Rahmstorf, and Hans Joachim Schellnhuber. Tipping elements in the earth's climate system. *Proceedings of the National Academy of Sciences*, 105(6):1786–1793, 2008. ISSN 0027-8424. doi: 10.1073/pnas.0705414105. URL https://www.pnas.org/content/105/6/1786.

[24] Lenton, T. et al. Climate tipping points — too risky to bet against; the growing threat of abrupt and irreversible climate changes must compel political and economic action on emissions. *Nature*, 2019.

[25] Mercator Research Institute on Global Commons and Climate Change. That's how fast the carbon clock is ticking. https://www.mcc-berlin.net/en/research/co2-budget.html, April 2021.

[26] Nieuwerth et al. Green flying: Final report. *Delft Technical University*, 2018.

[27] NLR - Royal Netherlands Aerospace Centre. Gsp - gas turbine simulation program. https://www.gspteam.com/, February 2023.

[28] NPARC Alliance CFD Verification and Validation Web Site. Examining spatial (grid) convergence. https://www.grc.nasa.gov/www/wind/valid/tutorial/spatconv.html, 2021. Accessed: 2022-12-13.

[29] OpenCFD Ltd. Openfoam user guide. https://www.openfoam.com/documentation/user-guide, 2023. Accessed: 2023-18-02.

[30] Riadh Ouzani, Sofiane Khelladi, and Amélie Danlos. Mixing in turbulent compressible heated coaxial jets: A numerical study. *International Journal of Hydrogen Energy*, 45:1–27, 2020. doi: 10.1016/j.ijhydene.2020.01.194. URL https://hal.archives-ouvertes.fr/hal-02502343.

[31] Jeffrey L. Peters. New techniques for contrail forecasting. Technical report, Air Weather Service, 1993.

[32] M. M. Ribeiro and J. H. Whitelaw. Coaxial jets with and without swirl. *Journal of Fluid Mechanics*, 96(4):769–795, 1980. doi: 10.1017/S0022112080002352.

[33] SAE. Gas turbine engine performance station identification and nomenclature, aerospace recommended practice.

[34] U. Schumann, J. Ström, R. Busen, R. Baumann, K. Gierens, M. Krautstrunk, F. P. Schröder, and J. Stingl. In situ observations of particles in jet aircraft exhausts and contrails for different sulfur-containing fuels. *Journal of Geophysical Research: Atmospheres*, 101(D3):6853–6869, 1996. doi: https://doi.org/10.1029/95JD03405. URL https://agupubs.onlinelibrary.wiley.com/doi/abs/10.1029/95JD03405.

[35] Ulrich Schumann, Hans Schlager, Frank Arnold, Robert Baumann, Peter Haschberger, and Otto Klemm. Dilution of aircraft exhaust plumes at cruise altitudes. *Atmospheric Environment*, 32(18):3097–3103, 1998.

[36] D. Sonntag. Advancements in the field of hygrometry. *Meteorologische Zeitschrift*, 3(2):51–66, 05 1994. doi: 10.1127/metz/3/1994/51. URL http://dx.doi.org/10.1127/metz/3/1994/51.

[37] Christopher K. W. Tam. Mach wave radiation from high-speed jets. *AIAA Journal*, 47(10):2440–2448, 2009. doi: 10.2514/1.42644. URL https://doi.org/10.2514/1.42644.

[38] Fernando Tejero, Matthew Robinson, David G. MacManus, and Christopher Sheaf. Multi-objective optimisation of short nacelles for high bypass ratio engines. *Aerospace Science and Technology*, 91: 410–421, 2019. ISSN 1270-9638. doi: https://doi.org/10.1016/j.ast.2019.02.014. URL https://www.sciencedirect.com/science/article/pii/S1270963818315724.

[39] Merijn Rembrandt van Holsteijn, Arvind Gangoli Rao, and Feijia Yin. Operating characteristics of an electrically assisted turbofan engine. In *Turbo Expo: Power for Land, Sea, and Air*, volume 84058, page V001T01A028. American Society of Mechanical Engineers, 2020.

[40] H.A. Warda, S.Z. Kassab, K.A. Elshorbagy, and E.A. Elsaadawy. An experimental investigation of the near-field region of a free turbulent coaxial jet using lda. *Flow Measurement and Instrumentation*, 10(1):15–26, 1999. ISSN 0955-5986. doi: https://doi.org/10.1016/S0955-5986(98)00041-7. URL https://www.sciencedirect.com/science/article/pii/S0955598698000417.

[41] Dustin Weaver and Sanja Miskovic. A study of rans turbulence models in fully turbulent jets: A perspective for cfd-dem simulations, Jul 2021. URL https://open.library.ubc.ca/collections/facultyresearchandpublications/52383/items/1.0401914.

[42] John Wright, Keith Gillis, Aaron Johnson, and Ida Shinder. Back pressure ratio and the transonic resonance mechanism of low unchoking in critical flow venturis. FLOMEKO 2016, Sydney, AU, 2016-09-28 04:09:00 2016. URL https://tsapps.nist.gov/publication/get_pdf.cfm?pub_id=921668.

[43] Israel J. Wygnanski and Heinrich E. Fiedler. Some measurements in the self-preserving jet. *Journal of Fluid Mechanics*, 38:577 – 612, 1969.

A

Semi-Empirical Approach

The mathematical derivations for the Semi-Empirical Flow Field Solver from chapter 5 are described here, in three consecutive iterations.

Approach (version 1)

Discrete small steps dx are taken in axial direction, for which the entrained velocity v_e is calculated. Whereas the original entrainment theory assumes a single average jet velocity along the radius, here the jet is also divided into discrete steps dr in radial direction. This results in a flow field that is divided into cells with dimensions dx and dr. The MTT law is then applied to each cell, determining the change in velocity and radius based on entrainment from adjacent cells, and conservation of mass and momentum. In Figure A.1 and Figure A.2, the discretization and its nomenclature can be seen.

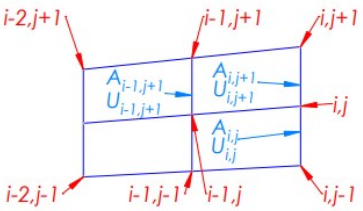

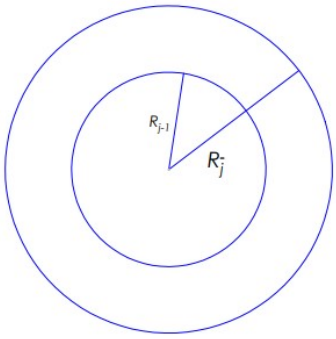

Figure A.1: Numbering convention used by the semi-empirical model (side view)

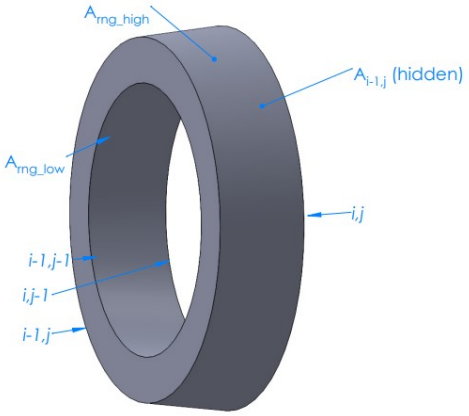

Figure A.2: Numbering convention used by the semi-empirical model (3D ring representation)

Assumptions

- Fixed entrainment coefficient $\alpha = 0.057$, corresponding to a pure momentum jet. [7]

- Conservation of mass and momentum (in x direction) applies to each individual cell.
- Flow is incompressible, and density and pressure are uniform for the purposes of mass flow and velocity calculations.
- $dx << dr$, such that prediction of values at station x_i, r_j can be based on values from previous stations x_{i-1}, r_j and x_{i-1}, r_{j-1}

Derivation of Equations

To calculate the change in velocity δU as well as the growth in cross-sectional area δA for each cell, the fundamental laws for conservation of mass and momentum are used. Because there are only two unknowns, only the equations in x direction are required.

Conservation of Mass

In Figure A.3, the mass flows in and out of a single cell can be seen. For conservation of mass to hold, the sum of these flows should be zero, else mass would have to be created or destroyed within the cell. The mass flow $\dot{m}_i$ through the cross section of station $x[i]$ is expressed as:

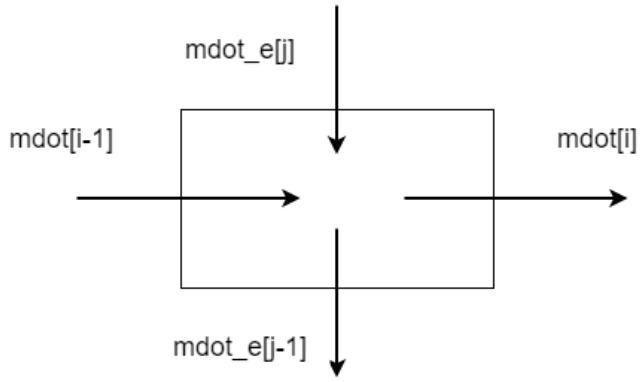

Figure A.3: Mass flows in and out of a single cell

$$\dot{m}_i = \rho A_i U_i, \tag{A.1}$$

where A_i is the cross sectional area and U_i the axial velocity, and the net entrained mass flow summarized in $\delta \dot{m}$ as follows:

$$\delta \dot{m} = \dot{m}_{e_j} - \dot{m}_{e_{j-1}} \tag{A.2}$$

The resulting expression for conservation of mass across a single cell can then be seen in Equation A.3:

$$\rho A_{i-1} U_{i-1} + \delta \dot{m} = \rho A_i U_i \tag{A.3}$$

The goal is to find the changes in velocity and area, δU and δA respectively, so A_i and U_i are rewritten to introduce those variables:

$$A_i = A_{i-1} + \delta A \tag{A.4}$$
$$U_i = U_{i-1} + \delta U \tag{A.5}$$

The new expression for conservation of mass then becomes:

$$\rho A_{i-1} U_{i-1} + \delta \dot{m} = \rho (A_{i-1} + \delta A)(U_{i-1} + \delta U) \tag{A.6}$$

Expanding, neglecting higher-order terms, and rewriting for δU as function of δA and the other, known, quantities, yields the first expression in the system of two equations that needs to be solved, shown in Equation A.7:

$$\delta U = \frac{1}{A_{i-1}}\left(\frac{\delta \dot{m}}{\rho} - U_{i-1}\delta A\right) \tag{A.7}$$

Conservation of Momentum
The second expression will come from the conservation of momentum in axial direction, which for a constant density flow is given by Equation A.8:

$$A_{i-1}U_{i-1}^2 = A_i U_i^2 \tag{A.8}$$

As with the first expression, this is rewritten for δU and δA:

$$A_{i-1}U_{i-1}^2 = (A_{i-1} + \delta A)(U_{i-1} + \delta U)^2 \tag{A.9}$$

Again expanding the terms and rewriting for δU, the second expression is found, given by Equation A.10:

$$\delta U = -\delta A \frac{U_{i-1}}{2A_{i-1}} \tag{A.10}$$

Now it is only a simple matter of combining Equation A.7 and Equation A.10:

$$\frac{1}{A_{i-1}}\left(\frac{\delta \dot{m}}{\rho} - U_{i-1}\delta A\right) = -\delta A \frac{U_{i-1}}{2A_{i-1}} \tag{A.11}$$

and consequently solving for δA:

$$\delta A = 2\frac{\delta \dot{m}}{\rho U_{i-1}} \tag{A.12}$$

Finally, δU can be determined by plugging in Equation A.12 into either Equation A.7 or Equation A.10, resulting in the expression given by Equation A.13:

$$\delta U = -\frac{\delta \dot{m}}{\rho A_{i-1}} \tag{A.13}$$

Approach (version 2)

At this point, the basic entrainment model produces plausible results for a jet with uniform exit velocity and no co-flow. However, these results are dependent on numerical factors such as the step width in radial direction, in a manner that suggests improvements still need to be made before a valid model can be achieved. These additional steps are described here.

- Take into account entrained momentum for a non-zero co-flow velocity.
  If the jet exists in a stationary medium, the total momentum inside the jet should not increase, and assuming no dissipation of energy into smaller turbulence scales, should not decrease either. However, the model is meant to be accurate for a turbofan engine in cruise conditions, so this qualification does not apply. When entraining surrounding air into the exhaust during cruise, this surrounding air already has velocity and therefore momentum relative to the stationary nozzle. This momentum is carried into the jet and needs to be taken into account. Because the entrained mass flow is known from Equation 5.10, the change in entrained momentum at every step is simply given by:

  $$dP = \dot{m}_e U_a, \tag{A.14}$$

  where U_a is the ambient air velocity.

- Improve accuracy of entrained velocity calculations, by implementing an estimate for the velocity at the current station, instead of taking the value from the previous station.
  In the original approach, one of the main challenges was using the correct initial values for the calculation of flow properties within every cell. When looking at Equation 5.9, for example, its value depends on the difference between the velocity at the current location and the velocity in the upper neighbouring cell. However, neither of these values are known at this step in the calculations, because entrained

velocity is one of the parameters required to calculate this very value. There is a problem with circular prerequisites here. The initial approach was to assume the velocity difference between two neighbouring cells is small, and therefore as a starting point U_{i-1} can be used in the place of U_i, after which an iterative procedure is used to converge to the correct values. However, this approach is still flawed, because the reliance on values from previous cells creates a "delay" in the information being passed between cells. This can be seen in the fact that dividing the jet into more radial steps leads to significant changes in the prediction of flow velocity. A clear example of this arises when comparing the predicted center-line velocity U_0 for two different numbers of radial steps: The calculation with 100 radial steps results in much less of a velocity change along the center-line than the one with 10 steps.
The suggested improvement is as follows: In stead of assuming the change in velocity is minimal from the previous cell to the current one, the assumption is made that the change in velocity is approximately equal to the previous change in velocity. Written out in the form of equations:

$$U_{i,j} = U_{i-1,j} + \delta U_{i-1,x}, \tag{A.15}$$

$$\delta U_{i-1,x} = U_{i-1} - U_{i-2} \tag{A.16}$$

Similarly, for the cell value of the upper neighbouring cell:

$$U_{i,j+1} = U_{i-1,j} + \delta U_{i-1,r}, \tag{A.17}$$

$$\delta U_{i-1,r} = U_{i-1,j+1} - U_{i-1,j} \tag{A.18}$$

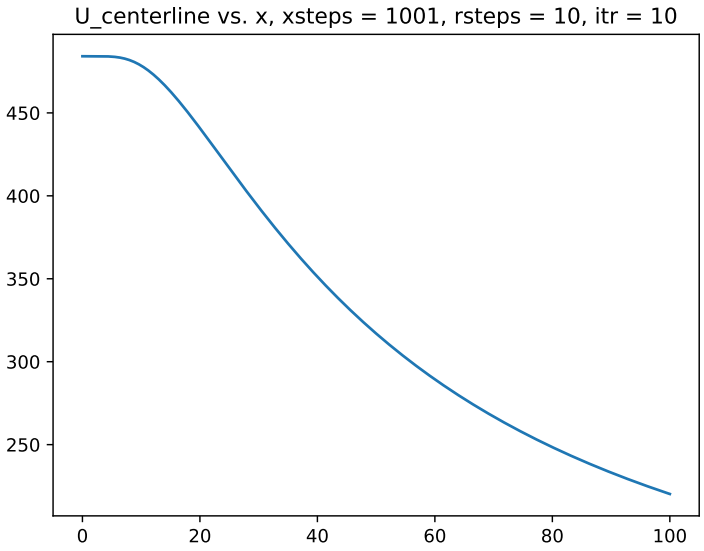

Figure A.4: Center-line velocity as predicted by the semi-empirical model when the radius is divided into 10 steps

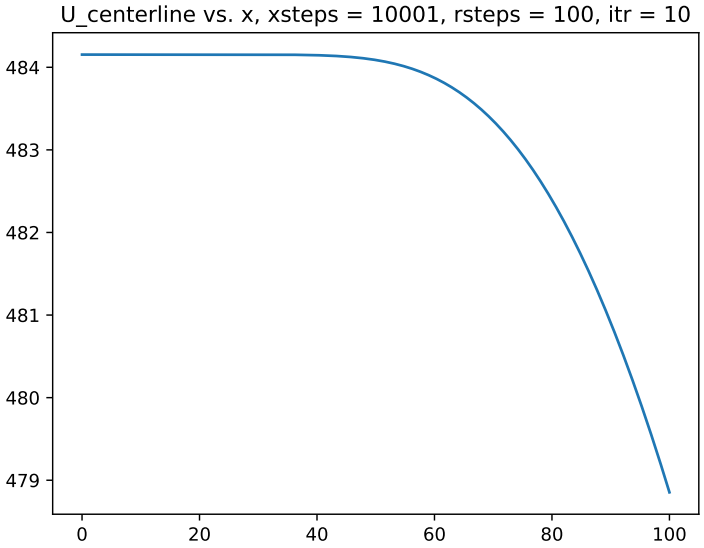

Figure A.5: Center-line velocity as predicted by the semi-empirical model when the radius is divided into 100 steps

Approach (version 3)

While the approach in the second iteration shows some improvement, it still is characterized by the same flaw: accuracy seems to be inversely related to the resolution of the grid on which the problem is solved. Therefore, yet another approach to the semi-empirical model is suggested: A set of algebraic equations is set up using the Finite Difference Method, and is then solved using linear regression. The approach and its underlying assumptions as well as limitations are treated here.

Velocity Field sub-module

1. **Partial Differential Equation**
   In order to design a model that is both accurate and feasible, a tradeoff needs to be made between the two. If pure accuracy in terms of describing physical mechanisms is pursued to the exclusion of other considerations, one will arrive at either a real physical experiment or a Direct Numerical Simulation (DNS). This type of model is, however, not feasible in terms of time constraints and computational resource availability. Similarly, if a model is set up that is too simplistic and has assumptions that make the results unreliable, it might be feasible to make, but does not have sufficient predictive power to be useful for the purposes of answering the research question. With this tradeoff in mind, the decision was made to employ a semi-empirical approach to the Partial Differential Equation (PDE) for this model. In the case of velocity, this results in a quasi-3D description of the axial velocity field, with the following initial assumptions:

   - Incompressible flow with constant density
   - Rotationally symmetrical flow: $\frac{\partial}{\partial \theta} = 0$
   - Axisymmetrical flow: Domain is defined from the jet center-line upwards
   - Zero pressure gradient: $\nabla p = 0$
   - Axial velocity depends on entrainment assuming a pure jet, according to the Morton - Taylor - Turner (MTT) Law (restatement of Equation 5.9):

$$v_e = \alpha * (U_i - U_o) \tag{A.19}$$

   These assumptions result in the following system of PDEs for the axial, radial, and rotational velocities respectively:

$$\frac{\partial U_x}{\partial x} - \frac{\alpha}{r}\frac{\partial}{\partial r}(r\frac{\partial U_x}{\partial r}) = 0 \tag{A.20}$$

$$U_r = \alpha\frac{\partial U_x}{\partial r} \tag{A.21}$$

$$U_\theta = 0 \tag{A.22}$$

The term $\frac{\alpha}{r}\frac{\partial}{\partial r}(r\frac{\partial U_x}{\partial r})$ in the first equation comes from the application of the derivative chain rule to the Laplacian ∇^2 in radial direction for a cylindrical coordinate system. Expanding this term further, and again applying the chain rule, leads to an expression that can easier be transformed into a Finite Difference equation:

$$\frac{\partial U_x}{\partial x} - \frac{\alpha}{r}(\frac{\partial U_x}{\partial r} + r\frac{\partial^2 U_x}{\partial r^2}) = 0 \tag{A.23}$$

2. **Finite Difference Expression**
Using a Central Difference approximation for the derived from a Taylor Series expansion around point $[i, j]$, and the assumption that the radius r at radial grid point j can be written as $r = j\Delta r$, the following Finite Difference expression can be found:

$$\frac{U_{x_{i+1}} - U_{x_{i-1}}}{2\Delta x} - \frac{\alpha}{2\Delta r^2}\left[U_{j+1}\frac{2j+1}{j} + U_j(-4) + U_{j-1}\frac{2j-1}{j}\right] = 0 \tag{A.24}$$

This expression is split into axial and radial directions:

$$\frac{U_{x_{i+1}} - U_{x_{i-1}}}{2\Delta x} = 0 \tag{A.25}$$

$$-\frac{\alpha}{2\Delta r^2}\left[U_{j+1}\frac{2j+1}{j} + U_j(-4) + U_{j-1}\frac{2j-1}{j}\right] = 0 \tag{A.26}$$

3. **Boundary Conditions**
The 2D domain has four boundaries on which conditions need to be specified.:

   - The left boundary represents the plane perpendicular to the axial direction, at the end of the nozzle. Therefore it is defined by a Dirichlet boundary condition specifying the axial velocity of the jet, bypass, and ambient air:

$$\text{for } i = 0, j = 0 : J$$

$$\begin{aligned}&\text{if } r \leq R_{core} : U_{i,j} = U_{core}\\ &\text{if } R_{core} < r \leq R_{bypass} : U_{i,j} = U_{bypass}\\ &\text{if } r > R_{bypass} : U_{i,j} = U_{ambient}\end{aligned}$$

   - The lower boundary represents the jet center-line, as the flow is symmetrical in this axis and only the upper part is resolved. This is therefore a symmetry axis, defined by the one-sided expression for a Neumann boundary:

$$\text{for } i = 0 : I, j = 0$$

$$U_{i,j+1} - U_{i.j} = 0$$

- The upper boundary represents the far field, and when placed sufficiently far away from the jet, should be defined by a Dirichlet boundary condition containing the velocity of ambient air:

$$\text{for } i = 0 : I, j = J$$

$$U_{i,j} = U_{ambient}$$

- Finally, the right boundary represents the outlet of the flow field. There is no physical boundary condition to be specified here. However, as the Finite Difference expressions make use of a Central Difference scheme, this cannot be applied at the edge of the domain. Therefore, a numerical boundary condition needs to be applied here, replacing the Central Difference scheme with a one-sided expression. The derivation of this expression is done using a Taylor Table and results in:

$$\text{for } i = I, j = 0 : J$$

$$\frac{U_{i-2,j} - 4U_{i-1,j} + 3U_{i,j}}{2\Delta x} = 0$$

4. **Algebraic System of Equations**
The above Finite Difference expressions need to be solved for every point (i, j) within the grid. For a grid of size (I, J), this requires a system of $I \cdot J$ equations for $(I \cdot J$ unknowns. This is achieved by generating a solution vector U of length $I \cdot J$, with terms ordered first by i and then by j. An illustration of this can be seen in Figure A.6. Consequently, two matrices $A_1 and A2$ for the two solution directions x and r are set up, each containing the relevant coefficients from the FD expressions for the respective directions, ordered in correspondence to the solution vector. In this case, the matrices A_1 and A_2 become:

$$A_1 = \frac{1}{2\Delta x}\begin{bmatrix} \ddots & \ddots & \ddots & & \\ & -1 & 0 & 1 & \\ & & \ddots & \ddots & \ddots \end{bmatrix} \tag{A.27}$$

$$A_2 = -\frac{\alpha}{2\Delta r^2}\begin{bmatrix} \ddots & & \ddots & & \ddots & & \\ & \frac{2j-1}{j} & \dots & -4 & \dots & \frac{2j+1}{j} & \\ & & \ddots & & \ddots & & \ddots \end{bmatrix} \tag{A.28}$$

Finally, these two matrices are added back together to form a single coefficient matrix A:

$$A_1 + A_2 = A \tag{A.29}$$

This then allows us to solve the system of equations for the vector $\mathbf{U_x}$, containing the axial velocity at every location (i, j):

$$[A]\mathbf{U_x} = \mathbf{U_{RHS}} \tag{A.30}$$

Here, $\mathbf{U_{RHS}}$ is the Right-Hand-Side vector containing zeroes at every point (i, j) except for the expressions pertaining to the Boundary Conditions.

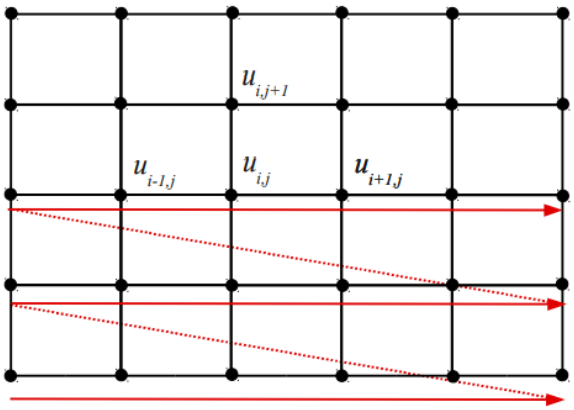

Figure A.6: Ordering of terms within the solution vector for the 2D Finite Difference scheme

Finite Difference expression for Temperature

Once the velocity field is known, the evolution of temperature within the flow field can be determined by applying the advection-diffusion equation with Temperature being the scalar quantity.

1. **Partial Differential Equation**
   The complete advection-diffusion equation for a scalar T in a velocity field **U** is as follows:

$$\frac{\partial T}{\partial t} = -\nabla \cdot (\kappa \nabla T) - \nabla \cdot (\mathbf{U} T) + R \tag{A.31}$$

   The time derivative term $\frac{\partial T}{\partial t}$ becomes zero for a steady state calculation, and the final reaction term R is also assumed to be zero. If the equation is then written in a cylindrical coordinate system with the assumption of axisymmetrical flow, it becomes:

$$\frac{\kappa}{r}\frac{\partial (r\frac{\partial T}{\partial r})}{\partial r} + \kappa \frac{\partial (\frac{\partial T}{\partial x})}{\partial x} + T\nabla \cdot \mathbf{U} + \mathbf{U}\nabla T = 0 \tag{A.32}$$

   From literature, it can be found that the thermal diffusion coefficient κ is in the range of $1e{-}06$ to $1e{-}05$, so it is reasonable to assume that advection is by far the dominant term at the velocities involved in this case. This greatly simplifies the equation to:

$$T\nabla \cdot \mathbf{U} + \mathbf{U}\nabla T = 0 \tag{A.33}$$

   Expressing this relation in cylindrical coordinates and assuming axisymmetric flow results in:

$$T(\frac{\partial U_r}{\partial r} + \frac{U_r}{r} + \frac{\partial U_x}{\partial x}) + U_x \frac{\partial T}{\partial x} + U_r \frac{\partial T}{\partial r} = 0 \tag{A.34}$$

   The equation is separated into $x-$ and $r-$ directions:

$$U_x \frac{\partial T}{\partial x} + T\frac{\partial U_x}{\partial x} = 0 \tag{A.35}$$

$$U_r(\frac{T}{r} + \frac{\partial T}{\partial r}) + T\frac{\partial U_r}{\partial r} = 0 \tag{A.36}$$

2. **Finite Difference Expression**
   Using the same discretization approach as for the derivatives of velocity in the previous step, and ordering by terms $T_{i,j}$, the Finite Difference expressions for the advection of temperature can be written as follows:

$$T_{i+1,j}\frac{U_{x_{i,j}}}{2\Delta x}+T_{i,j}\frac{U_{x_{i+1,j}}-U_{x_{i-1,j}}}{2\Delta x}-T_{i-1,j}\frac{U_{x_{i,j}}}{2\Delta x}=0 \tag{A.37}$$

$$T_{i,j+1}\frac{U_{r_{i,j}}}{2\Delta r}+T_{i,j}\frac{jU_{r_{i,j+1}}+2U_{r_j}-jU_{r_{i,j-1}}}{2j\Delta r}-T_{i,j-1}\frac{U_{r_{i,j}}}{2\Delta r}=0 \tag{A.38}$$

3. **Boundary Conditions**
The domain again requires conditions to be specified on each of the four surrounding boundaries:

   - The initial temperatures of the core, bypass, and ambient air are specified using a Dirichlet condition on the left boundary:

$$\text{for } i=0, j=0:J$$

$$\begin{aligned}&\text{if } r\leq R_{core}: T_{i,j}=T_{core}\\&\text{if } R_{core}<r\leq R_{bypass}: T_{i,j}=T_{bypass}\\&\text{if } r>R_{bypass}: T_{i,j}=T_{ambient}\end{aligned}$$

   - The symmetry condition representing the jet center-line on the lower boundary is given by the one-sided expression for a Neumann boundary:

$$\text{for } i=0:I, j=0$$

$$T_{i,j+1}-T_{i.j}=0$$

   - The upper boundary again represents the far field, which is represented by a Dirichlet condition specifying ambient temperature:

$$\text{for } i=0:I, j=J$$

$$U_{i,j}=U_{ambient}$$

   - Finally, the outlet at the right side is represented by a numerical boundary condition, changing the Central Difference expression to a one-sided one using a Taylor Table. This results in the expression:

$$\text{for } i=J, j=0:J$$

$$T_{i-2}\frac{U_{x_i}}{2\Delta x}+T_{i-1}\frac{-4U_{x_i}}{2\Delta x}+T_i\frac{U_{x_{i-2}}-4U_{x_{i-1}}+6U_{x_i}}{2\Delta x}=0$$

4. **Algebraic system of Equations**
These expressions lead to a system of equations to be solved using linear regression. The approach to this is identical to the approach for solving the velocity equations: Two matrices A_1 and A_2 are set up that represent the left hand side for a total of $I\cdot J$ equations with $I\cdot J$ unknowns, where I and J are the number of steps within the domain in $x-$ and $r-$ direction respectively. The unknowns are the values of T at every location (i,j). The two matrices contain the coefficients for the equations decomposed in $x-$ and $r-$ direction respectively. They are then added together to form the complete coefficient matrix $A=A_1+A_2$, and the following system of equations is solved:

$$[A]\mathbf{T}=\mathbf{T_{RHS}} \tag{A.39}$$

where $\mathbf{T_{RHS}}$ is the solution vector.

At every row i in the matrix A, an equation is represented that describes the Finite Difference expression around a point i within the field. This results in a sparse diagonal matrix with the coefficients representing the multiplication of terms in the Finite Difference expression. Thus, matrix A_1 and A_2 become:

$$A_1 = \frac{1}{2\Delta x}\begin{bmatrix} \ddots & \ddots & \ddots & & \\ & -U_{x_i} & U_{x_{i+1}} - U_{x_{i-1}} & U_{x_i} & \\ & & \ddots & \ddots & \ddots \end{bmatrix} \tag{A.40}$$

$$A_2 = \frac{1}{2\Delta y}\begin{bmatrix} \ddots & & \ddots & & \ddots & \\ & -U_{r_j} & \dots & U_{r_{j+1}} + \frac{2}{j}U_{r_j} - U_{r_{j-1}} & \dots & U_{r_j} \\ & & \ddots & \dots & \ddots & \dots & \ddots \end{bmatrix} \tag{A.41}$$

Finite Difference Expression for Water Vapour Partial Pressure

The water vapour partial pressure is calculated in much the same way as the temperature. The concentration of water can be described by the same advection -diffusion equation. Similarly to the heat diffusivity, molecular diffusivity can also be considered negligible compared to advection at the relevant speeds. This results in the exact same system of equations being used, with the only difference being the boundary conditions.

Implementation in Programming Structure

To summarize the flow of the program as implemented in Python, a simple flowchart is shown in Figure A.7.

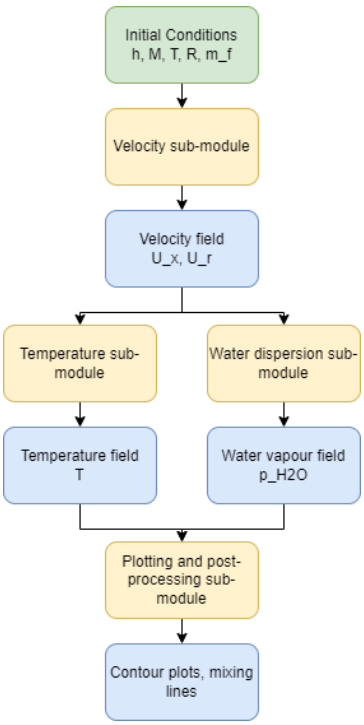

Figure A.7: Modelling flow of the Finite Difference model for calculating the exhaust flow field characteristics

B

Sensitivity Analysis Results

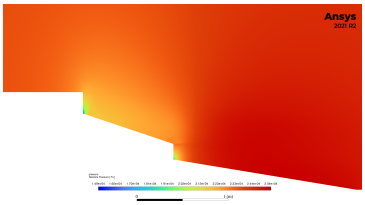

(a) $p_{bypass} = 23742Pa$

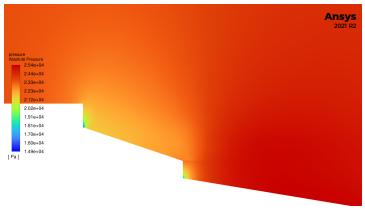

(b) $p_{bypass} = 26000Pa$

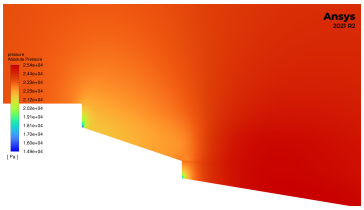

(c) $p_{bypass} = 27160Pa$

Figure B.1: Pressure contours for the Leap-1A engine exhaust with $U_{bypass} = 275ms^{-1}$

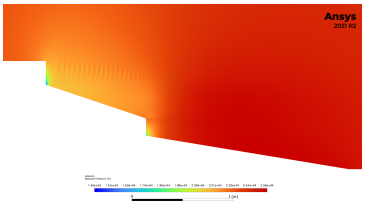

(a) $p_{bypass} = 23742Pa$

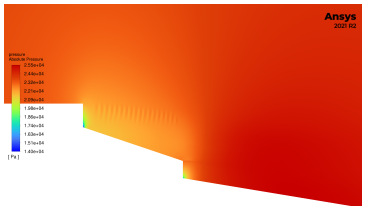

(b) $p_{bypass} = 26000Pa$

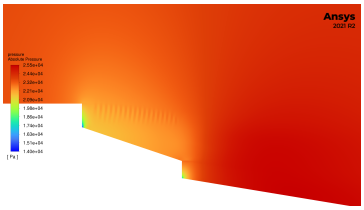

(c) $p_{bypass} = 27160Pa$

Figure B.2: Pressure contours for the Leap-1A engine exhaust with $U_{bypass} = 300ms^{-1}$

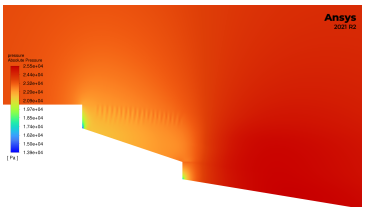

(a) $p_{bypass} = 23742Pa$

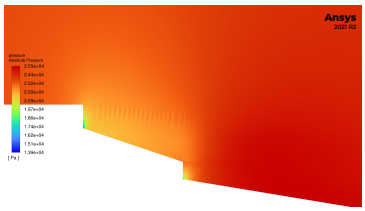

(b) $p_{bypass} = 26000Pa$

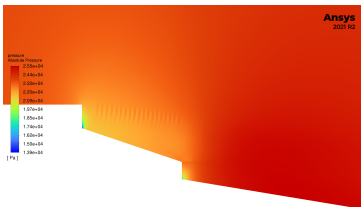

(c) $p_{bypass} = 27160Pa$

Figure B.3: Pressure contours for the Leap-1A engine exhaust with $U_{bypass} = 303ms^{-1}$

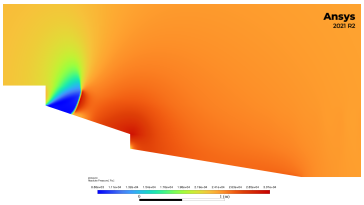

(a) $p_{bypass} = 23742Pa$

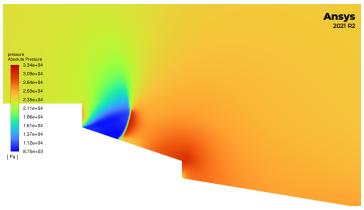

(b) $p_{bypass} = 26000Pa$

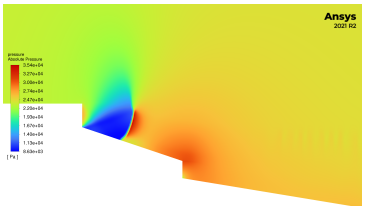

(c) $p_{bypass} = 27160Pa$

Figure B.4: Pressure contours for the Leap-1A engine exhaust with $U_{bypass} = 303.9ms^{-1}$

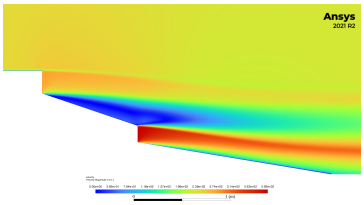

(a) $p_{bypass} = 23742Pa$

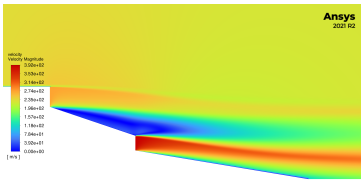

(b) $p_{bypass} = 26000Pa$

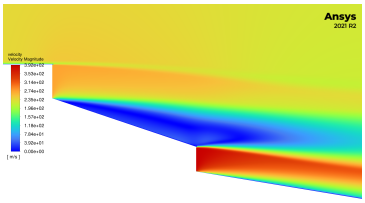

(c) $p_{bypass} = 27160Pa$

Figure B.5: Velocity contours for the Leap-1A engine exhaust with $U_{bypass} = 275ms^{-1}$

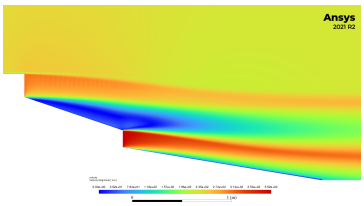

(a) $p_{bypass} = 23742Pa$

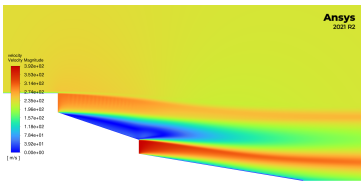

(b) $p_{bypass} = 26000Pa$

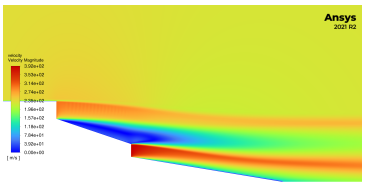

(c) $p_{bypass} = 27160Pa$

Figure B.6: Velocity contours for the Leap-1A engine exhaust with $U_{bypass} = 300ms^{-1}$

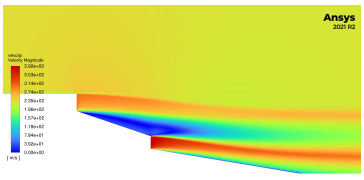

(a) $p_{bypass} = 23742Pa$

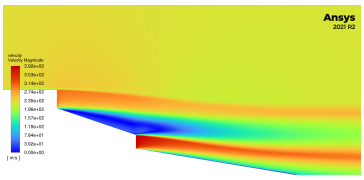

(b) $p_{bypass} = 26000Pa$

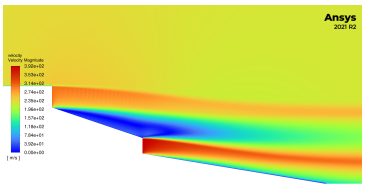

(c) $p_{bypass} = 27160Pa$

Figure B.7: Velocity contours for the Leap-1A engine exhaust with $U_{bypass} = 303ms^{-1}$

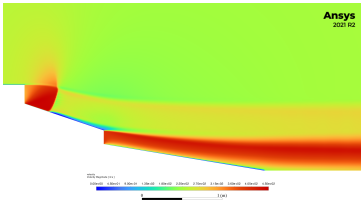

(a) $p_{bypass} = 23742Pa$

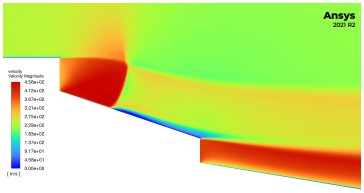

(b) $p_{bypass} = 26000Pa$

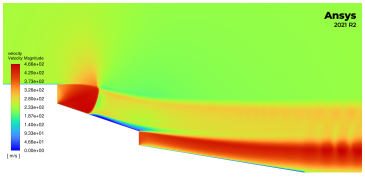

(c) $p_{bypass} = 27160Pa$

Figure B.8: Velocity contours for the Leap-1A engine exhaust with $U_{bypass} = 303.9ms^{-1}$

C

Temperature Gradient based Mixing Validation

One of the key assumptions in the Contrail Formation Prediction model is that the water vapour content can be accurately predicted as a function of the temperature gradient within the flow. To assess the validity of this approach, it is applied to a case from literature in which both the concentration of an inert species and the temperature of a round simple turbulent jet are known. If the model is able to predict both temperature and concentration with a similar degree of accuracy, the assumption can be considered valid.

Validation setup and Boundary Conditions
The validation case used is the paper "Transfer of Heat and Matter in the Turbulent Mixing Zone of an Axially Symmetrical Jet" by Hinze & Van der Hegge Zijnen [15]. The experimental conditions used in this paper are replicated in the CFD Mixing Model, similarly to the validation cases described in section 5.9. These conditions are summarized below:

Boundary type	velocity-inlet		
Parameter	**Specification**	**Value**	**Unit**
Velocity	Magnitude	40	$[ms^{-1}]$
	Direction	Normal to boundary	
Pressure	Gauge Pressure	100	$[Pa]$
Turbulence	Intensity	0.1	[%]
	Length Scale	0.00380	$[m]$
Temperature	Static Temperature	323	$[K]$

Table C.1: Water Vapour Content Validation Case Core Inlet Boundary Conditions

Boundary type	pressure-far-field		
Parameter	**Specification**	**Value**	**Unit**
Velocity	Mach number	0.001	$[-]$
	Direction	Normal to boundary	
Pressure	Gauge Pressure	100	$[Pa]$
Turbulence	Intensity	0.1	[%]
	Length Scale	0.00380	$[m]$
Temperature	Static Temperature	293	$[K]$

Table C.2: Water Vapour Content Validation Case Ambient Boundary Conditions

Parameter definitions
The results from the experiment that are relevant for this validation effort are the radial and axial distributions

Boundary type	pressure-far-field		
Parameter	**Specification**	**Value**	**Unit**
Velocity	Mach number	0.001	[−]
	Direction	Normal to boundary	
Pressure	Gauge Pressure	100	$[Pa]$
Turbulence	Intensity	0.1	[%]
	Length Scale	0.003800	$[m]$
Temperature	Static Temperature	293	$[K]$

Table C.3: Water Vapour Content Validation Case Far Field Boundary Conditions

Boundary type	wall
Velocity	No Slip
Pressure	Not specified
Turbulence	Not specified
Temperature	Adiabatic

Table C.4: Water Vapour Content Validation Case Nozzle wall Boundary Conditions

Boundary type	pressure-outlet		
Parameter	**Specification**	**Value**	**Unit**
Velocity	Not specified		
Pressure	Gauge Pressure at infinity (non-reflecting)	100	$[Pa]$
Turbulence	Intensity	0.1	[%]
	Length Scale	0.003800	$[m]$
Temperature	Static Temperature	293	$[K]$

Table C.5: Water Vapour Content Validation Case Outlet Boundary Conditions

Boundary type	axis
Velocity	Not specified
Pressure	Not specified
Turbulence	Not specified
Temperature	Not specified

Table C.6: Water Vapour Content Validation Case Axis Boundary Conditions

Parameter	**Definition**	**Unit**
Θ	Time - mean value of temperature difference with ambient air	K
Ω	Time-mean value of concentration difference with ambient air	%
x	Axial distance to orifice	m
a	Distance of apparent aperture to orifice	m
d	Diameter of orifice	m
η	Radial distance ratio $\frac{y}{x+a}$	–

Table C.7: Parameters used in the water vapour content validation case

of temperature and concentration. The model outputs are transformed to match the parameters used in the validation case. The definition of these parameters is given in Table C.7.
As the model gives a steady-state solution and the distance a is zero, the temperature and concentration profiles are by definition representative of the time-mean values, and parameter η simplifies to $\eta = \frac{y}{x}$. As a final step, the temperature and concentration profiles are normalized by dividing by the maximum value Θ_m and the nozzle exit value Ω_0 respectively.

Temperature distributions
From the model, the temperature distributions can be directly output and compared to the experiment. This

comparison, for both radial and axial distributions, is shown in Figure C.1 and Figure C.2 respectively.

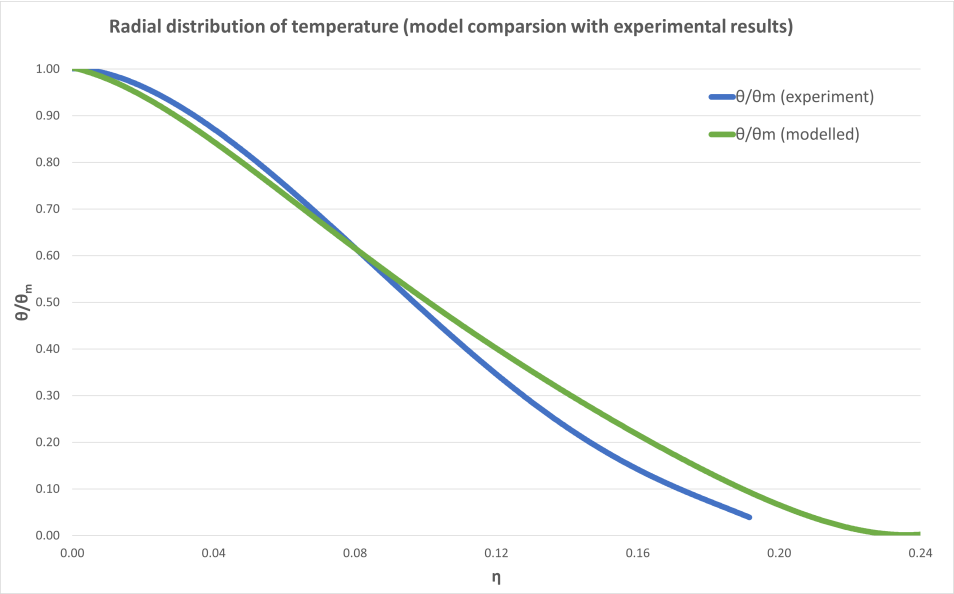

Figure C.1: Comparison of radial temperature distribution for a round turbulent jet: model vs. experiment [15]

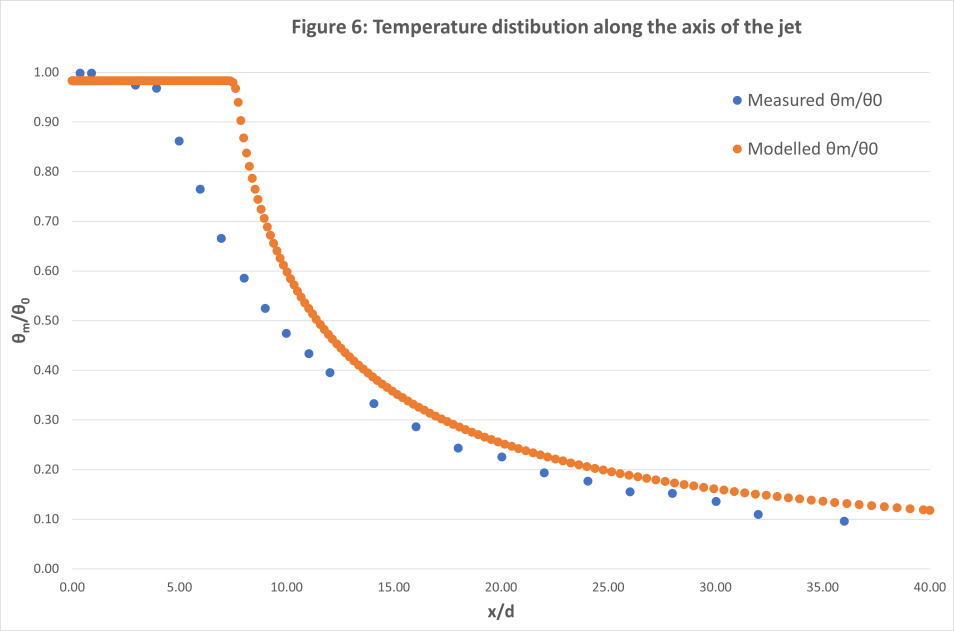

Figure C.2: Comparison of axial temperature distribution for a round turbulent jet: model vs. experiment [15]

By themselves, these comparisons do not provide information with respect to the validity of the assumptions for this section of the model. They do reinforce the conclusions from the validation efforts done in section 5.9, namely that the mixing model overestimates potential core length for simple round jets but provides good agreement in terms of spreading rate.

Concentration distributions

For validation of the concentration calculation, the approach described in section 6.3 is applied to the model temperature field. The resulting radial and axial distributions predicted by the model are then compared to the experimental results. These comparisons can be seen in Figure C.3 and Figure C.4 respectively.

Comparison of results

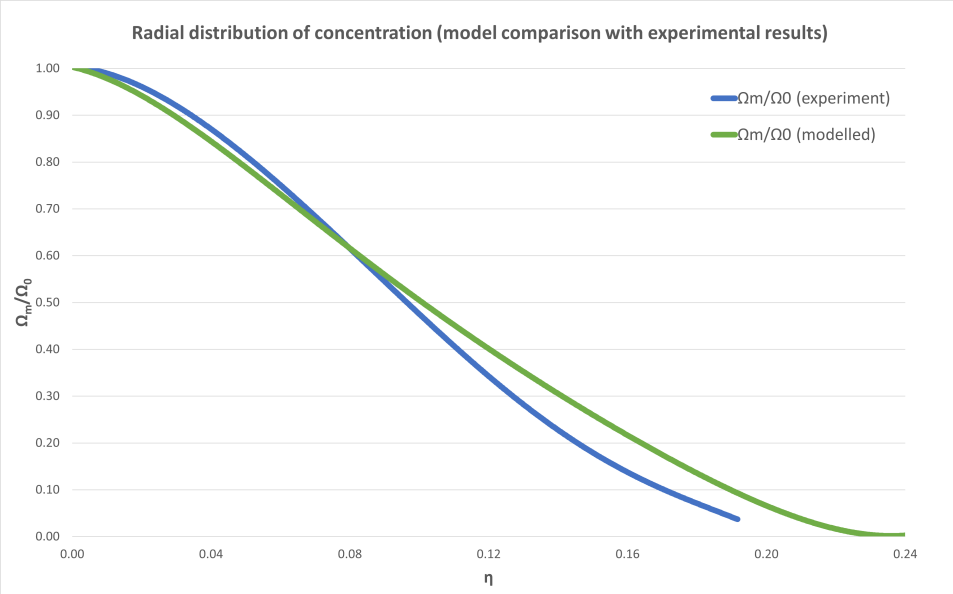

Figure C.3: Comparison of radial concentration distribution for a round turbulent jet: model vs. experiment [15]

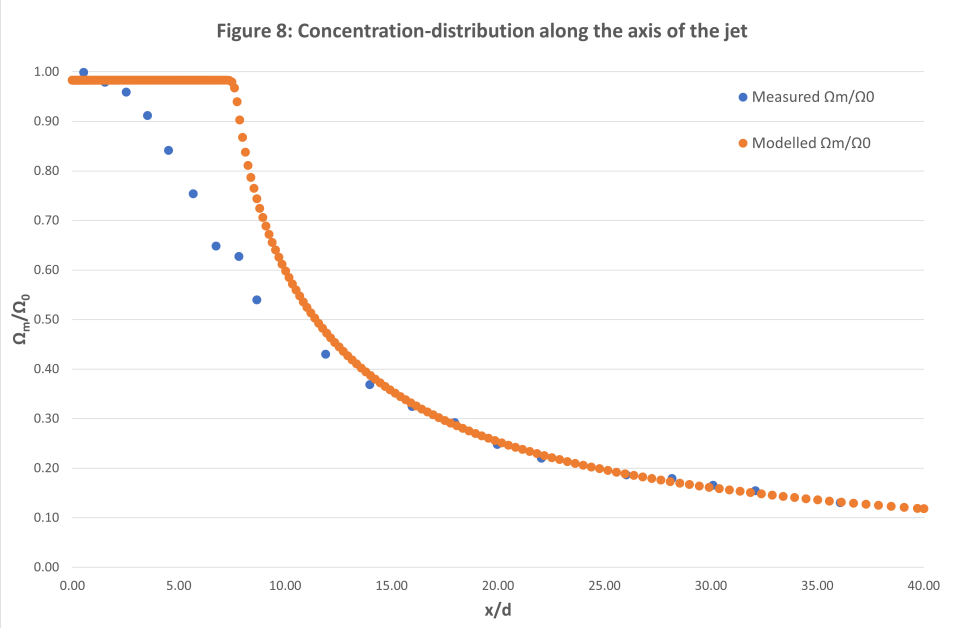

Figure C.4: Comparison of axial concentration distribution for a round turbulent jet: model vs. experiment [15]

When comparing the radial distributions of temperature and concentration, given respectively by Figure C.1 and Figure C.3, it becomes apparent that the model predicts both parameters with no distinguishable difference in accuracy. The same can be said for the comparison of axial distributions between Figure C.2 and Figure C.4. This means that, while there are discrepancies between predicted concentration profiles and experimental results, these are due to underlying modelling errors from the CFD model, which are described in chapter 5. The calculation step from temperature gradient to concentration provides no discernible additional error for the given validation case.

D

Boundary Condition Specifications

D.1. Leap-1A Case Study Boundary Conditions

Parameter	Specification	Value	Unit
Boundary type	velocity-inlet		
Velocity	Magnitude	391.6165	$[ms^{-1}]$
	Direction	Normal to boundary	
Pressure	Gauge Pressure	100	$[Pa]$
Turbulence	Intensity	5	[%]
	Length Scale	0.03	$[m]$
Temperature	Static Temperature	579.85	$[K]$

Table D.1: Core Inlet Boundary Conditions

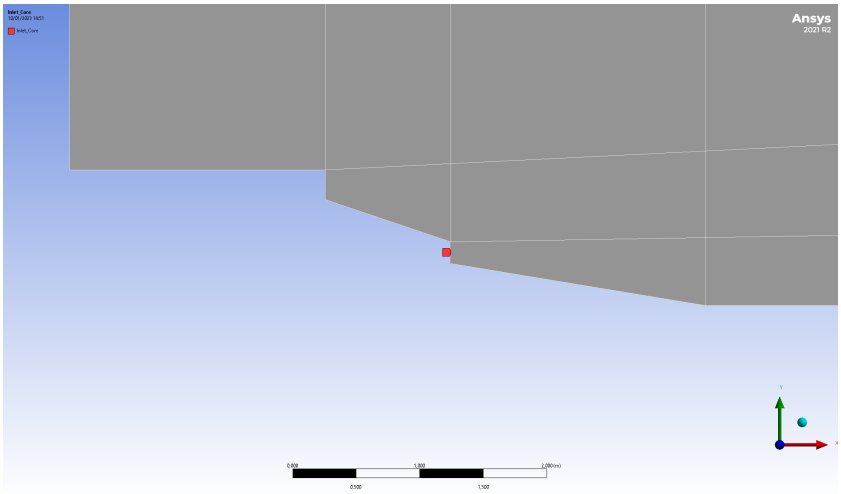

Figure D.1: Location of the Core Inlet Boundary Condition in the Leap-1A model

Parameter	Specification	Value	Unit
Boundary type	velocity-inlet		
Velocity	Magnitude	303.9	$[ms^{-1}]$
	Direction	Normal to boundary	
Pressure	Gauge Pressure	100	$[Pa]$
Turbulence	Intensity	5	[%]
	Length Scale	0.03	$[m]$
Temperature	Static Temperature	229.63	$[K]$

Table D.2: Bypass Inlet Boundary Conditions

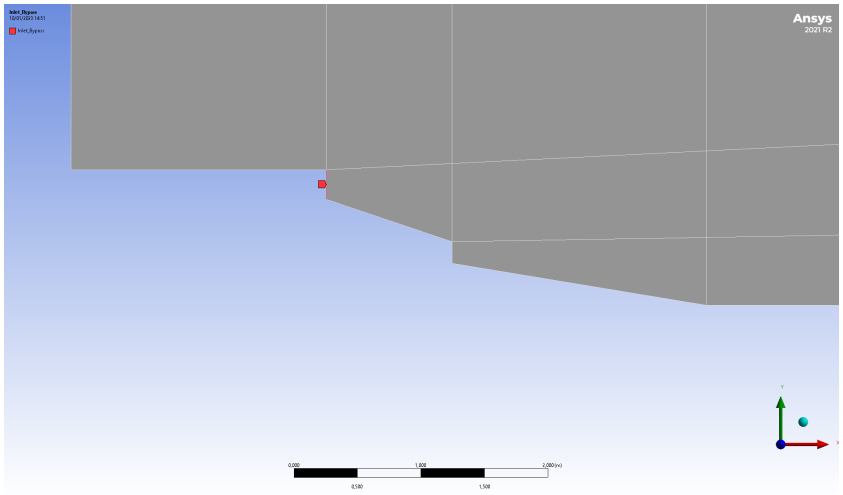

Figure D.2: Location of the Bypass Inlet Boundary Condition in the Leap-1A model

Parameter	Specification	Value	Unit
Boundary type	pressure-far-field		
Velocity	Mach number	0.78	[−]
	Direction	Normal to boundary	
Pressure	Gauge Pressure	100	$[Pa]$
Turbulence	Intensity	5	[%]
	Length Scale	0.03	$[m]$
Temperature	Static Temperature	218.81	$[K]$

Table D.3: Ambient Boundary Conditions

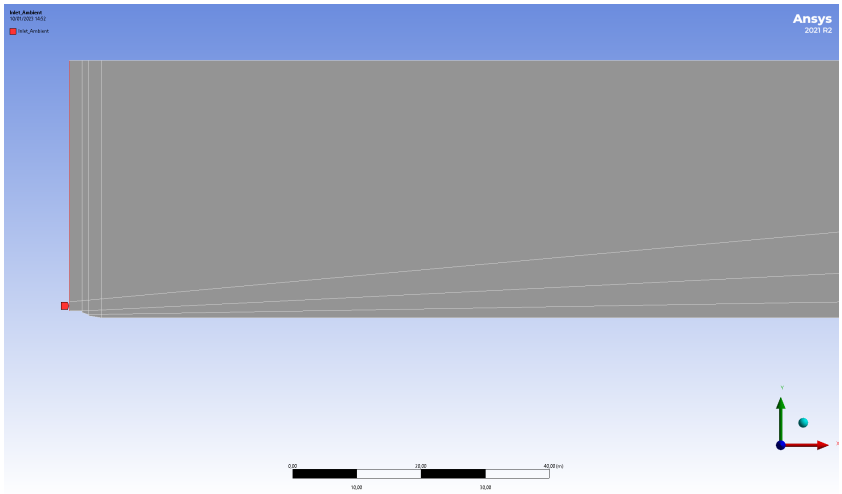

Figure D.3: Location of the Ambient Inlet Boundary Condition in the Leap-1A model

Parameter	**Specification**	**Value**	**Unit**
Boundary type	pressure-far-field		
Velocity	Mach number	0.78	[−]
	Direction	Parallel to boundary	
Pressure	Gauge Pressure	100	$[Pa]$
Turbulence	Intensity	5	[%]
	Length Scale	0.03	$[m]$
Temperature	Static Temperature	218.81	$[K]$

Table D.4: Far Field Boundary Conditions

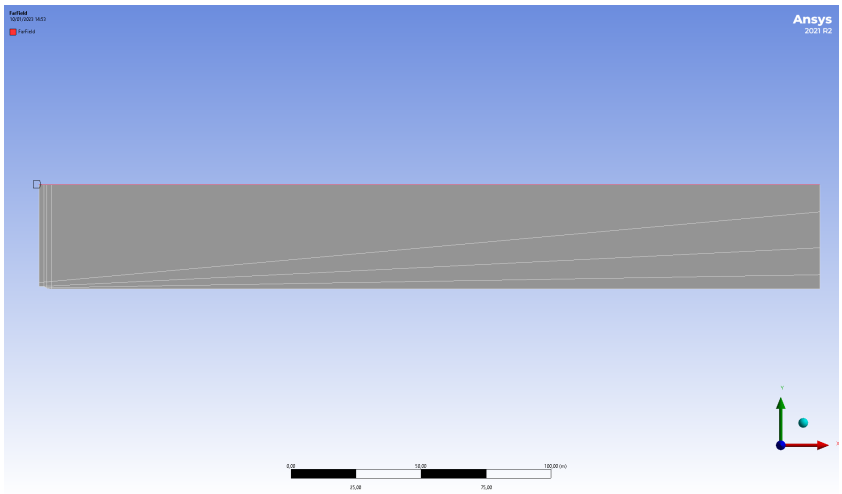

Figure D.4: Location of the Far Field Boundary Condition in the Leap-1A model

Parameter	Specification
Boundary type	wall
Velocity	No Slip
Pressure	Not specified
Turbulence	Not specified
Temperature	Adiabatic

Table D.5: Nozzle wall Boundary Conditions

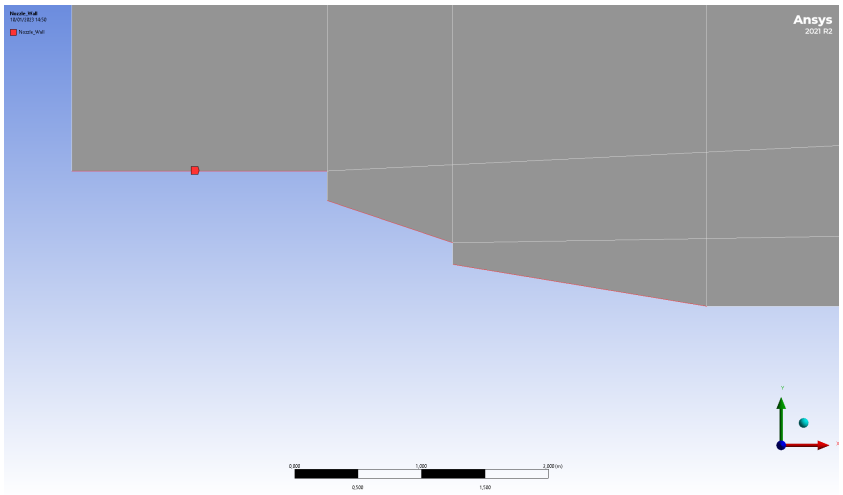

Figure D.5: Location of the Nozzle Wall Boundary Condition in the Leap-1A model

Parameter	Specification	Value	Unit
Boundary type	pressure-outlet		
Velocity	Not specified		
Pressure	Gauge Pressure at infinity (non-reflecting)	100	$[Pa]$
Turbulence	Intensity	5	[%]
	Length Scale	0.03	$[m]$
Temperature	Total Temperature	245.435	$[K]$

Table D.6: Outlet Boundary Conditions

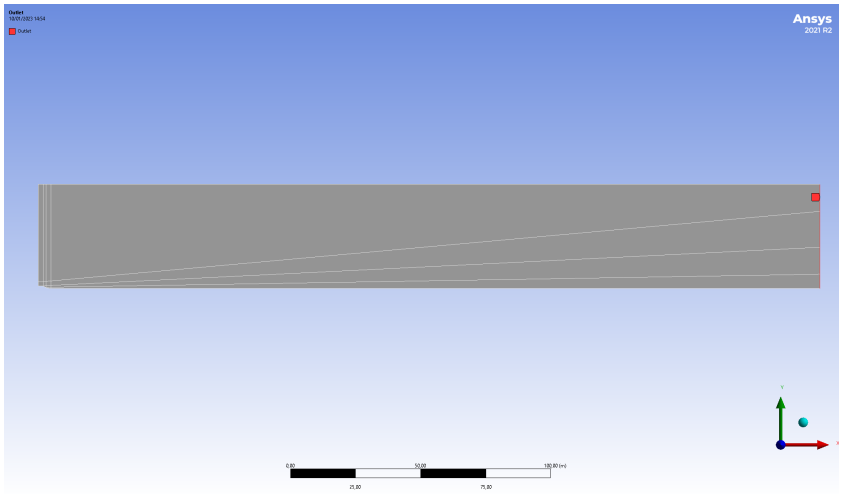

Figure D.6: Location of the Outlet Boundary Condition in the Leap-1A model

Parameter	Specification
Boundary type	axis
Velocity	Not specified
Pressure	Not specified
Turbulence	Not specified
Temperature	Not specified

Table D.7: Axis Boundary Conditions

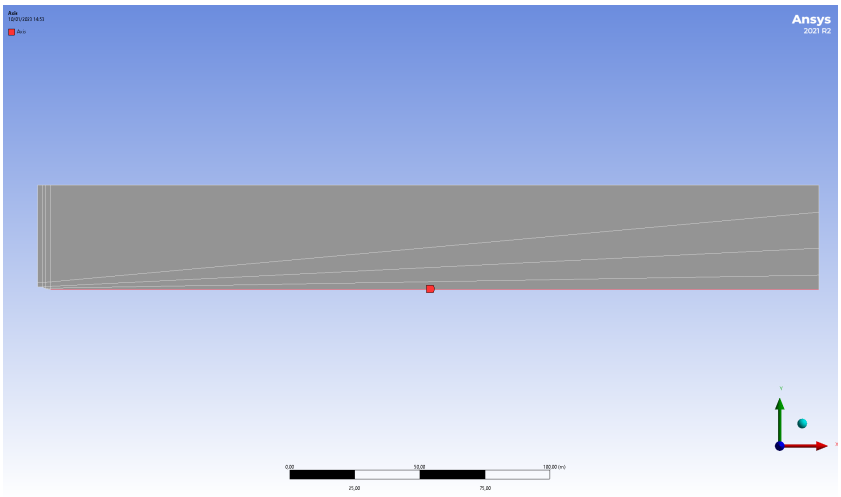

Figure D.7: Location of the Axis Boundary Condition in the Leap-1A model

D.2. Simple Free Round Jet Validation Boundary Conditions

Boundary type	velocity-inlet		
Parameter	**Specification**	**Value**	**Unit**
Velocity	Magnitude	51	$[ms^{-1}]$
	Direction	Normal to boundary	
Pressure	Gauge Pressure	100	$[Pa]$
Turbulence	Intensity	0.1	[%]
	Length Scale	0.00100	$[m]$
Temperature	Static Temperature	293	$[K]$

Table D.8: Free Jet Validation Case Core Inlet Boundary Conditions

Boundary type	pressure-far-field		
Parameter	**Specification**	**Value**	**Unit**
Velocity	Mach number	0.001	$[-]$
	Direction	Normal to boundary	
Pressure	Gauge Pressure	100	$[Pa]$
Turbulence	Intensity	0.1	[%]
	Length Scale	0.00100	$[m]$
Temperature	Static Temperature	293	$[K]$

Table D.9: Free Jet Validation Case Ambient Boundary Conditions

Boundary type	pressure-far-field		
Parameter	**Specification**	**Value**	**Unit**
Velocity	Mach number	0.001	$[-]$
	Direction	Normal to boundary	
Pressure	Gauge Pressure	100	$[Pa]$
Turbulence	Intensity	0.1	[%]
	Length Scale	0.00100	$[m]$
Temperature	Static Temperature	293	$[K]$

Table D.10: Free Jet Validation Case Far Field Boundary Conditions

Boundary type	wall
Velocity	No Slip
Pressure	Not specified
Turbulence	Not specified
Temperature	Adiabatic

Table D.11: Free Jet Validation Case Nozzle wall Boundary Conditions

Boundary type	pressure-outlet		
Parameter	**Specification**	**Value**	**Unit**
Velocity	Not specified		
Pressure	Gauge Pressure at infinity (non-reflecting)	100	$[Pa]$
Turbulence	Intensity	0.1	[%]
	Length Scale	0.00100	$[m]$
Temperature	Static Temperature	293	$[K]$

Table D.12: Free Jet Validation Case Outlet Boundary Conditions

Boundary type	axis
Velocity	Not specified
Pressure	Not specified
Turbulence	Not specified
Temperature	Not specified

Table D.13: Free Jet Validation Case Axis Boundary Conditions

D.3. Co-flow Experiment Validation Boundary Conditions

Boundary type	velocity-inlet		
Parameter	**Specification**	**Value**	**Unit**
Velocity	Magnitude	282	$[ms^{-1}]$
	Direction	Normal to boundary	
Pressure	Gauge Pressure	100	$[Pa]$
Turbulence	Intensity	5	[%]
	Length Scale	0.00308	$[m]$
Temperature	Static Temperature	792	$[K]$

Table D.14: Co-axial Transonic Validation Case Inner Jet Inlet Boundary Conditions

Boundary type	velocity-inlet		
Parameter	**Specification**	**Value**	**Unit**
Velocity	Magnitude	175	$[ms^{-1}]$
	Direction	Normal to boundary	
Pressure	Gauge Pressure	100	$[Pa]$
Turbulence	Intensity	5	[%]
	Length Scale	0.00308	$[m]$
Temperature	Static Temperature	293.15	$[K]$

Table D.15: Co-axial Transonic Validation Case Outer Jet Inlet Boundary Conditions

Boundary type	pressure-far-field		
Parameter	**Specification**	**Value**	**Unit**
Velocity	Mach number	0.01	$[-]$
	Direction	Normal to boundary	
Pressure	Gauge Pressure	100	$[Pa]$
Turbulence	Intensity	5	[%]
	Length Scale	0.00308	$[m]$
Temperature	Static Temperature	293	$[K]$

Table D.16: Co-axial Transonic Validation Case Ambient Boundary Conditions

Boundary type	pressure-far-field		
Parameter	**Specification**	**Value**	**Unit**
Velocity	Mach number	0.01	$[-]$
	Direction	Normal to boundary	
Pressure	Gauge Pressure	100	$[Pa]$
Turbulence	Intensity	5	[%]
	Length Scale	0.00308	$[m]$
Temperature	Static Temperature	293	$[K]$

Table D.17: Co-axial Transonic Validation Case Far Field Boundary Conditions

Boundary type	pressure-outlet		
Parameter	**Specification**	**Value**	**Unit**
Velocity	Not specified		
Pressure	Gauge Pressure at infinity (non-reflecting)	100	$[Pa]$
Turbulence	Intensity	5	[%]
	Length Scale	0.00308	$[m]$
Temperature	Total Temperature	294.425	$[K]$

Table D.18: Co-axial Transonic Validation Case Outlet Boundary Conditions

Boundary type	axis
Velocity	Not specified
Pressure	Not specified
Turbulence	Not specified
Temperature	Not specified

Table D.19: Co-axial Transonic Validation Case Axis Boundary Conditions

E

Flow Field Solver Results

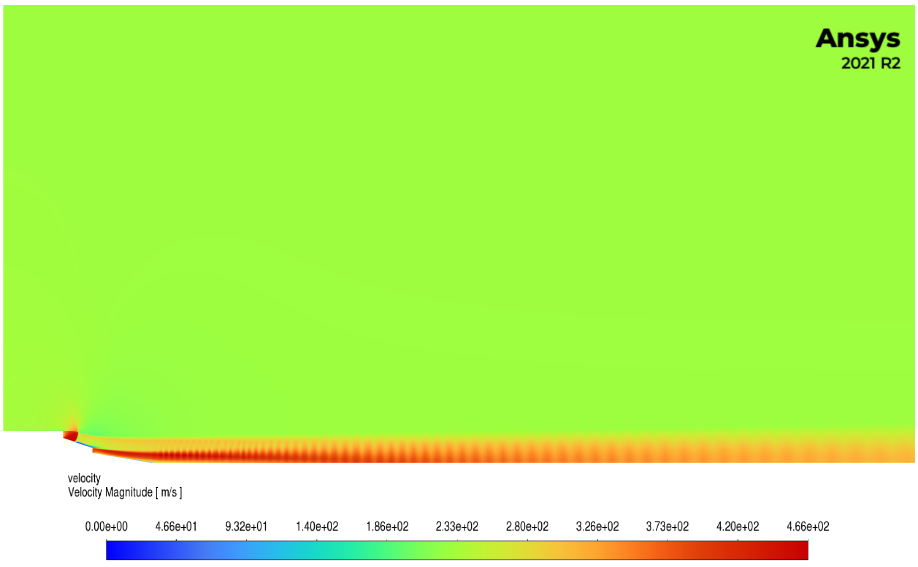

Figure E.1: Contour plot of the velocity in the near-field of the Leap-1A engine

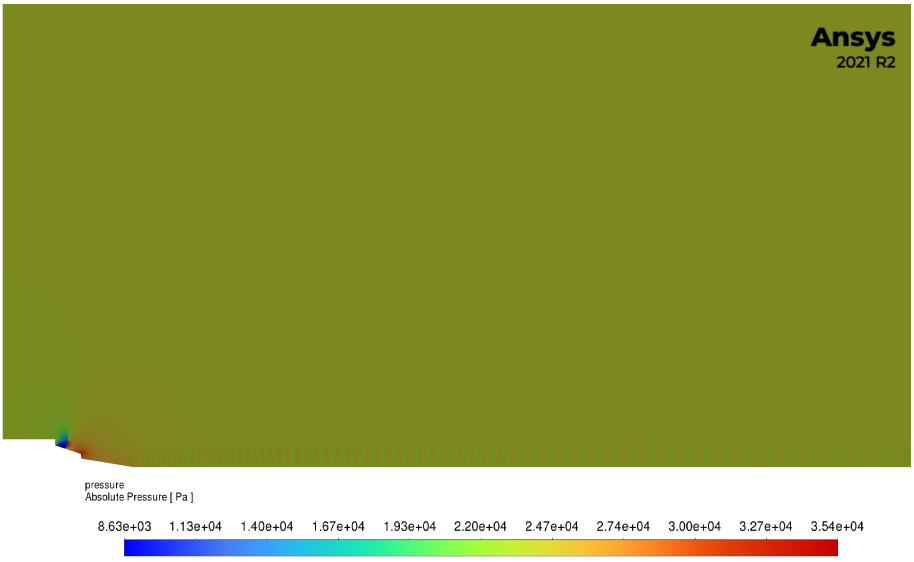

Figure E.2: Contour plot of the pressure in the near-field of the Leap-1A engine

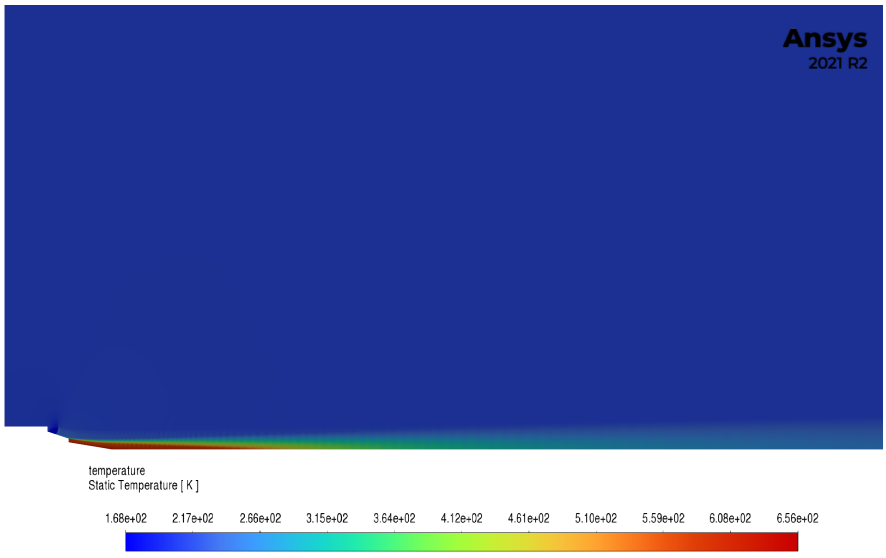

Figure E.3: Contour plot of the temperature in the near-field of the Leap-1A engine

F

Investigation into pyCycle

In their 2019 paper "pyCycle: A Tool for Efficient Optimization of Gas Turbine Engine Cycles", Hendricks and Gray name two main motivations for the development of pyCycle. Firstly, "current state-of-the-art thermodynamic cycle analysis tools are not well suited to integration into vehicles [sic] level models" [13]. Secondly, as aircraft design becomes more multidisciplinary, gradient-based optimization techniques are a key ingredient to vehicle-level design optimization with manageable computational costs. Existing tools are not well suited to implementing these gradient-based techniques. The objective, then, was to "develop a new thermodynamic cycle analysis tool, called pyCycle, that provides analytic derivatives suitable for use with gradient-based optimization".

Working principles of pyCycle

pyCycle was developed on the framework of OpenMDAO. An Extended Design Structure Matrix (XDSM) showing the general structure of the pyCycle tool can be found in Figure F.1. Within it, four basic code blocks can be identified:

- **Cycle block:** This is the core module of the tool. It contains all governing thermodynamic equations for the engine model. Though shown here as a single block, it consists of all submodules that the engine in question is built out of.
- **Balance block:** This block contains a set of implicit state variables and the associated nonlinear residual equations. In practice, this block ensures the engine model is valid by requiring all physical dependencies and design rules to be satisfied.
- **Solver block:** The residual equations from the Balance block are converged by this block.
- **Optimizer block:** This block runs an optimization algorithm to find the design variables that satisfy the given constraints and minimize the objective function.

When modelling a single flight condition, the approach can be summarized as follows:

1. Specify the "On-Design" conditions and optimize the cycle for these conditions. Typical on-design conditions are Top-of-Climb (TOC) and Sea Level Static (SLS) conditions. By setting the known or expected key design parameters such as compressor pressure ratio or maximum turbine inlet temperature (TIT), the on-design calculation results in a set of physical design values, e.g. the turbine and compressor map scalars. The XDSM for On-Design calculations on a geared turbofan engine is shown in Figure F.2.
2. Using the physical design parameters from the on-design calculation, the cycle analysis can now be performed for *any* flight condition. This is defined as the "Off-Design" condition calculation. The XDSM for Off-Design calculations on a geared turbofan engine is shown in Figure F.3.

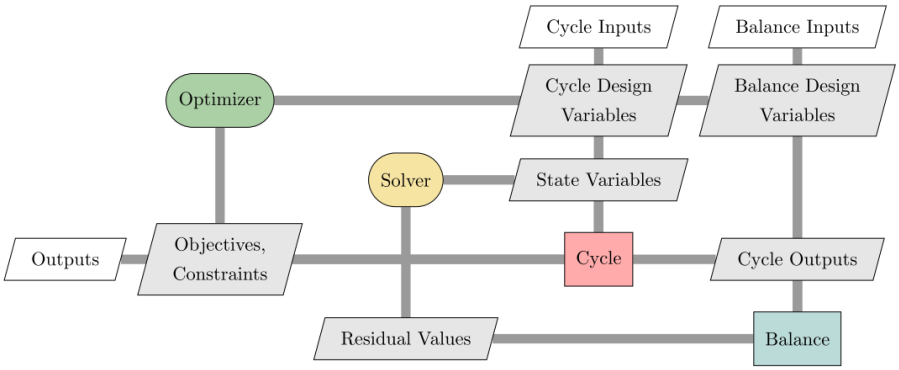

Figure F.1: General pyCycle analysis tool structure [13]

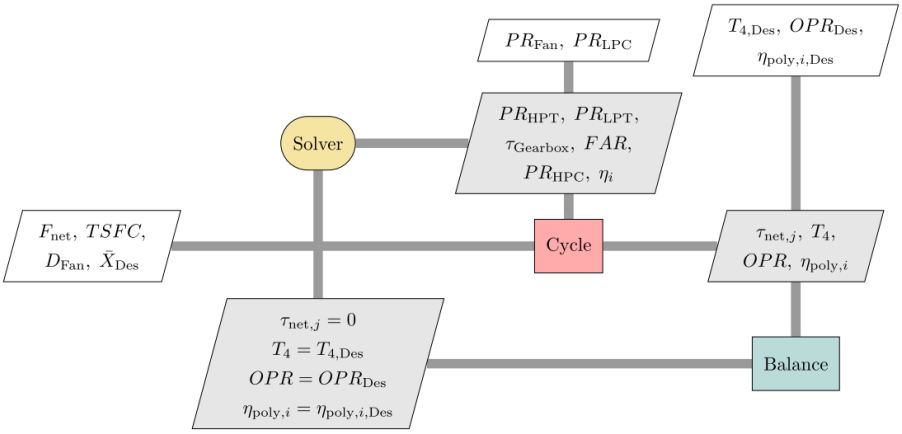

Figure F.2: XDSM for a pyCycle On-Design calculation of a geared turbofan cycle [13]

Multi-Point Design Mode

Aside from the On-Design and Off-Design mode calculations, a third calculation mode is included in pyCycle: the Multi-Design Point (MDP) mode. This combines the functionality of On- and Off-Design analyses. Rather than sequentially specify a single design point and then calculate all off-design conditions, the two are combined to simultaneously evaluate performance at multiple operating conditions. This allows the cycle analysis to be used as part of an optimization process that results in a design satisfying constraints and requirements at multiple design points. The XDSM for a Multi-Design Point analysis of a geared turbofan engine can be seen in Figure F.4.

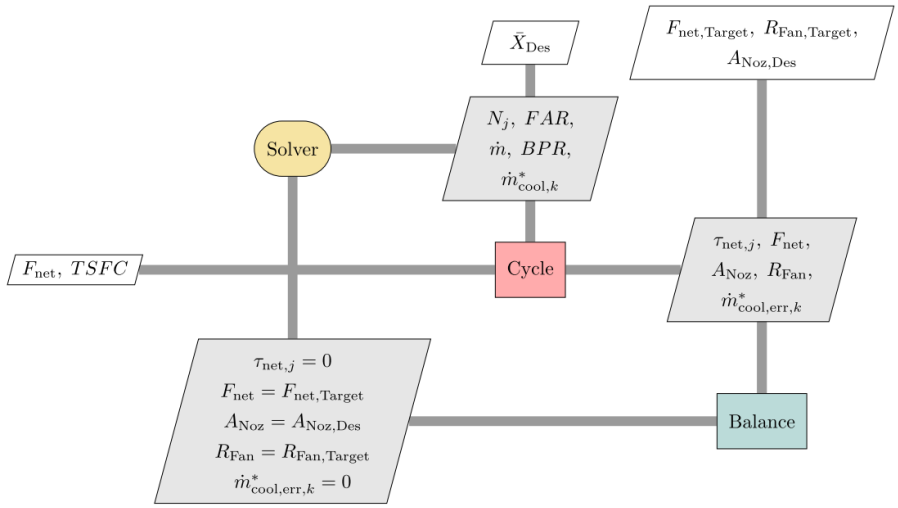

Figure E.3: XDSM for a pyCycle Off-Design calculation of a geared turbofan cycle [13]

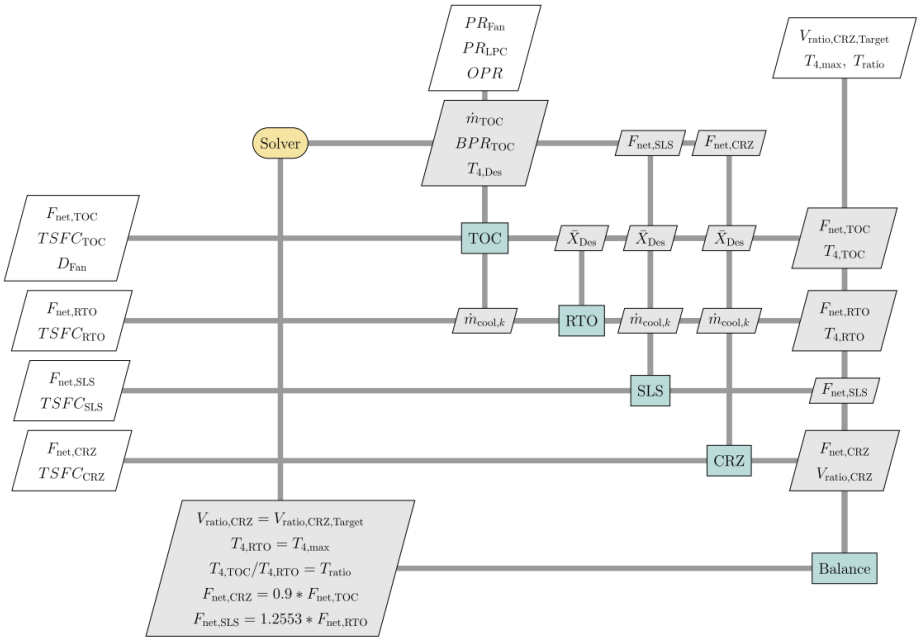

Figure E.4: XDSM for a pyCycle Multi-Design Point calculation of a geared turbofan cycle [13]